

The Influence of Morphology and Molecular Orientation on the
Efficiency and Lifetime of Organic Solar Cells

by

Sibi Sutti

A thesis
presented to the University of Waterloo
in fulfillment of the
thesis requirement for the degree of
Master of Applied Science
in
Electrical and Computer Engineering

Waterloo, Ontario, Canada, 2015

© Sibi Sutti 2015

Author's Declaration

This thesis consists of material all of which I authored or co-authored: see Statement of Contributions included in the thesis. This is a true copy of the thesis, including any required final revisions, as accepted by my examiners.

I understand that my thesis may be made electronically available to the public.

Statement of Contributions

For the paper presented in Chapter 5, I designed and conducted all the experiments, analyzed all data and prepared the manuscript for submission. Graeme Williams trained me to use relevant fabrication and characterization equipment and was also involved in interpreting preliminary data and designing further experiments.

For the paper presented in Chapter 6, I designed and conducted preliminary experiments involving four of the five device structures (A, B, C and D). I studied the photovoltaic properties, UV/visible absorption and external quantum efficiency of these devices. I wrote the first draft of the manuscript detailing the findings from the preliminary study. In order to expand on my preliminary work, Graeme Williams and I also designed and conducted transient photocurrent measurements on the devices. We also added the last device structure, E, to the study. Graeme Williams analyzed the data from the transient photocurrent measurements and wrote the final manuscript.

Abstract

One of the reasons for the low efficiency of organic solar cells (OSCs) is because the relationship between morphology and molecular orientation of the organic semiconductors and the performance and lifetime of the OSC is not well understood.

Theoretically, the morphology and molecular orientation of organic semiconductors influence the three major processes that determine the performance of an OSC. These processes are i) light absorption, ii) exciton dissociation and iii) charge transport. The general objective of this research work is to understand how the morphology of the active layers in an OSC affects these three processes with the aim of gaining insights that can be used to improve OSC efficiency and lifetime. The relationship between device physics and morphology is studied by analyzing the photovoltaic performance, external quantum efficiency, UV/visible absorption, charge conductivity and surface morphology of the fabricated OSCs and relevant organic semiconductor active layers.

Chapters 5 and 6 in this work study the impact of varying the donor-acceptor ratio in OSCs. The best OSC performance was found to occur at high fullerene concentrations due to increased fullerene aggregation resulting in larger absorption and exciton dissociation in the OSC. Building on this insight, OSCs comprising a mixed layer with high fullerene content followed by a neat fullerene layer, was identified to possess the highest performance of all other device architectures due to balanced charge generation and charge collection. Chapters 7 and 8 in this work study the impact of varying the molecular orientation of phthalocyanine donor materials using templating layers on the performance and lifetime of planar heterojunction OSCs. Templating layers force the phthalocyanine molecules to lie flat on the substrate affecting the three main OSC processes. Depending on the combination of the templating layer and phthalocyanine, different aspects of the OSC device physics are altered leading to large differences in performance gains obtained from templating. Finally, it was found that the morphology of the donor material affects the morphology of fullerene acceptor deposited on top, which results in substantial variation in the lifetimes of phthalocyanine/fullerene planar heterojunction OSCs.

Acknowledgements

I would like to first acknowledge my supervisor, Professor Hany Aziz, for his invaluable insights, discussions and advice during the course of this research work. The freedom and flexibility that he offered me in pursuing my research interests allowed me to grow as an independent thinker and helped me gain confidence in my abilities for research and beyond.

Next, I would like to acknowledge my colleague, Graeme Williams, for his assistance in the research work that I performed. His expert training and guidance on all lab equipment helped me master the tools I needed to do my work and produce results in a timely manner.

I would like to acknowledge the tireless efforts of the G2N lab manager, Mr. Richard Barber. Without his knowledge and expertise in all things related to the clean room, I would not have been able to overcome many of the challenges that I encountered during the course of my research.

I would like to acknowledge my fellow lab mates, past and present, for their advice, assistance and company, in and out of the lab. Namely, Qi Wang, Afshin Zamani Siboni, Mike Zhang, Bin Sun, Uyxing Vongsaysy, Mina Abdelmalek, Thomas Borel, Yoshitaka Kajiyama, Anne Bouchady, Tyler Davids, Elizabeth Salsberg and Amanda Victorious.

Finally, I would like to acknowledge my funding sources that allowed me to carry out this research – Natural Sciences and Engineering Research Council of Canada, Ontario Graduate Scholarship, Waterloo Institute of Nanotechnology and University of Waterloo Graduate Scholarships.

Dedication

I would like to dedicate this work to all those in my life who continually help me
learn, grow and discover

Table of Contents

Author's Declaration	ii
Statement of Contributions	iii
Abstract.....	iv
Acknowledgements	v
Dedication	vi
List of Figures.....	x
List of Tables	xii
List of Abbreviations	xiii
Chapter 1 - Introduction	1
1.1 Physics of organic semiconductors	3
1.2 The Influence of Morphology and Molecular Orientation.....	6
1.3 Device Structure and Operation of Organic Solar Cells	7
1.4 Photovoltaic Performance of an Organic Solar Cell.....	10
1.5 Factors Limiting the Efficiency of Organic Solar Cells.....	11
1.6 Organic Solar Cell Materials and Fabrication Technologies.....	14
Chapter 2 - Background and Literature Review	16
Chapter Summary.....	16
2.1 Donor and Acceptor Materials.....	17
2.2 Donor Acceptor Ratio	18
2.2.1 Unanswered Questions.....	21
2.3 Templating Layers	22
2.3.1 Unanswered Questions.....	28
Chapter 3 – Objectives	30
Chapter 4 – Research Methodology and Experimental Procedures	31
4.1 Research Methodology.....	31
4.2 Basic Device Fabrication Procedure.....	32
4.3 Basic Characterization Procedure.....	34

Chapter 5 - Role of the Donor Material and the Donor-Acceptor Mixing Ratio in Increasing the Efficiency of Schottky Junction Organic Solar Cells	36
Chapter Summary	36
5.1 Introduction	37
5.2 Materials and methods.....	38
5.3 Results and Discussion	39
5.3.1 Influence of the Donor-Acceptor Mixing Ratio.....	39
5.3.2 Influence of the Choice of Donor Material.....	45
5.4 Conclusions	53
Chapter 6 – Interplay Between Efficiency and Device Architecture for Small Molecule Organic Solar Cells	55
Chapter Summary	55
6.1 Introduction	56
6.2 Experimental.....	57
6.3 Results and Discussion	58
6.3.1 From Planar Heterojunction to Bulk Heterojunction.....	61
6.3.2 From Bulk Heterojunction to Planar-Mixed Structures.....	67
6.3.3 Full Planar-Mixed Molecular Heterojunction.....	74
6.4 Conclusions	80
Chapter 7 – Effect of PTCDA and CuI Templating on Hole Mobility and Performance of Phthalocyanine/C60 Organic Solar Cells	81
Chapter Summary	81
7.1 Introduction	82
7.2 Experimental Methods.....	83
7.3 Results and Discussion	84
7.3.1 Effect of Templating on Photovoltaic Properties.....	84
7.3.2 Effect of Templating on EQE and Absorption	86
7.3.3. Effect of Templating on Hole Transport.....	90
7.3.4 Effect of Templating on Surface Morphology.....	97
7.4 Conclusions	99
Chapter 8 – Influence of the Donor Material on the Degradation Behavior of C60-Based Planar Heterojunction Organic Solar Cells	101

Chapter Summary	101
8.1 Introduction	102
8.2 Experimental Methods	104
8.3 Results and Discussion	105
8.3.1 Degradation of C60 Schottky OSCs	105
8.3.2 Degradation of Phthalocyanine/C60 PHJ OSCs	108
8.3.3 Influence of C60 Morphology on Degradation Behavior	109
8.4 Conclusions	115
Chapter 9 – Conclusions and Future Work	116
Letters of Copyright Permission	119
References	131
Appendix	148

List of Figures

Figure 1: Bonding structure of ethylene. Reproduced with permission from ref. [11].	3
Figure 2: Examples of a few popular organic semiconductors and their applications	4
Figure 3: Schematic of a) PHJ OSC and b) BHJ OSC with typical thicknesses	9
Figure 4: Photovoltaic parameters of a solar cell. Reproduced with permission from ref. [11].	10
Figure 5: Molecular structure of un-substituted phthalocyanine and a schematic of its herringbone packing with typical lattice spacings. Adapted from ref. [3].	18
Figure 6: Cross-sectional TEM of TPTPA:C70 OSCs at 5% TPTPA Concentration. Reproduced with permission from ref. [8].	21
Figure 7: a) Top down view of PTCDA on substrate, b) Top down view of H2Pc on substrate, c) Side view of H2Pc grown on PTCDA. Reproduced with permission from ref. [3]	23
Figure 8: Stacking of FePc on a) Bare SiO ₂ and b) SiO ₂ /CuI template layer. Reproduced with permission from ref. [28]. Published by The Royal Society of Chemistry.	28
Figure 9: Schematic of a thermal evaporation chamber. Reproduced with permission from ref. [1]	32
Figure 10: Schematic of the substrate used for OSC fabrication.	33
Figure 11: Schematic of the Schottky junction device structure used to investigate the effect of the mixing ratio. Reproduced with permission.	40
Figure 12 a) EQE spectra of Schottky junction devices with varying donor concentration, and b) UV/Vis absorption spectra of Schottky junction devices. Also shown: UV/Vis absorption spectrum of C ₆₀ in toluene and the AM1.5 spectrum	41
Figure 13: AFM images of 50nm films of a) pure C ₆₀ , b) 10% ClInPc in C ₆₀ , c) 20% ClInPc in C ₆₀ and d) 50% ClInPc in C ₆₀ on CF ₄ :O ₂ plasma treated ITO. Reproduced with permission.	44
Figure 14: a) Schematic of the Schottky junction device structure used to test the effect of varying the donor material at 10% donor concentration with associated energy levels shown below and b) EQE spectra of devices shown in (a). Reproduced with permission.	46
Figure 15: a) Schematic of the hole-only device structure used to study the hole extraction properties of different donor materials and b) IV characteristics of the devices in (a) with different donors	48
Figure 16: i. Energy level diagram for ClGaPc/C ₆₀ organic solar cells. ii. Absorbance spectra of 50 nm films of C ₆₀ and ClGaPc. Reproduced with permission from the PCCP Owner Societies.	59
Figure 17 - Illustration of OSC Device Architectures, including: a) planar heterojunction (PHJ), b) bulk heterojunction (BHJ). c) BHJ with a neat acceptor layer, d) BHJ with a neat donor layer and e) planar-mixed molecular heterojunction. Reproduced with permission from the PCCP Owner Societies.	60
Figure 18 - Photovoltaic output parameters of ClGaPc:C ₆₀ OSCs with varying device architectures and varying acceptor (C ₆₀) content. Devices A through E correspond to the PHJ, BHJ, BHJ/acceptor, donor/BHJ and PM-HJ device architectures respectively. Reproduced with permission from the PCCP Owner Societies	61
Figure 19 - External quantum efficiency spectra of the PHJ (A) and BHJ (B) ClGaPc:C ₆₀ OSCs with different layer thicknesses (PHJ) and C ₆₀ content (BHJ). Reproduced with permission from the PCCP Owner Societies.	63

Figure 20 - Modified external quantum efficiency spectra of the PHJ ClGaPc/C60 OSC with varying layer thicknesses. Pc contributions have been subtracted using normalized UV/Vis data (described in the body of the manuscript). Reproduced with permission from the PCCP Owner Societies.....	64
Figure 21 - Single exponential fit tau values for transient photocurrent decay (falling current) after illumination with a white LED pulse. Tau values are plotted vs. C60 content for PHJ and BHJ ClGaPc:/C60 OSCs. Reproduced with permission from the PCCP Owner Societies.....	66
Figure 22 - External quantum efficiency spectra of the BHJ (B), BHJ/acceptor (C), donor/BHJ (D) and PM-HJ (E) ClGaPc:C ₆₀ OSCs with varying C ₆₀ content. Reproduced with permission from the PCCP Owner Societies.	69
Figure 23 - Single exponential fit tau values for transient photocurrent decay (falling current) after illumination with a white LED pulse. Tau values are plotted vs. C60 content for BHJ. Reproduced with permission from the PCCP Owner Societies.	71
Figure 24 - i. Transient photocurrent decay of a 1:7 ClGaPc:C60 PM-HJ OSC under bright light and dim light. ii. Single exponential fit (SE) and double exponential fit (DE) t values for the transient photocurrent decays of PM-HJ ClGaPc:C ₆₀ OSCs. Reproduced with permission from the PCCP Owner Societies.....	77
Figure 25: EQE spectra of control and PTCDA templated ZnPc, ClAlPc and SubPc PHJ OSCs	86
Figure 26: UV/vis absorption spectra of templated and control ZnPc and ClAlPc PHJ OSCs.....	88
Figure 27: UV/visible absorption spectrum of neat ZnPc and ClAlPc films with PTCDA deposited before and after the phthalocyanines	91
Figure 28: J-V curves (solid lines) and SCLC fits (dotted lines) of ZnPc hole-only devices	93
Figure 29: J-V curve (solid lines) and SCLC fits (dotted lines) of the ClAlPc hole-only devices.....	94
Figure 30: I-V curve of SubPc Hole Only Devices	97
Figure 31: AFM scans of templated and untemplated ZnPc and ClAlPc.....	98
Figure 32: PV parameters of ZnPc, SubPc and ClInPc PHJ OSCs as a function of aging time.....	105
Figure 33: External quantum efficiency spectra of fresh and aged samples of C60 only OSCs, ZnPc PHJ OSCs, ClInPc PHJ OSCs and SubPc PHJ OSCs.	106
Figure 34: a) Absorption of C60 only OSC before and after aging and b) Absorption of ClInPc/C60 PHJ OSC before and after aging	107
Figure 35: AFM Images of C60 on top of ClInPc and SubPc	111
Figure 36: PV parameters of templated and non-templated ZnPc PHJ OSCs as a function of aging time	112
Figure 37: PV parameters of templated and non-templated ClInPc PHJ OSCs as a function of aging time	113

List of Tables

Table 1: Comparison of Vacuum Thermal Evaporation and Solution Processing	15
Table 2: Photovoltaic performance of ClInPc:C ₆₀ Schottky junction devices with different doping concentrations. Reproduced with permission	40
Table 3: Photovoltaic performance of Schottky junction devices with different donor materials at 10% donor concentration. The schematic of the device structure is shown in Figure 4(a). Reproduced with permission.....	47
Table 4: Photovoltaic performance of ClInPc:C ₇₀ devices for different doped layer thicknesses. The device structure is CF ₄ -Treated ITO/ClInPc:C ₇₀ (x nm)/C ₇₀ (30 – x nm)/BCP/Al. Reproduced with permission.	52
Table 5: PV Parameters of control and PTCDA templated ZnPc, ClAlPc and SubPc PHJ OSCs	85
Table 6: Zero-field mobilities and field activation parameters of templated and untemplated ZnPc and ClAlPc hole only devices	92
Table 7: EQE percent differences between fresh and aged samples for templated and control ClInPc and ZnPc PHJ OSCs	114
Table A8: Time-zero PV Performance of ZnPc, SubPc and ClInPc PHJ OSCs used in Chapter 8	148
Table A9: Time-zero PV Performance of Control, PTCDA-templated and CuI-templated ZnPc PHJ OSCs shown in Chapter 8	148
Table A10: Time-zero PV Performance of Control, PTCDA-templated and CuI-templated ClInPc PHJ OSCs shown in Chapter 8	148

List of Abbreviations

a-Si	Amorphous Silicon
AFM	Atomic Force Microscopy
BHJ	Bulk Heterojunction
CdTe	Cadmium Telluride
ClAlPc	Chlorine Aluminum phthalocyanine
ClInPc	Chlorine Indium phthalocyanine
CuI	Cooper iodide
CuPc	Copper phthalocyanine
EBL	Exciton Blocking Layer
EQE	External Quantum Efficiency
FF	Fill Factor
GW	Gigawatts
HOMO	Highest occupied molecular orbital
IEA	International Energy Agency
ITO	Indium tin oxide
Jsc	Short-circuit current density
LUMO	Lowest unoccupied molecular orbital
MFP	Mean Free Path
OLED	Organic light emitting diode
OSC	Organic Solar Cells
OTFT	Organic thin film transistor
PbPc	Lead phthalocyanine
PHJ	Planar Heterojunction
PMHJ	Planar Mixed Heterojunction
PTCDA	Perylene-3, 4, 9, 10-tetracarboxylic dianhydride
PV	Photovoltaics
QCM	Quartz crystal monitor
RMS	Root mean squared
SubPc	Boron subphthalocyanine chloride

TEM	Transmission electron microscopy
TiOPc	Titanium oxide phthalocyanine
UV/Vis	Ultraviolet/Visible
Voc	Open Circuit Voltage
VOPC	Vanadium oxide phthalocyanine
XRD	X-ray diffraction
ZnPc	Zinc phthalocyanine

Chapter 1 - Introduction

It is often said that the sunlight incident on the Earth's surface every hour has enough energy to power human civilization for a year [1]. Harnessing this power source in the near future is crucial to reduce our over-reliance on fossil fuels and reverse the damage that we have already caused to our planet's environment.

The adoption of green and renewable energy technologies has been on the rise in the past decade. In the World Energy Outlook New Policies Scenario published by the International Energy Agency (IEA), renewable electricity generation technologies are expected to grow three times from 2012 to 2040 [2]. However, with regards to climate change, the sobering reality is that this growth rate is not fast enough. Power generation on a global scale must be switched to green energy sources as soon as possible if we are to avoid catastrophic weather-related disasters in the next century [3,4]. Traditional renewable energy resources like hydroelectricity and geothermal electricity are approaching their installation capacity in many areas and have limited growth potential in the future. Out of the remaining options, the most widely adoptable renewable energy technologies are wind and solar photovoltaics (PV), which have showed an average annual growth rate of approximately 25% and 50% in the past 5 years respectively [5]. The installed solar PV power generation capacity has risen from 1.5 giga-watts (GW) in 2000 to 67 GW in 2011 indicating that demand for solar power is strong and the market is ready for widespread adoption. In order to exploit this demand and make ubiquitous solar power a reality, the cost of solar PV systems must be drastically reduced so that they can out-compete non-renewable energy sources.

There are several PV technologies in the market today that aim to deliver the cost-savings necessary to make solar power a primary energy source. Most of the installed solar PV power generation capacity so far (~85%) is provided by traditional "generation 1" PV technologies based on crystalline silicon. Many of these installations rely on large governmental subsidies to make them cost competitive against non-renewable energy

sources. Newer “generation 2” PV technologies aim to drastically reduce the cost per watt of solar PV by reducing semiconductor material costs. The most developed generation-2 PV technologies use thin films of amorphous silicon (a-Si), cadmium telluride (CdTe) or copper-indium-gallium-selenide (CIGS) as the semiconductor material. The advantages of using these materials include low material usage per watt of generated power, lower purification requirements and thinner and lighter modules. CdTe and CIGS solar cells are relatively mature technologies that have already reached efficiencies (~20%) and cost-per-watt (~\$1 per Watt-peak) comparable to generation-1 PV technologies. Some of the world’s largest solar farms use CdTe panels instead of crystalline silicon indicating that generation-2 PV technologies are slowly being adopted [6]. The market share of thin-film generation-2 PV is hovering around 15% and expected to grow in the future. However, even these generation-2 PV technologies have not reached a level of cost-competitiveness with non-renewable power generation sources that would allow for global adoption. In addition, CdTe and CIGS solar cells rely on using elements that are rare in the Earth’s crust or possess significant health risks, which can raise concerns when it comes to mass-production on a global scale.

Organic solar cells are an emerging generation-2 solar PV technology that promise to provide the cheapest cost-per-watt with the bonus of easy and safe scale-up possibilities for global mass-production. OSCs are made using organic semiconducting materials that can be easily synthesized using safe and commonly available materials in batch processes and fabricated on a large scale using roll-to-roll solution coating or vacuum deposition methods. However, OSCs as a technology, are still in its infancy. The best research cells [7], fabricated by Heliatek GmbH., show 12% efficiency, which is much lower than the 20% efficiency of CdTe or CIGS solar cells. The sub-module efficiencies of OSCs are even lower at a reported 8% [8] with cost-per-watt ranging in the \$11-12 watt-peak range [9]. In order to make OSCs cost-competitive with other PV technologies and eventually, enable solar power on a global scale, extensive research is needed to improve their efficiencies and lower their cost. Assuming 15% module efficiency can be attained using a mass-producible technique such as roll-to-roll processing, OSCs can deliver sub-dollar per watt solar energy on a global scale [10]. The

following sections detail the fundamentals of OSCs and discuss the active areas of research and improvement for this technology.

1.1 Physics of organic semiconductors

Organic semiconducting molecules possess carbon chain backbones with conjugated π -orbitals for electron or hole conduction. Molecules with conjugated π -orbitals have alternating carbon to carbon single and double bonds in their backbone. For example, in the simple molecule ethylene (C_2H_4), each carbon atom is bonded to two hydrogen atoms and double bonded to the other carbon atom. Therefore, each carbon atom is sp^2 hybridized with the p_z orbitals left unhybridized. The p_z orbitals of each carbon atom possess weak interactions and form a delocalized state above and below the ethylene molecular plane due to electron cloud overlap. Due to the weak nature of the π -orbital interactions, the π bonding molecular orbital and the π anti-bonding molecular orbital represent the lowest energy electronic excitation in the molecule. As such, the π bonding orbital is labeled the highest occupied molecular orbital (HOMO) and the π anti-bonding orbital is labeled the lowest unoccupied molecular orbital (LUMO). This is schematically shown in Figure 1 [11].

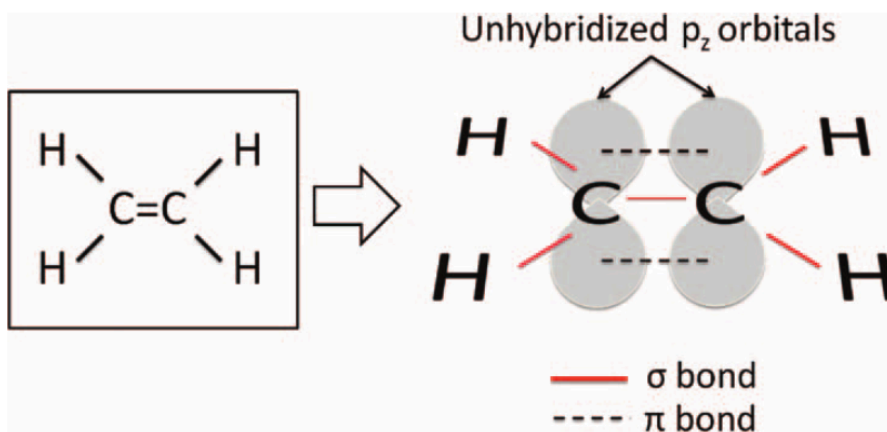
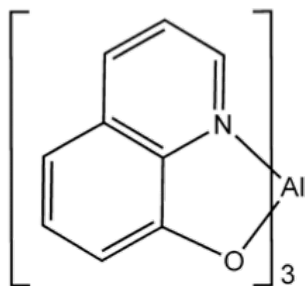


Figure 1: Bonding structure of ethylene. Reproduced with permission from ref. [11].

Most organic semiconductors used in organic light emitting diodes (OLEDs), organic solar cells and organic thin film transistors (OTFTs) possess extended conjugated

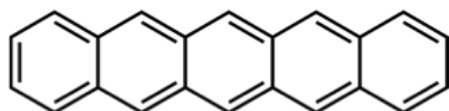
systems that determine their luminescence and electronic properties. Examples of a few popular organic semiconductors are shown in Figure 2.



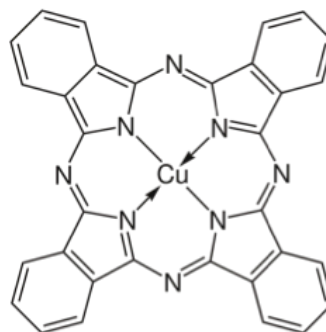
Alq3 – OLED Green Emitter



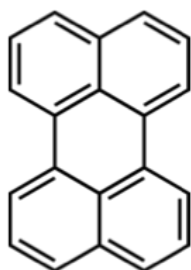
C60 – OSC Acceptor



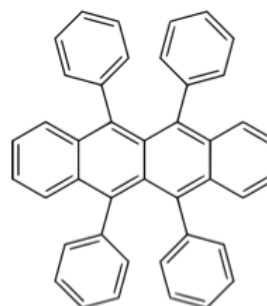
Pentacene – OTFT hole transport, OSC donor



Copper phthalocyanine - OSC donor



Perylene – OLED blue emitter



Rubrene – OTFT hole transport, OLED red emitter

Figure 2: Examples of a few popular organic semiconductors and their applications

Depending on the device structure employed, the same organic material can be used for different functions. For example, single crystal rubrene displays the highest hole-mobilities in OTFTs and is also used as a dopant in the fabrication of white-light OLEDs due to its electroluminescent properties.

As the extent of conjugation increases in a molecule (i.e. the conjugated chain becomes longer), the HOMO and LUMO energy levels broaden into band-like states similar to the valence and conduction bands found in inorganic semiconductors. The origin of this band broadening is due to the Pauli exclusion principle that states that no two electrons can occupy the same quantum state simultaneously. In order to accommodate the increased number of π electrons, the π molecular orbitals split into multiple energy states. As a result of the broadening of the HOMO and LUMO bands, the band-gap of the molecule decreases as the conjugation increases.

Molecules with large conjugated groups typically show red shifted absorption and emission spectrums. Similarly, when many molecules are present in close proximity, such as in a thin-film, the HOMO and LUMO bands broaden even more, resulting in a further lowering of the band-gap energy. When the emission spectra of the same organic molecule in solution and film are compared, the emission of the film shows a red shift due to the lowering of the band-gap. The origin of the band splitting in thin-films is due to the stacking of the π -orbitals of neighbouring molecules on top of the each other, resulting in further energy level splitting.

When light is incident on an organic molecule, an electron from the HOMO is excited to the LUMO. The excited molecule has one electron in the LUMO and one electron in the HOMO. The vacant energy state left in the HOMO is known as a “hole”. The electron and hole are coulombically attracted to each other resulting in a formation of an electron-hole bound pair called an exciton. When excitons are formed in an organic film, they can recombine (radiatively or non-radiatively), diffuse through the film from molecule to molecule or dissociate into separate electron and hole charge carriers.

Exciton diffusion happens primarily through two energy transfer processes – Forester and Dexter energy transfer. Forester energy transfer relies on the creation of dipole moments in molecules neighboring the excited molecules. When the excited molecule relaxes, the energy is transferred to the neighboring molecule and therefore, an

exciton is created there. This relies on strong overlap between the emission and absorption spectra of the involved molecules and can happen over distances up to 10 nm. In Dexter energy transfer, an electron is directly transferred from the LUMO of an excited molecule to the LUMO of a neutral molecule. In exchange, a hole is transferred from the neutral molecule to the excited molecule. This process strongly depends on the distance between the molecules and the overlap of the molecular orbital wave functions and therefore happens over a very short distance, usually 5-10 angstroms.

Charge transport of free electrons and holes in organic semiconductor films can be divided into intra-molecular transport and inter-molecular transport. Intra-molecular transport of electrons and holes is extremely efficient due to the presence of a large number of delocalized band-like states. Inter-molecular transport is much less efficient because the free electrons and holes must “hop” over an energy barrier to be transferred to another molecule. This model of transport is commonly called “hopping transport” [12]. When the intermolecular distance is low and π -orbital overlap of neighbouring molecules is high, the energy barrier for transport is quite low and almost resembles band transport. However, when the intermolecular distance is high and π -orbital overlap is low, the energy barrier is high and charge transport occurs via hopping.

1.2 The Influence of Morphology and Molecular Orientation

In a thin-film of organic semiconductor, absorption, exciton diffusion and charge transport are heavily dependent on the morphology, order and orientation of the molecules in the film. The absorption of light by an organic molecule is dependent on the angle between the electric field of the incident photon and the transition dipole moment of the molecule [13]. If the transition dipole moment is parallel to the electric field of the incident photon, absorption is maximized. If the transition dipole moment is perpendicular to the electric field of the incident photon, absorption is minimized. Depending on the orientation of the molecules in the film and the angle of incident light, absorption can vary by several orders of magnitude for the same material.

The diffusion of excitons is heavily dependent on the crystallinity and grain size of the organic film [14]. If the molecules are arranged in polycrystalline domains, exciton diffusion length will be maximized due to lower intermolecular distance and increased spatial overlap between the molecular orbitals of neighbouring molecules resulting in efficient Dexter energy transfer. If there is significant disorder in the molecules of the organic film, exciton diffusion will primarily happen through the Forester mechanism and will be inefficient beyond 10 nm distances. Crystalline films show over four times greater exciton diffusion lengths than amorphous films of the same material.

Finally, charge transport in an organic film is also crucially dependent on the intermolecular distance and crystalline order in the film [12]. Molecules arranged in polycrystalline domains with large degree of π - π orbital stacking would show the best charge mobility in the π - π stacking direction. The charge mobility in the direction of π - π stacking in an organic film is typically several orders of magnitude higher than the charge mobility in the out-of-plane direction. Decreasing the intermolecular distance (which decreases the π - π stacking distance) and increasing the crystallinity of an organic film will serve to increase charge mobility in the film. Disordered films would have large “hopping” energy barriers due to low π -orbital overlap and large π - π distances that will reduce charge mobility in the film.

1.3 Device Structure and Operation of Organic Solar Cells

In order to obtain photovoltaic performance, the excitons generated in an organic semiconductor must be separated into free charge carriers and collected at different electrodes. Early renditions of organic solar cells consisted of one organic semiconductor sandwiched between an anode and cathode. One of the most commonly used materials for this purpose was metal-substituted phthalocyanines like copper phthalocyanine (CuPc) shown in Figure 2. In these early cells, the Schottky junction formed between the semiconductor and the metal electrode dissociated the excitons formed in the organic semiconductor. The current produced by these cells was quite low because the exciton

dissociation happened only at the metal/organic interface and some excitons were quenched by the metal [15].

In 1986, Tang introduced a double layer OSC comprising of a heterojunction formed between two different organic materials called the donor and acceptor [16]. The HOMO and LUMO energy levels of the donor and acceptor are staggered so that the donor energy levels are higher than the acceptor energy levels. In this so-called planar heterojunction (PHJ) OSC, exciton dissociation primarily happens due to charge transfer between the donor and acceptor species. Since the energy level offset between these two species was quite large, the exciton dissociation process was quite efficient and the current produced by these cells was greatly increased. Metal-substituted phthalocyanines are one of the most often used and well-studied donor materials and C₆₀ or C₇₀ fullerenes are the standardly used as acceptors.

Further improvement in OSC device performance came when these donor and acceptor materials were blended together to form bulk-heterojunctions (BHJ) [17]. BHJs increased the exciton diffusion area hence, the exciton dissociation rate and enabled even higher currents to be extracted from OSCs. However, due to the mixing of donor and acceptor materials, charge transport in BHJ OSCs is quite poor compared to planar junction OSCs since complete percolation paths for holes and electrons towards their respective electrodes are limited in number. In order to address this issue, planar mixed heterojunction (PMHJ) OSCs were fabricated where the BHJ layer was kept thin (10 nm at most) and sandwiched between neat donor and acceptor materials. The BHJ layer increased exciton dissociation and the neat donor and acceptor materials transported the charges to the electrodes efficiently.

In a typical OSC stack, the anode is transparent and made out of indium tin oxide (ITO). The cathode is usually a low work function metal with aluminum and silver being popular choices. Large efficiency increments in OSCs have been brought about by the use of anode and cathode interfacial layers. Anode interfacial layers such as molybdenum trioxide (MoO₃) increase the work function of the anode [18,19]. A large anode work

function allows for the formation of an ohmic contact between the anode and the donor material leading to better collection of holes. Cathode interfacial layers are also known as exciton blocking layers (EBL). The function of the EBL is to prevent damage to the underlying organic layers during cathode metal deposition and also prevent excitons from being quenched by the metal cathode [20,21].

Schematics of PHJ and BHJ OSCs with typical layer thicknesses are shown in Figure 3a and Figure 3b respectively.

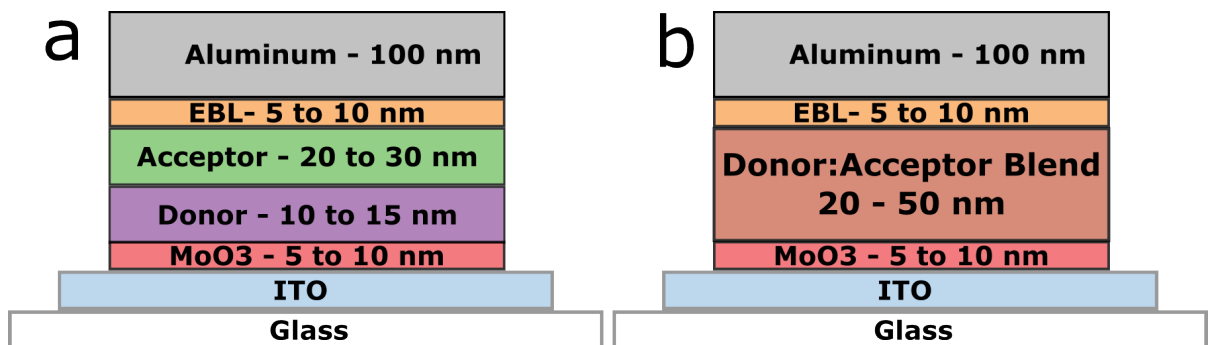


Figure 3: Schematic of a) PHJ OSC and b) BHJ OSC with typical thicknesses

In summary, the photogeneration processes inside a heterojunction organic solar cell can be stated as follows:

- i) Absorption of light and formation of excitons
- ii) Diffusion of exciton to donor/acceptor interface
- iii) Charge transfer and formation of a charge transfer exciton
- iv) Separation of charge transfer exciton into free charge carriers
- v) Drift of free charge carriers towards the electrodes influenced by the built-in electric field

1.4 Photovoltaic Performance of an Organic Solar Cell

The performance of organic solar cells is characterized by three important photovoltaic performance parameters – the short-circuit current density (J_{sc}), open-circuit voltage (V_{oc}) and fill-factor (FF). Figure 4 shows the photovoltaic parameters on an typical J-V plot [11].

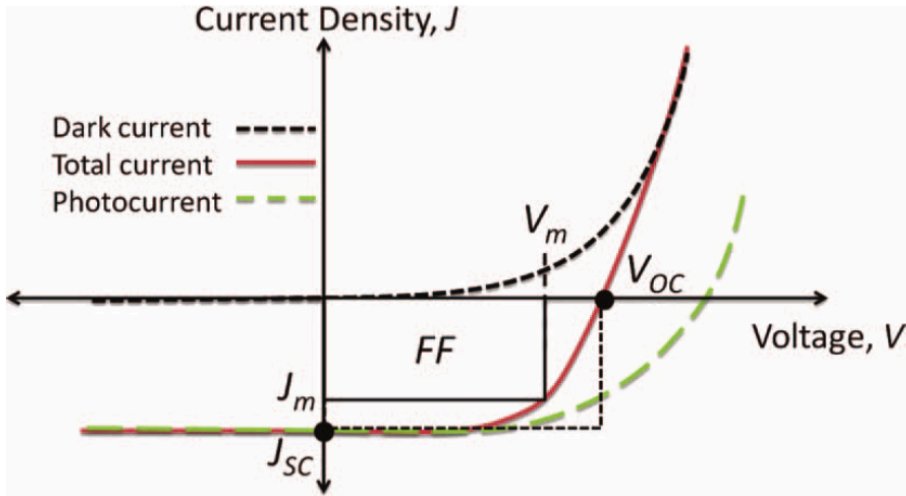


Figure 4: Photovoltaic parameters of a solar cell. Reproduced with permission from ref. [11]

The dark current is obtained by applying a sweeping voltage without illumination. The total current – which is a geometric sum of the dark and photocurrents - is obtained when the same voltage sweep of the device is carried under with illumination.

The J_{sc} represents the maximum photocurrent generated by the device and is defined as the current produced by the solar cell when the applied bias is 0 V. The V_{oc} refers to the maximum voltage developed across the electrodes of the solar cell and is defined as the voltage produced when the current flow across the solar cell is 0 A or when the photocurrent and dark current cancel each other out. The fill-factor is a measure of the square-ness of the J-V curve and is represented by the formula:

$$FF = \frac{J_{MAX}V_{MAX}}{J_{SC}V_{OC}}$$

Finally, the efficiency of the solar cell is given by the formula:

$$Efficiency (\eta) = \frac{J_{sc}V_{oc}FF}{P_0}$$

Where P_0 is the incident photon power intensity in Watts per meter squared.

1.5 Factors Limiting the Efficiency of Organic Solar Cells

Following from the previous mechanistic explanation of the operation of organic solar cells presented in Section 1.3, the factors affecting photocurrent generation in an OSC can be identified as:

- i) Absorption (Abs)
- ii) Excitation diffusion (ED)
- iii) Charge separation (CS)
- iv) Charge collection (CC)

Therefore, the efficiency of electron collection as a function of photon energy, called external quantum efficiency (EQE), can be represented as:

$$\eta_{EQE} = \eta_{Abs}\eta_{ED}\eta_{CS}\eta_{CC}$$

The absorption efficiency is an intrinsic property of the material and the morphology of the deposited thin-film. In a typical OSC, the absorption spectrum displays two broad regions of donor absorption and acceptor absorption but does not cover the entire spectrum of light incident on it. As such, this is one of the key factors for efficiency loss in a single-junction OSC. Secondly, as mentioned in Section 1.2, the absorption of an organic material is maximum when the electric field of the incident photon is parallel to the transition dipole moment (μ) of the organic molecule. In an OSC, this means that the organic molecules must be oriented with their transition dipole moments parallel to the substrate. The transition dipole moments of organic molecules are along the plane of the C=C back bones which means that the molecular plane must be

oriented parallel to the substrate to maximize the absorption of an organic molecule. Most common donor materials orient themselves with their molecular planes perpendicular or tilted to the substrate, which results in absorption loss. Finally, in an OSC, reflections between the anode and cathode gives rise to an interference pattern that affects the optical field distribution in the device and hence the absorption efficiency of the entire OSC stack. This distribution can be modeled by using the dielectric constant and the layer thicknesses [22].

The exciton diffusion efficiency is related to the exciton diffusion length in the material. It is an intrinsic property of the material as well as the morphology of the deposited thin-film and active layer. As mentioned in Section 1.2, highly ordered films have greater exciton diffusion lengths than amorphous films. Increasing the crystallinity and grain size of a donor or acceptor leads to greater exciton diffusion in that layer. As exciton diffusion length (L_D) increases, a larger number of excitons can get to the donor/acceptor interface and thus become dissociated. However, if the grain sizes are too big, then the exciton diffusion area will be reduced which can result in a decrease in exciton diffusion efficiency.

Exciton dissociation occurs by electron transfer from donor to acceptor molecules. An important factor affecting this charge transfer efficiency in a heterojunction OSC is the energy level offset between the donor and acceptor. A minimum of 0.2-0.3 eV offset is required for charge transfer in most cases [17,22]. If the offset is not sufficiently large, then the exciton dissociation efficiency drops tremendously. The charge transfer efficiency is also greatly dependent on the relative molecular orientations of the donor and acceptor materials [23]. For example, in a PHJ OSC composed of the archetypal donor material copper phthalocyanine (CuPc) and common electron acceptor (C_{60}), the charge transfer and subsequent exciton dissociation rate was found to be four times higher when the CuPc molecules were face-on with respect to the C_{60} molecules than edge-on. This suggests that increased π orbital overlap between donor and acceptor materials leads to increased charge transfer. In both PHJ and

BHJ OSCs, the relative orientations of donor and acceptor molecules are poorly controlled leading to suboptimal exciton dissociation efficiency.

Finally, the charge collection efficiency is dependent on the mobility of charges in the material and the nature of the organic/metal interface. As mentioned in Section 1.1, the mobility of charges in a material is critically dependent on the thin-film morphology of the deposited material. Ordered films with greater molecular orbital overlap and π - π stacking show greater charge carrier mobility than amorphous films. In order for maximum charge collection efficiency in an OSC, the π - π stacking direction must be perpendicular to the substrate so that the electrons and holes can have the best mobility to move towards to the cathode and anode respectively. However, the π - π stacking direction in most OSCs is poorly controlled and often is parallel to the substrate leading to large decrease in charge mobilities in the organic thin films. Increasing the crystallinity and grain-sizes of the organic materials also improves charge mobility and hence charge collection efficiency. In typical OSCs, the grain sizes are not well controlled resulting in sub-optimal charge collection efficiencies and lower FF.

The V_{oc} of heterojunction OSCs is determined by the difference between the energy levels of the HOMO of the donor and LUMO of the acceptor. This is the bandgap of the charge transfer exciton that is formed after dissociation. The commonly accepted formula in a heterojunction solar cell for the V_{oc} is given by:

$$V_{OC} = \frac{1}{e} (|E_{HOMO}^{donor}| - |E_{LUMO}^{acceptor}|) - 0.3V$$

The 0.3V factor represents energetic losses at organic/metal interfaces due to band bending and Fermi level pinning [24]. Increasing the V_{oc} requires increasing the charge transfer exciton band-gap and reducing interfacial losses. It is critically dependent on the intrinsic properties of the donor and acceptor materials and also on the morphology of the OSC. The relative orientations of donor and acceptor materials has also been shown to affect the V_{oc} [25]. Better donor/acceptor orbital overlap leads to easier charge transfer

and hence, reduced energetic losses within the cell. As a result, the V_{oc} is found to increase. Increasing crystallinity of the organic molecules can lower the band-gap due to increased π - π stacking. As a result, the V_{oc} could be reduced due to decreased bandgap of the charge transfer exciton. In most OSCs, the relative orientations of the donor and acceptor as well as the crystallinity of the deposited layers are poorly controlled, resulting in sub-optimal V_{oc} and efficiency.

There is a fundamental trade off between absorption, exciton dissociation and charge collection in OSCs. If the organic layers are made thicker in a PHJ OSC, the absorption increases but results in a drop in exciton dissociation due to lower number of excitons being able to reach the donor/acceptor interface. Charge collection also suffers because the dissociated free carriers have to travel additional distance through the organic materials. In a BHJ OSC, increasing the mixed layer thickness increases absorption but severely hampers charge collection due to low number of electron and hole percolation paths to the cathode and anode respectively. Large BHJ thicknesses increase the probability of electron and hole recombination since the charges have to travel an additional distance in the active layer to reach the electrodes.

1.6 Organic Solar Cell Materials and Fabrication Technologies

There are two main classes of organic semiconductor molecules that are used in organic solar cells – small molecules and polymers. Initially, research efforts were focused on polymer OSCs due to their promising performance. The most well studied polymer OSC system is composed of a thiophene backbone polymer, poly-3-hexylthiophene (P3HT) as the donor material and a fullerene derivative, 1-(3-methoxycarbonyl)propyl-1-phenyl[6,6]C₆₁ (PCBM), as the acceptor material. However, due to the identification of new small molecule semiconductors and better understanding of device physics and architectures, small-molecule based OSCs have matched and in some cases, exceeded the efficiency of polymer OSCs. The most well studied small molecule donor materials are metal-substituted phthalocyanines. C₆₀ or C₇₀ is commonly used as the acceptor in small molecule OSCs. Small molecules possess several

advantages over polymer materials. Namely, small molecule materials are easier to synthesize and purify in batch processes and have a well defined molecular structure [26]. Both polymer and small molecule OSCs report efficiencies reaching 8-10% [27–29]. The record efficiency holder for organic solar cells belongs to Heliatek GmbH who have demonstrated 12.0% efficiency with vacuum deposited tandem small molecule OSCs [7]. Polymer solar cells do not lag far behind with Mitsubishi Chemical claiming 11.1% [8].

Organic solar cells are fabricated either by vacuum deposition or solution processing. Vacuum deposition is applicable to fabricating OSCs with small molecules or oligomers that do not decompose before evaporating. Solution processing is compatible with polymer materials and small molecules with good solubility. There are several advantages and disadvantages to these two techniques that are summarized in

Table 1 [11].

Table 1: Comparison of Vacuum Thermal Evaporation and Solution Processing

Vacuum Thermal Evaporation	Solution Processing
Advantages: <ul style="list-style-type: none"> - Angstrom level thickness control - Ability to deposit multi-layer structures with little to no intermixing - Co-evaporation and fine percentage doping - Ability to deposit metals and inorganic materials such as dielectrics and salts 	Advantages: <ul style="list-style-type: none"> - Lower equipment costs due to lack of vacuum chambers - Less material waste - Simpler process that is compatible with large batch fabrication
Disadvantages: <ul style="list-style-type: none"> - Large quantities of wasted material due to isotropic evaporation - Expensive vacuum equipment and startup costs - Incompatible with materials that decompose before their evaporation temperature 	Disadvantages: <ul style="list-style-type: none"> - Lack of fine control over thickness and film uniformity - Multilayer structures only possible if solvent doesn't dissolve materials in the previous layer - Incompatible with materials that have low solubility

Chapter 2 - Background and Literature Review

Chapter Summary

In this chapter, a background and literature review of the following topics is provided:

- Phthalocyanine donors and fullerene acceptors
- Controlling the donor-acceptor ratio of bulk heterojunction OSCs
- Templating layers used in planar heterojunction OSCs

Phthalocyanine donors and fullerene acceptors are the most commonly used donor-acceptor material combination in OSC literature. Phthalocyanine donors are seen as the stereotypical small-molecule donor material and are widely used due to their ease of synthesis and purification, low cost and large variation in optical and electronic properties. Fullerene acceptors, such as C60 and C70, are the most commonly used acceptor material in literature because they have high electron mobility and possess ideal energy levels for dissociation of excitons formed in phthalocyanine donors.

The donor-acceptor ratio is a critical parameter that influences the efficiency of the bulk-heterojunction layer in a BHJ OSC by modifying the phase-separation and aggregation of donor or acceptor molecules. Excluding molecular design and modification of the donor-acceptor materials, controlling the donor-acceptor ratio is one of the main methods of modifying the morphology of the bulk heterojunction. However, existing explanations fail to explain the full extent of how varying the donor-acceptor ratio in a OSC affects its device physics, morphology and overall performance.

Templating layers are used to control the morphology and molecular orientation of phthalocyanine donor materials in planar heterojunction OSCs. When deposited on substrates without templating layers, phthalocyanines molecules arrange themselves with their molecular planes perpendicular to the substrate. However, when deposited on top of templating layers, phthalocyanine molecules lie with their molecular planes parallel to the substrate. Using templating layers is a simple method to study the effect of morphology

and molecular orientation on the performance of planar heterojunction OSCs. Since templating layers are a recent phenomenon, comprehensive studies on how templating layers affect the device physics of phthalocyanine PHJ OSCs have not yet been conducted.

2.1 Donor and Acceptor Materials

Most of the work in OSC literature has been focused on phthalocyanine based donor materials. Phthalocyanines are a versatile class of small molecules that are easily available and widely regarded as a stereotypical small-molecule donor material [1,2]. Substituting various metal atoms in the center of the phthalocyanine molecule can control various properties such as HOMO-LUMO energy levels, crystal structure and molecular orientation. Examples of single substituted divalent phthalocyanines are zinc phthalocyanine (ZnPc), copper phthalocyanine (CuPc) and lead phthalocyanine (PbPc). Double substituted trivalent phthalocyanines include chlorine aluminum phthalocyanine (ClAlPc) and chlorine indium phthalocyanine (ClInPc) and tetravalent phthalocyanines include titanium oxide phthalocyanine (TiOPc) and vanadium oxide phthalocyanine (VOPc). Vacuum deposited thin films of phthalocyanines are polycrystalline and show a herringbone packing structure which is considered a stereotypical morphology of many classes of small molecules. Figure 5 shows the molecular structure of un-substituted phthalocyanine and its herringbone packing structure with typical lattice spacings [3]. At room temperature, H₂Pc molecules orient themselves perpendicular to the substrate with their b-axis parallel to the substrate. The π - π stacking direction is along the b-axis phthalocyanine molecules. Therefore, phthalocyanines demonstrate their best optical and electrical properties along this axis.

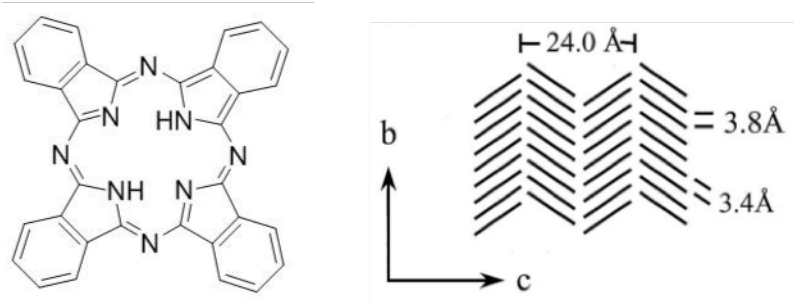


Figure 5: Molecular structure of un-substituted phthalocyanine and a schematic of its herringbone packing with typical lattice spacings. Adapted from ref. [3].

The crystal structure of phthalocyanines deposited on a substrate is determined by weak Van der waal's interactions between the phthalocyanine molecules and also the interaction between the phthalocyanine molecules and the substrate. As a result, different polymorphs of the same phthalocyanine material can be obtained depending on deposition conditions and post deposition treatment. This also makes phthalocyanines ideal candidates to study the influence of deposition conditions and post deposition treatments on film morphology and device performance. Therefore, a large portion of literature focuses on these materials.

Fullerenes (C_{60} and C_{70}) are commonly used as acceptor materials in literature due to their high performance and common availability. Due to the deep HOMO and LUMO levels of fullerenes, they are efficient exciton dissociating acceptors when paired with many donor materials and due to extensive charge delocalization, they possess high electron mobility. As a result, fullerenes are very versatile and can be used in almost any device structure. Also, due to their spherical shape, their absorption and charge transport properties are isotropic which helps limit the number of variables when studying the properties of a phthalocyanine/ C_{60} OSC.

2.2 Donor Acceptor Ratio

The donor-acceptor ratio is a critical parameter that influences the efficiency of a bulk heterojunction OSC. Despite being easy to control, the effect of the donor acceptor

ratio on the BHJ morphology and OSC performance has not been studied thoroughly. Most of the few works in literature have focused on phthalocyanine and C₆₀ BHJ OSCs. In general, the donor-acceptor ratio controls the phase separation and aggregation of the donor and acceptor materials. At very high concentrations of either the donor or acceptor material, the material that is present in lower concentration tends to phase separate out of the mixture.

Sullivan *et. al.* first reported that the morphology of 1:1 CuPc:C₆₀ mixed layer is amorphous with no significant evidence of phase segregation [4]. By comparing CuPc:C₆₀ mixed layer absorption spectra with neat CuPc and CuPc in solution, they proposed that phase separation isn't significant unless either the donor or acceptor is present at very high concentrations (>75%). A follow-up work by Heutz *et. al.* observed that phase separation is significant at 25% CuPc concentration. Large crystallites of either CuPc or C₆₀ were observed via atomic force microscopy (AFM) imaging at 25% CuPc concentration. Interestingly, phase separation wasn't observed at 75% CuPc concentration indicating that the CuPc aggregation is strongly disrupted by the introduction of small concentrations of C₆₀ in the mixed layer. Optimum CuPc:C₆₀ OSC performance was observed at 75% CuPc concentration in the mixed layer indicating that the charge mobilities in the OSC were balanced at this mixing ratio. Opitz *et. al.* measured the field effect mobilities as a function of CuPc:C₆₀ mixing ratio [5]. At 1:1 CuPc:C₆₀ mixing ratio, the electron mobility was in the order of 10⁻³ whereas the hole mobility was on the order of 10⁻⁶. At 3:1 CuPc:C₆₀ concentration, the hole and electron mobilities were both on the order for 10⁻⁴. They also observed phase separation at 1:1 CuPc:C₆₀ mixing ratio when deposited on heated substrates at T_{sub} = 375 K. Higher CuPc concentrations (3:1 CuPc:C₆₀) still did not show significant phase separation even at elevated substrate temperature.

Significant interest in studying the effect of the donor-acceptor ratio was generated when Zhang *et. al.* demonstrated donor:fullerene OSCs with surprisingly high efficiencies (>5.0%) utilizing mixed layers with very low donor concentration (5% donor) [6]. A wide variety of donor materials were able to provide high performance as

long as the donor concentration was kept very low and the acceptor used was either C₆₀ or C₇₀. The high performance of these cells was partly attributed to the high V_{oc} arising from the formation of a Schottky junction between a high-workfunction anode and the fullerene. The J_{sc} of these low donor concentration cells is also much higher compared to cells with higher donor concentration.

Several groups have attributed this increase in J_{sc} to more efficient phase separation and balance of charge mobilities when the donor material is present in low concentrations. Pandey *et. al.* found that phase separation was present at 20% SubPc concentration in a SubPc:C₆₀ blend layer using transmission electron microscopy (TEM) [7]. Both 10% SubPc concentration and 50% SubPc concentration showed amorphous films. Zheng *et. al.* reported similar observations for 5% tris[4-(5-phenylthiophen-2-yl)phenyl]amine (TPTPA):C₇₀ blends [8]. Using cross-sectional TEM, they found 20 nm sized domains of C₇₀ and 4 nm sized domains of TPTPA in 5% TPTPA:C₇₀ blend layers. Figure 6 shows the cross-sectional TEM images of 5% TPTPA:C₇₀ OSCs from ref. [8]. The white domains belong to C₇₀ while the black dots belong to TPTPA. In a follow up study, they reported similar observations with low concentration pentacene and dinaphthothieonothiophene (DNNT) mixtures with C₇₀ [9]. One of the reasons for the surprising performance of these low-donor concentration OSCs is due to the nano-scale phase separation between donor and acceptor and the resulting balance of charge carrier mobilities.

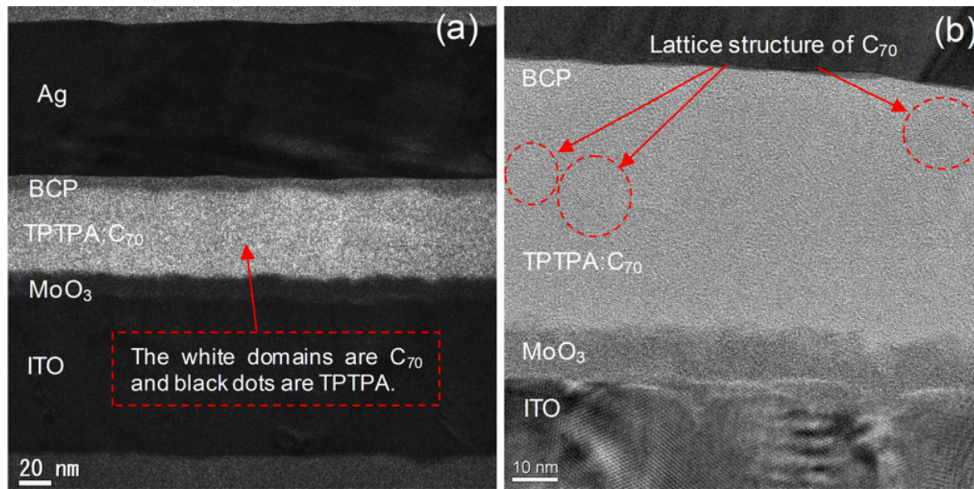


Figure 6: Cross-sectional TEM of TPTPA:C70 OSCs at 5% TPTPA Concentration. Reproduced with permission from ref. [8]

2.2.1 Unanswered Questions

Phase separation and balanced charge carrier mobilities cannot completely explain the large increase in J_{sc} in low-donor concentration OSCs. When the donor concentration decreases, the absorption by the donor molecules also decreases. Since the donor absorption plays a large role in determining the photocurrent of the OSC, the J_{sc} should decrease as the donor concentration decreases. Furthermore, as the donor concentration decreases, the percolation path of holes to the anode should also decrease leading to higher recombination and further reduction of J_{sc} and FF. However, the inverse effect is observed in these low-donor concentration OSCs and there are no mechanistic explanations for this phenomenon in literature. More research is required in order to examine the reasons behind varying J_{sc} as a function of donor/acceptor ratio and whether the morphology of the mixed layer contributes to this effect. The first objective of this research work is to answer this question.

Secondly, mixed donor-acceptor layers are found in a wide variety of OSC device architectures such as the planar-mixed heterojunction (PMHJ) where the mixed layer is sandwiched between neat layers of donor and acceptor materials. The PMHJ architecture

has shown to improve the fill factor of OSCs to a great extent due to better charge transport properties arising from the use of the neat layers. In addition to the PMHJ, hybrid devices such as a BHJ with a neat electron-transport layer or a BHJ with a neat hole-transport layer have also been used in literature with a variety of materials. However, there are no studies in literature that examine the effect of varying the donor-acceptor mixing ratio in all of these device architectures. The device physics of an OSC varies greatly depending on the device architecture used. Conclusions drawn about the effect of the donor-acceptor mixing ratio in any one of the device architectures might not necessarily ring true for the others. Therefore, in order to completely understand the effect of the donor-acceptor mixing ratio and its associated morphological changes on the performance of OSCs, it is necessary to investigate all possible OSC device architectures. Examining the effect of varying the donor-acceptor ratio in all OSC device architectures is the second objective of this research work.

2.3 Templating Layers

Molecular templating refers to the phenomenon in which the morphology of the template layer substantially influences the morphology of the layers deposited on top. The templating phenomenon has been studied quite extensively in literature, mostly in phthalocyanine materials. The molecular orientation and crystal structure of vacuum deposited polycrystalline organic materials are determined by molecule-molecule interactions and molecule-substrate interactions. In phthalocyanines, the interaction between phthalocyanines and the templating layer are much stronger than the interactions between other phthalocyanine molecules. As a result, the molecular orientation of the first deposited phthalocyanine layer is affected by the presence of the templating layer. This effect then propagates to subsequently deposited phthalocyanine molecules.

Bayliss *et. al.* first reported its observation in H₂Pc films in the year 2000 [10]. They grew three different phases of H₂Pc film by deposition at room temperature (α phase), room temperature deposition followed by annealing at 320⁰C for 2 h (β_1 phase) and deposition on heated substrates at $T_{\text{sub}} = 330^{\circ}\text{C}$ (β_2 phase). Subsequently, they

examined the effect of growing α -H₂Pc on top of an underlayer of β_1 and β_2 H₂Pc as well as the effect of growing β_1 -H₂Pc on β_2 -H₂Pc and β_2 -H₂Pc on β_1 -H₂Pc. In all cases, they found that the film grown on top had adopted the same phase as the film underneath which firmly suggested that the first deposited layer acted as a molecular template for all subsequent layers.

In a follow up work, Heutz *et. al.* found that perylene-3, 4, 9, 10-tetracarboxylic dianhydride (PTCDA) can strongly template H₂Pc [3]. When deposited on a substrate at room temperature, H₂Pc is obtained in its α -phase where the molecules are packed in a herringbone structure with the molecular planes perpendicular to the substrate. When deposited on PTCDA, H₂Pc adopts an extremely different crystal structure where its molecules lie parallel to the substrate, similar to that of the PTCDA molecules. Figure 7a shows the top down view of a PTCDA unit cell on a substrate and Figure 7b shows the top down view of H₂Pc stacking when deposited on a substrate at room temperature [3]. Figure 7c shows the side view of H₂Pc when deposited on top of PTCDA highlighting the change in molecular orientation from perpendicular to the parallel to the substrate [3]. Interestingly, when PTCDA was deposited on top of α -H₂Pc, the crystal stacking of PTCDA was inhibited to such an extent that it was x-ray amorphous. Heutz also found that the templating effect extended for thick films – a 15 nm film of PTCDA was enough to template a 190 nm thick film of H₂Pc.

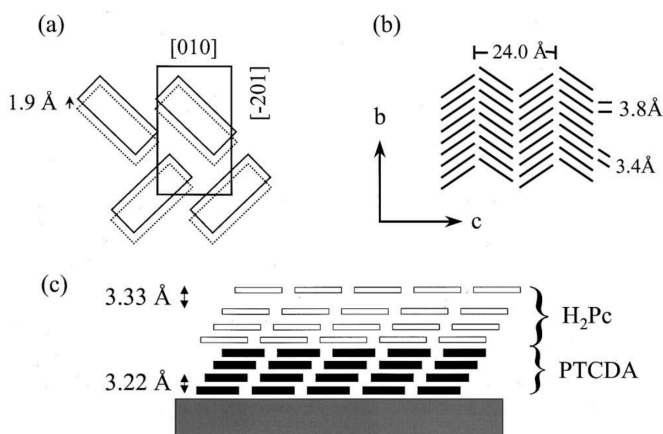


Figure 7: a) Top down view of PTCDA on substrate, b) Top down view of H₂Pc on substrate, c) Side view of H₂Pc grown on PTCDA. Reproduced with permission from ref. [3]

When PTCDA is deposited at room temperature on KCl substrates, the molecules lie flat on the substrate with a tilt of approximately 90° along the long axes as shown in Figure 7a [3,11]. PTCDA grows in a layer-by-layer fashion completely covering the available substrate area before another monolayer is formed. When H₂Pc is deposited on top of the PTCDA, it adopts the same face-on molecular orientation and the layer-by-layer growth mode due to strong intermolecular interactions between H₂Pc and PTCDA [30].

In 2002, Heutz *et. al.* followed up on their previous work and found that when PTCDA was grown on β_1 -H₂Pc, the PTCDA layer grew as elongated crystallites on top of β_1 -H₂Pc domains [12]. The structure of PTCDA was not disrupted as in the case with growing PTCDA on top of α -H₂Pc. They also found that neither H₂Pc nor PTCDA under layers affected the structure of Alq₃, which is an amorphous material. Sakurai *et. al.* found that depositing H₂Pc on PTCDA layers as thin as 0.5 nm was enough to change its molecular orientation [13,14]. However, as the PTCDA layer thickness decreased, the molecular tilt angle of H₂Pc relative to the substrate increased. With no PTCDA, H₂Pc molecules are tilted an average of 54 relative to the substrate. On top of 0.5 nm PTCDA, the H₂Pc mean tilt angle reduces drastically to 32° . When the PTCDA thickness is increased to 1.5 nm, the H₂Pc mean tilt angle decreases further to 27° – which corresponds to the b-axis (Figure 7) of the H₂Pc crystals lying perpendicular to the substrate. The reason for the large shift in H₂Pc molecular orientation for thin layers of PTCDA was attributed to the excellent surface coverage of PTCDA molecules even at small thicknesses. In 2007, Sakurai *et. al.* also demonstrated that the molecular orientation of 1:1 H₂Pc:PTCDA mixtures was also parallel to the substrate when deposited on a PTCDA templating layer [15]. When the mixing ratio was increased in favor of H₂Pc to 4:1 H₂Pc:PTCDA, the molecular orientation of H₂Pc reverted back to being perpendicular to the substrate. Also, when 1:1 H₂Pc:PTCDA was deposited on top of neat H₂Pc, the orientation of the molecules in the mixed layer was random.

Sullivan *et. al.* studied the effect of templating layers in CuPc:C₆₀ PHJ OSCs in 2007 [16]. They found that the J_{sc} increased from 2.5 mA/cm² for control cells with no

PTCDA templating layer to over 4.0 mA/cm^2 for OSCs with 1 nm PTCDA templating layer. The increase in J_{sc} was attributed to a significant increase in absorption from the CuPc molecules being oriented parallel to the substrate and the electric field of the incident photons when deposited on PTCDA templates. However, the V_{oc} decreased substantially from 0.5 V for controls to 0.4 V for devices with 1 nm PTCDA templating layer. The drop in the V_{oc} upon the introduction of PTCDA templating layer was attributed to charge build up at the anode interface. The energy levels of PTCDA align poorly with that of CuPc leading to significant accumulation of holes at the PTCDA/CuPc interface. Due to the increase in J_{sc} , the efficiency of PTCDA templated OSCs reached 0.81% whereas the control OSCs only demonstrated 0.73% efficiency.

Lassiter *et. al.* studied the performance of CuPc and C_{60} OSCs using PTCDA and diindenoperylene (DIP) as templating layers in PHJ and PMHJ configurations [17]. When CuPc was deposited on PTCDA or DIP, the RMS surface roughness increases from 1.8 nm to 3.9 nm. However, when a thin layer of DIP is deposited on PTCDA before CuPc, the CuPc roughness increases to 6.8 nm and the CuPc islands are approximately 100 nm in size. In PHJ configuration, the OSC performance was unaffected when DIP was used as the sole templating layer. When PTCDA was used as the templating layer, the J_{sc} and V_{oc} increased leading to an efficiency of 1.76% compared to the 1.42% of controls. However, when DIP was deposited on top of PTCDA before CuPc deposition, the PHJ OSC efficiency increased to 2.19% primarily due to increases in J_{sc} . The DIP was suggested to perform the role of an anode exciton blocker that prevents excitons from being quenched by the ITO. The additional excitons can then be dissociated in the OSC to generate increased photocurrent. DIP also enhances the templating effect of the PTCDA and increases the surface roughness of CuPc which provides more intermixing between CuPc and C_{60} . In a PMHJ, the use of PTCDA/DIP templating/exciton blocking layer increased the efficiency from 1.89% to 2.49%.

In addition to the extensive body of work on PTCDA templating layers, copper iodide (CuI) templating layers have received significant attention recently. In 2010, Cheng *et. al.* reported that CuI can be used to control the molecular orientation of CuPc

and hence improve the performance of CuPc/C₆₀ PHJ OSCs [18]. A thin (1-3 nm) of CuI deposited between ITO and CuPc is enough to change the CuPc molecular orientation from edge-on to face-on. This is because CuI interacts strongly with CuPc molecules that overpowers the molecule-molecule interactions and forces the CuPc molecules to adopt a face-on orientation. When CuPc was deposited on CuI, Cheng *et. al.* observed an increase in absorption intensity and a slight broadening of the absorption band indicating that the π - π stacking distance has been reduced. In CuI templated PHJ and PMHJ OSCs, the J_{sc} and FF increase substantially to provide a large improvement in efficiency. PHJ OSC efficiency increased from 1.03% for controls to 1.76% for CuI templated PHJ and PMHJ OSC efficiency increased from 1.49% to 2.55% for CuI templated PMHJ. Cheng *et. al.* also observed that the CuI templating layer increased the work function of ITO by 0.7 eV, similar to the action of MoO₃, which enhances hole extraction from CuPc.

Bernede *et. al.* studied the use of MoO₃/CuI anode interlayers extensively with thiophene-based donor materials [19,20]. They found that the MoO₃/CuI interlayers enhanced the performance of PHJ OSCs using terthiophene-pyran-malononitrile (T3PM) and the 5-[2,6-bis(E-2-{3',4'-di-n-hexyl[2,2':5',2''-terthiophen]-5-yl} vinyl)-4H-pyran-4-ylidene]pyrimidine-2,4,6(1H,3H,5H)trione (TTB) as the donor material. The performance enhancement was attributed to a decrease in the ITO work-function and reduction in donor surface roughness due to the presence of CuI.

Cattin *et. al.* also studied the use of MoO₃/CuI with CuPc/C₆₀ OSCs [19]. They found that the deposition rate of CuI was crucial to achieving templating effects that are beneficial to OSC performance. Lowering CuI deposition rates led to better templating effects and a greater increase in all PV properties. The highest OSC efficiency (1.75%) was obtained when the CuI was deposited at 0.05 Å/s with a J_{sc} of 6.76 mA/cm², V_{oc} of 0.5V and FF of 53%. When the CuI deposition rate increased to 0.1 Å/s, the J_{sc} (4.9 mA/cm²), V_{oc} (0.35 V) and FF (42%) all decreased significantly. At a CuI deposition rate of 0.5 Å/s, the J_{sc} (2.21 mA/cm²), V_{oc} (0.24 V) and FF (34%) was lower than controls with no CuI. When CuI is deposited at a low rate, the surface of the ITO/CuI anode is homogeneous with very low surface roughness. However, when the CuI is deposited at a

high rate, the surface is marked with large CuI crystallites as thick as 100 nm. The large CuI crystallites can create micro-shorts in the OSC and therefore reduce efficiency.

Rand *et al.* studied the effect of CuI templating layers on ZnPc/C₆₀ PHJ OSCs [21]. They found that the exciton transfer rate in the face-on ZnPc improved more than five times but due to the close stacking of the face-on ZnPc, the excitation diffusion length was reduced from 26 nm to 15 nm. The formation of charge transfer state with C₆₀ was also improved for face-on ZnPc. In terms of absorption, the face-on ZnPc demonstrated a 30% increase in absorption strength but due to the presence of interference effects in OSCs, the absorption enhancement was limited to 12%.

Lee *et al.* compared the performance of CuI, CuBr and CuCl templating layers in a ZnPc/C₆₀ OSC [22]. They found that CuI performed best (in terms of J_{sc} increase) as the templating layer for ZnPc compared to CuBr and CuCl. CuCl and CuBr templating layers have deeper HOMO levels than CuI that present a hole-extraction barrier at the ITO/CuX/ZnPc interface. Jang-Joo Kim's group studied the effect of CuI and CuBr templating with CuPc, ZnPc and PbPc [23–26]. For all M-Pcs, the molecular orientation was shifted from edge-on to face-on when deposited on CuI. They also reported that the CTE bandgap between ZnPc and C₆₀ was 1.10 eV for CuI templated ZnPc compared to 0.90 eV for controls with no CuI. This explains the small increase in V_{oc} commonly observed for CuI templated PHJ OSCs. Finally, they also found that CuI interlayers template C₇₀ deposited on top of CuI/PbPc. The CuI/PbPc layer encourages the C₇₀ to preferentially adopt the fcc phase with (220) orientation which greatly increases the crystallinity of the C₇₀ layer. As a result, the absorption due to C₇₀ aggregates increases and the exciton diffusion length in C₇₀ increases from 6.9 nm to 13.8 nm. Vasseur *et al.* reported similar observations with CuI/PbPc/C₆₀ devices and their EQE data indicated that the fullerene templating effect is observed with C₆₀ as well [27].

In an extremely detailed work studying the growth of FePc on CuI, Rochford *et al.* observed that CuI was always present as CuI (111) regardless of substrate temperature [28]. However, at room temperature, the CuI was a polycrystalline film showing very low

surface roughness. As the substrate temperature increased, CuI switched to an island growth mode producing visible islands of various sizes and heights. They also noted that the presence of CuI encouraged the formation of face-o (311) FePc. The stacking habit of FePc on bare SiO₂ and on SiO₂/CuI substrate is shown in Figure 8 [28].

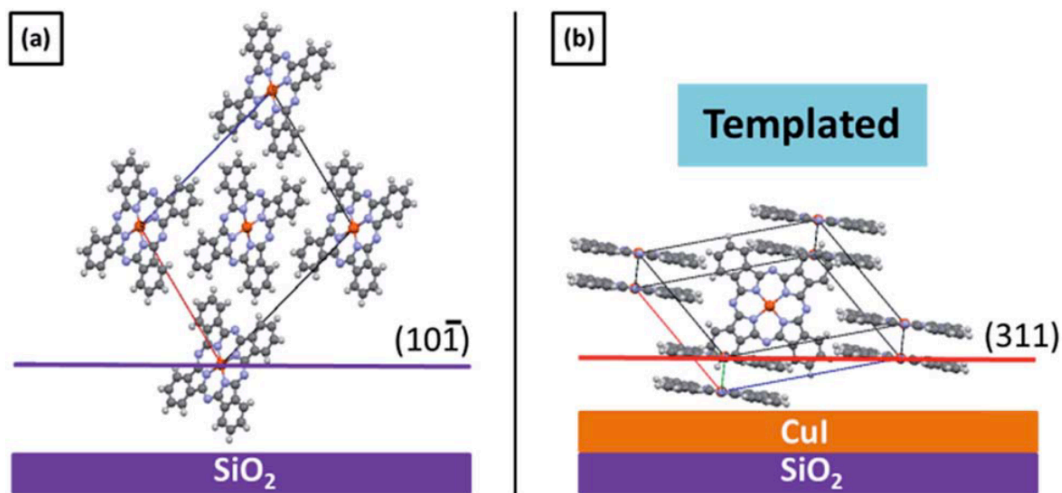


Figure 8: Stacking of FePc on a) Bare SiO₂ and b) SiO₂/CuI template layer. Reproduced with permission from ref. [28]. Published by The Royal Society of Chemistry.

In a follow up study, Rochford *et. al.* showed that when FePc was deposited on a CuI film composed of isolated islands, the FePc molecules preferentially nucleated at the edges of the islands and grew into high aspect ratio crystallites [29]. Further FePc deposition led to the formation of different FePc polymorphs.

2.3.1 Unanswered Questions

Despite the extensive body of work on templating layers, the effect of templating layers on hole mobility has not been studied, which prevents a complete understanding of the effect of templating layers on the device physics of PHJ OSCs. The third objective of this work is to examine the effect of templating on hole mobility in phthalocyanines and associated changes in PHJ OSC device physics.

Furthermore, the differences between PTCDA and CuI templating layers have not been studied for the same set of materials. PTCDA is a small-molecule that lies flat when deposited on a substrate. As a result, it templates any subsequent deposited material to lie flat on the substrate as well. CuI, on the other hand, works best as a templating layer when deposited at low deposition rates and in thin layers (1 -2 nm) where complete substrate coverage is not expected. Any subsequently deposited layer shows changes in orientation and morphology due to increased interactions between the deposited molecules and CuI. Due to the material differences between PTCDA and CuI, it is expected that the final morphology of the templated layer will be different which could result in differences in templated OSC performance. Also, templating layers have been exclusively studied with divalent phthalocyanines such as ZnPc, CuPc and PbPc. There has been little work studying the performance of templating layers with other high performance phthalocyanines such as ClInPc, ClAlPc and SubPc. Since the morphology of the phthalocyanines varies depending on the substituted metal atoms, studying templating behavior in different phthalocyanines provides a way to correlate templated morphology changes to OSC performance. The fourth objective of this research work is to examine the differences between templating performance of PTCDA and CuI across a broader range of phthalocyanines.

Finally, the effect of templating layers on the degradation behavior of planar heterojunction OSCs has not been studied in literature. The use of templating layers allows us to study the influence of morphology and molecular orientation on degradation behavior for the same donor/acceptor system without the need for molecular modification. The fifth and final objective of this research work is to examine the influence of templating on the degradation behavior of PHJ OSCs.

Chapter 3 – Objectives

The objectives of this research work are to examine the unanswered questions established in Sections 2.2.1 and 2.3.1. They are summarized here as follows:

1. Determine the role of the donor material in high-fullerene concentration Schottky-junction organic solar cells
2. Examine the role of the donor-acceptor mixing ratio and associated morphological changes in all organic solar cell device architectures
3. Determine the effect of molecular templating on hole mobility of phthalocyanine/C60 planar heterojunction OSCs and examine associated changes in device physics
4. Compare the templating efficacy of the two common templating layers, CuI and PTCDA, across a wider variety of phthalocyanine donor materials
5. Investigate the degradation behavior of templated phthalocyanine/C60 planar heterojunction OSCs

Chapter 4 – Research Methodology and Experimental Procedures

4.1 Research Methodology

The general objective of this research work is to examine the relationship between morphology of organic semiconductors and their effect on organic solar cell performance. Therefore, the research methodology in this work is focused on i) fabricating and characterizing organic solar cells and ii) characterizing the morphology of relevant organic semiconductor layers.

Phthalocyanines and fullerenes are used as donors and acceptors respectively in this work owing to their stereotypical donor-acceptor properties outlined in Section 2.1 and also because they are the main donor-acceptor system used in literature relevant to the objectives, as shown in Section 2.2 and 2.3. Vacuum deposition is used to fabricate the OSCs because the layer thicknesses and compositions can be precisely controlled. This is a crucial necessity in order to examine the influence of molecular orientation, morphology and device structure on OSC performance. The photovoltaic performance of the fabricated OSCs are characterized under AM1.5G illumination calibrated to 1000 mW/cm² according to standard procedure in the field. Insights into absorption, exciton generation, exciton dissociation and charge transport are gained by measuring the wavelength dependent performance of the OSCs in the form of UV/visible absorption spectra and external quantum efficiency spectra. Charge transport is further examined by measuring the hole and electron conductivity of individual organic layers using unipolar device architectures.

The morphology of the relevant active layers is characterized directly using atomic force microscopy, which provides insights into the roughness and crystallinity of the organic layer. Information about the relative molecular orientations in the organic layer is inferred mainly from the UV/visible spectra of the materials. By correlating the PV performance, EQE, UV/Vis absorption, unipolar device data and AFM image

analysis, a comprehensive picture of the dependence of OSC performance on organic semiconductor morphology can be obtained.

4.2 Basic Device Fabrication Procedure

The basic device structure of OSCs is given in Section 1.3 of the introduction. All OSCs are fabricated by vacuum evaporation in a custom built six-source thermal evaporator. The evaporation chamber is attached to the substrate chamber via a load-lock and the entire setup is pumped down to a minimum base pressure of 5×10^{-6} torr. The materials to be evaporated are contained in a tantalum evaporation boat and attached to two electrodes of the thermal evaporator. A high amperage AC current is applied between the electrodes that results in resistive heating of the tantalum boats and subsequent evaporation of the organic materials. Quartz crystal monitors (QCM) placed above the evaporation source are used to measure the film thickness and evaporation rate. The thicknesses of the films are calibrated using a stylus profilometer. A simple schematic of a vacuum evaporation chamber is shown in Figure 9 [1].

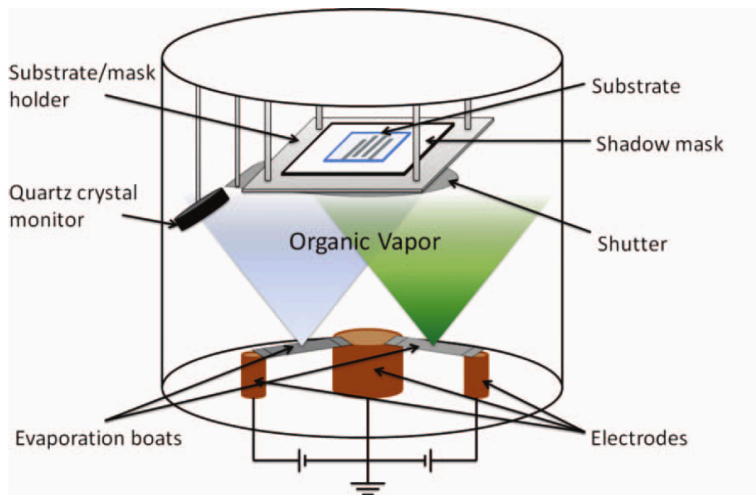


Figure 9: Schematic of a thermal evaporation chamber. Reproduced with permission from ref. [1]

The mean free path (MFP) of the evaporated organic materials in the chamber is given by the following formula [11]:

$$MFP = \frac{k_B T}{\sqrt{2} * P_{dep} * \pi d^2}$$

where P_{dep} is the deposition pressure and πd^2 is the collision area between molecules assuming that they have a spherical geometry. The MFP of organic molecules in a thermal deposition system is much greater than the source-to-substrate distance at 5×10^{-6} torr. As a result, the deposition of the material depends on the line-of-sight between the evaporation plume and the substrate and a shadow-mask is used to define the area in which the material is deposited.

A 2''x2'' glass substrate with commercially patterned ITO pads is used for all devices. A schematic of the substrate is shown in Figure 10.

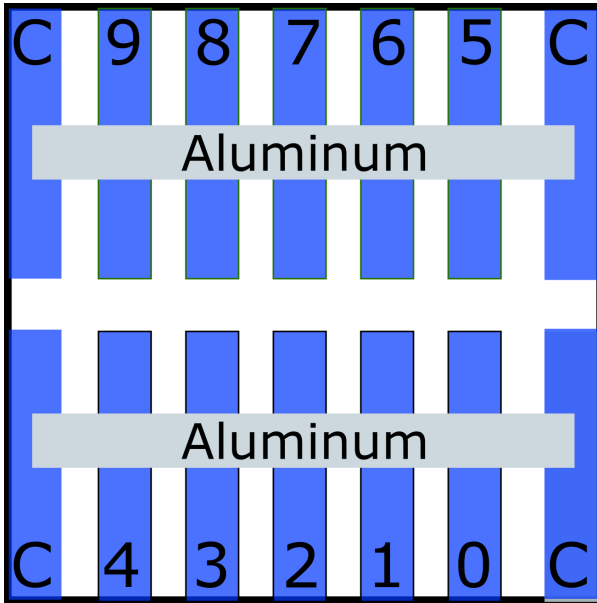


Figure 10: Schematic of the substrate used for OSC fabrication

The blue rectangles denote the ITO pads and the silver rectangles denote the aluminum metal deposited on top as the cathode. The ITO pads labeled with “C” serve as the cathode contacts. The numbered ITO pads are the anode contacts of the devices. Each

device can accommodate 10 devices. Due to the arrangement of the shadow mask, the devices in the same column are duplicates. For example, device 0/5, device 1/6 and so on are duplicates. The intersection of the aluminum cathode and the anode ITO pad defines an active device area of 0.2 cm^2 .

The general OSC fabrication procedure is as follows:

1. Load materials in evaporation chamber (donor, acceptor, exciton blocking layer, anode buffer layer and aluminum) and pump down to base pressure
2. Clean substrate by subsequent sonication in acetone, micro-90 detergent and isopropanol
3. Let substrate dry by placing in an oven at 110°C for at least 1 hour
4. Load substrate into the substrate chamber and pump down to base pressure
5. Adjust shadow mask to expose certain areas of the substrate depending on device structure and experiment design
6. Apply power to material source to evaporate organic material
7. Once desired evaporation rate is achieved, open shutter to deposit material on the substrate
8. Close shutter once desired thickness is reached and then turn off power to the material boat

In order to fabricate a PHJ OSC, MoO_3 is deposited first, followed by the donor material, acceptor, exciton blocking layer and cathode. In order to fabricate a BHJ OSC, the donor and acceptor materials are evaporated simultaneously at different rates depending on the desired BHJ composition. The deposition rate of organic materials is usually ranges from 0.5 to 2 \AA/s unless otherwise mentioned. The deposition rate of MoO_3 is usually 0.05 to 0.1 \AA/s . Aluminum is deposited anywhere from 2 to 4 \AA/s .

4.3 Basic Characterization Procedure

Electrical characterization of the fabricated OSC is done under dry and inert nitrogen gas flow to prevent moisture and oxygen related degradation. To this end, the

OSCs are placed in a sealed test-box under nitrogen gas flow. The test box has a window cut out to allow for the OSC to be exposed to light. The anode ITO pads are contacted by pushpins attached to a 10-position rotary switch that carries the signal to the center pin of a BNC terminal. The cathode ITO pads are contacted by pushpins that are shorted out and soldered to the outer casing of the BNC terminal. In this way, each individual device on the substrate can be tested independently.

Photovoltaic parameters of the OSCs are measured under 1000 mW/cm^2 AM1.5G radiation output from a ABET Sun 3000 Class AAA solar simulator. A Keithley 2400 SourceMeter is used to obtain the current-voltage characteristics of the OSC under illumination or in the dark. Commercially available software is used to calculate the fill-factor and efficiency from the I-V data. External quantum efficiency measurements are performed using a custom-built setup that consists of a Newport mercury lamp, Oriel Cornerstone 260 1/4m monochromator, optical chopper and SR830 lock-in amplifier. The OSCs are exposed to monochromatic light in 2 nm steps chopped at 100 Hz. The resulting photocurrent is output to the SR830 lock-in amplifier and converted to EQE by comparing to a silicon reference solar cell. The data is plotted using custom-built LABVIEW software. UV/Visible absorption measurements are performed in air in a Shimadzu UV-2501 PC UV/Vis spectrophotometer. A VEECO Dimension 3100 model AFM in tapping mode is used to image the surface profile of deposited films and OSCs. The typical scan areas are $1 \mu\text{m} \times 1 \mu\text{m}$, $5 \mu\text{m} \times 5 \mu\text{m}$ and $10 \mu\text{m} \times 10 \mu\text{m}$. RMS surface roughness over these scan areas is obtained using commercial software.

Chapter 5 - Role of the Donor Material and the Donor-Acceptor Mixing Ratio in Increasing the Efficiency of Schottky Junction Organic Solar Cells

Authors: Sibi Sutti, Graeme Williams and Hany Aziz

Published in: Organic Electronics, vol. 14, iss. 10, pp. 2392-2400, 2013. Reproduced with permission.

Chapter Summary

The first objective of this research work – to examine the role of the donor-acceptor mixing ratio in affecting the morphology and performance of OSCs – is addressed in this chapter. The donor-acceptor mixing ratio is varied between 1:1, as in a traditional BHJ OSC and 1:9 as in a Schottky junction OSC. Schottky junction OSCs employ a high work-function anode and an active layer comprised of fullerene and low concentrations of donor. In this study, the roles of the donor material and the donor-acceptor mixing ratio in Schottky junction OSCs are explored. The results show that the high short circuit current (J_{sc}) seen in Schottky junction OSCs at low donor concentrations arises primarily from photocurrent contributions from charge-transfer intermolecular states in C_{60} aggregates. These aggregates absorb light at 400-600nm and are thus well matched to the solar spectrum. The presence of the donor molecules is shown to be necessary for the dissociation of the C_{60} aggregate excitons, which ultimately allows for enhanced photocurrents. The exciton dissociation process is governed primarily by the highest occupied molecular orbital (HOMO) energy level difference between the donor and C_{60} , and is only efficient when this difference is large enough for the energetically favorable transfer of holes from C_{60} to the donor material. Increasing the donor concentration beyond a certain threshold hinders C_{60} aggregate formation and thus removes its contribution to photocurrent completely. Furthermore, the V_{oc} is shown to be strongly influenced by the choice of donor material, indicating that it is not set by

the Schottky junction barrier height as previously thought. In spite of this influence on V_{oc} , the choice of donor does not appear to play a significant role in the extraction of holes from the Schottky junction organic solar cells.

5.1 Introduction

Until recently, the planar-mixed molecular heterojunction (PMHJ) was considered the state of the art in device architecture for SM-OSCs [1]. In a PMHJ device, a bulk-heterojunction (BHJ) mixture of donor and acceptor species is sandwiched between neat donor and acceptor layers [2,3]. The BHJ greatly enhances exciton dissociation efficiency due to presence of a large number of donor-acceptor interfaces [4]. The exciton dissociation process involves charge transfer of electrons to the acceptor material and of holes to the donor material. However, due to the lack of a continuous network of hole and electron transport materials, the charge transport properties of BHJ OSCs alone tend to be rather poor. The PMHJ overcomes this deficiency by keeping the BHJ layer thin, and by using neat donor and acceptor layers as hole and electron transport layers respectively. The addition of these neat layers allows for improved charge carrier transport to the electrodes to improve the fill factor (FF).

In 2010, a new device architecture was introduced that exploits the n-type Schottky junction formed between thin-film fullerenes and the high work-function electrode of MoO₃-coated ITO [5]. Interestingly, the Schottky junction allows for exceptionally high open-circuit voltage (V_{oc}) on the order of 0.9 – 1.1V [5–7]. In standard OSC architectures, such as with PMHJs, the HOMO_{donor}-LUMO_{acceptor} energy level difference dictates the maximum V_{oc} [8]. However, in Schottky junction cells the V_{oc} is not affected by the HOMO_{donor}-LUMO_{acceptor} difference, but it is instead thought to be determined by the Schottky junction barrier height [9]. Furthermore, it was found that the short circuit current (J_{sc}) and FF of Schottky cells can be improved by doping the fullerene layer with a small amount (5-20%) of suitable donor material. It is interesting to note that the J_{sc} and FF of the donor-doped Schottky cells are comparable to PMHJs in spite of the low donor concentration and the lack of neat charge transport layers. As a

result, Schottky junction solar cells can exhibit very high power conversion efficiencies (PCE) with the highest reported value in literature of 6.4% [10].

There have been several hypotheses to explain the high performance of the Schottky junction architecture, especially with regard to the role of the donor material; however, several critical points merit further investigation [6,7,11]. For instance, varying the donor-acceptor (D-A) mixing ratio in a BHJ has been shown to cause substantial changes in donor morphology, leading to the hypothesis that the increase in J_{sc} is caused by optimized hole transport [10–16]. A detailed background of varying the donor-acceptor ratio has been provided in Chapter 2. Unfortunately, lowering the donor concentration also reduces the absorption by the donor molecules, which are better matched to the solar spectrum than fullerene acceptors, which complicates and casts some doubt on this explanation. More recently it has been suggested that the donor enhances the dissociation of excitons formed in the fullerene matrix, rather than contributing strongly to the absorption of light [15]. However, the exact mechanism behind this dissociation enhancement and subsequent hole transport is not obvious for very low donor concentrations, and has not yet been examined in detail.

In this study, we conduct a systematic investigation of the role of the donor material and the donor-acceptor mixing ratio in Schottky junction solar cells. From the results, we better establish the role of the donor material in the Schottky junction architecture and determine the mechanism by which it affects the photovoltaic performance. We also outline the general principles to optimize the performance of Schottky junction solar cells.

5.2 Materials and methods

Prior to organic layer deposition, the substrates were treated with $CF_4:O_2$ plasma at 20 mTorr pressure and 100W inductively coupled plasma (ICP) power. The flow rates of CF_4 and O_2 were 15 sccm and 5 sccm respectively. After $CF_4:O_2$ plasma treatment, the

rest of the fabrication proceeded as outlined in Section 4.1. The exact device structures used in the experiments are discussed section 5.3. 8nm of bathocuproine (BCP) was deposited before the cathode in all solar cells except for the hole-only devices, where a 20nm layer of N,N'-bis(naphthalen-1-yl)-N,N'-bis(phenyl)-benzidine (NPB) and a 5nm layer of molybdenum oxide (MoO₃) was used instead. 100nm of Al was deposited at 30 Å/s as the top electrode in all devices. A final device area of 0.2 cm² was defined by the intersection of the Al electrode with the patterned ITO. Atomic force microscopy (AFM) samples consisted of a 50nm thick BHJ fabricated on CF₄:O₂ plasma treated ITO.

The following materials were used as donors: Chlorine-Indium Pthalocyanine (ClInPc, Xerox Research Center of Canada, 99.9%, Sublimed-grade); NPB; 4,4'-bis(carbazol-9-yl)biphenyl (CBP), Tris(8-hydroxy-quinolinato)aluminium (Alq3); 4-(dicyanomethylene)-2-tert-butyl-6-(1,1,7,7-tetramethyljulolidin-4-yl-vinyl)-4H-pyran (DCJTb) (Luminescence Technology Corp, >99%, Sublimed-grade).

Photovoltaic parameters, AFM images, UV/Visible absorption spectra and External quantum efficiency spectra were measured as described in Section 4.2.

5.3 Results and Discussion

5.3.1 Influence of the Donor-Acceptor Mixing Ratio

In order to study the effect of varying the donor-acceptor mixing ratio in the Schottky junction architecture, we fabricated simple Schottky devices with the structure: ITO/Donor:C₆₀/BCP/Al, as illustrated in **Figure 11**. The ITO was treated with CF₄:O₂ plasma to increase its work function, which is shown here to provide an electrode capable of forming a Schottky junction with C₆₀ (analogous to the more common ITO/MoO₃ interface). The effects of ITO treatment by CF₄:O₂ have been discussed elsewhere [17] and ITO/CF₄ has just recently been used for OSC applications [18,19]. ClInPc, as a relatively new and highly efficient material [20–22] was used as the donor in 10% and 50% concentration mixtures with C₆₀. BCP was used as an exciton blocking layer and

was then followed by the Al cathode. The photovoltaic output parameters for these cells tested under 1-sun AM1.5G irradiation are shown in Table 2.

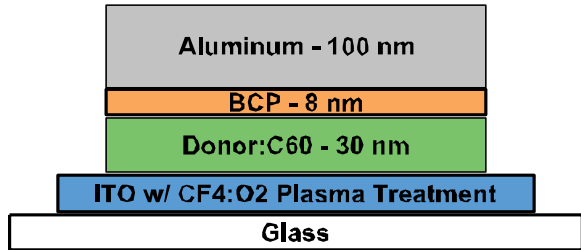


Figure 11: Schematic of the Schottky junction device structure used to investigate the effect of the mixing ratio. Reproduced with permission.

As expected, solar cells formed with a neat C_{60} layer display a high V_{oc} due to the n-type Schottky junction. Doping the C_{60} Schottky cell with 10% ClInPc increases the J_{sc} and FF dramatically, while the V_{oc} suffers a minor decrease. Increasing the ClInPc concentration to 50% lowers the J_{sc} and V_{oc} , but increases the FF.

Table 2: Photovoltaic performance of ClInPc: C_{60} Schottky junction devices with different doping concentrations. Reproduced with permission

Doping Concentration	J_{sc} [mA cm^{-2}]	V_{oc} [V]	FF [%]	PCE [%]
0% (Neat C_{60})	1.15	1.16	32	0.42
10%	4.99	0.99	41	2.02
50%	4.32	0.80	45	1.57

To understand the changes in J_{sc} caused by the variation in donor concentration, we measured the external quantum efficiency (EQE) of these cells. The EQE spectra of these cells from $\lambda = 300\text{nm}$ to 900nm are shown in Figure 12(a). The EQE spectrum of the neat C_{60} cells reaches a maximum efficiency of 15% at $\lambda = 350\text{nm}$ with a shoulder at $\lambda = 470\text{nm}$ and gradually drops off to negligible levels at $\lambda > 530\text{nm}$. With the

introduction of 10% ClInPc donor, we observe its contribution at $\lambda = 720\text{nm}$ with $\sim 6.5\%$ quantum efficiency. In addition, two interesting effects are observed: First, the quantum efficiency at $\lambda = 350\text{nm}$ increases from approximately 15% to 35%. Secondly, the EQE shoulder observed in the neat C_{60} cells at $\lambda = 470\text{nm}$ is enhanced and appears as distinct peak with approximately 25% quantum efficiency. This band at $\lambda = 470\text{nm}$ is relatively broad, starting at 400nm and gradually dropping off to zero at $\lambda > 600\text{nm}$. When the ClInPc concentration is further increased to 50%, the EQE of the 350nm band surprisingly remains the same even though the concentration of C_{60} is substantially reduced. In contrast, the 470nm band is strongly suppressed. Finally, as expected, the peak at $\lambda = 720\text{nm}$ increases to 22%.

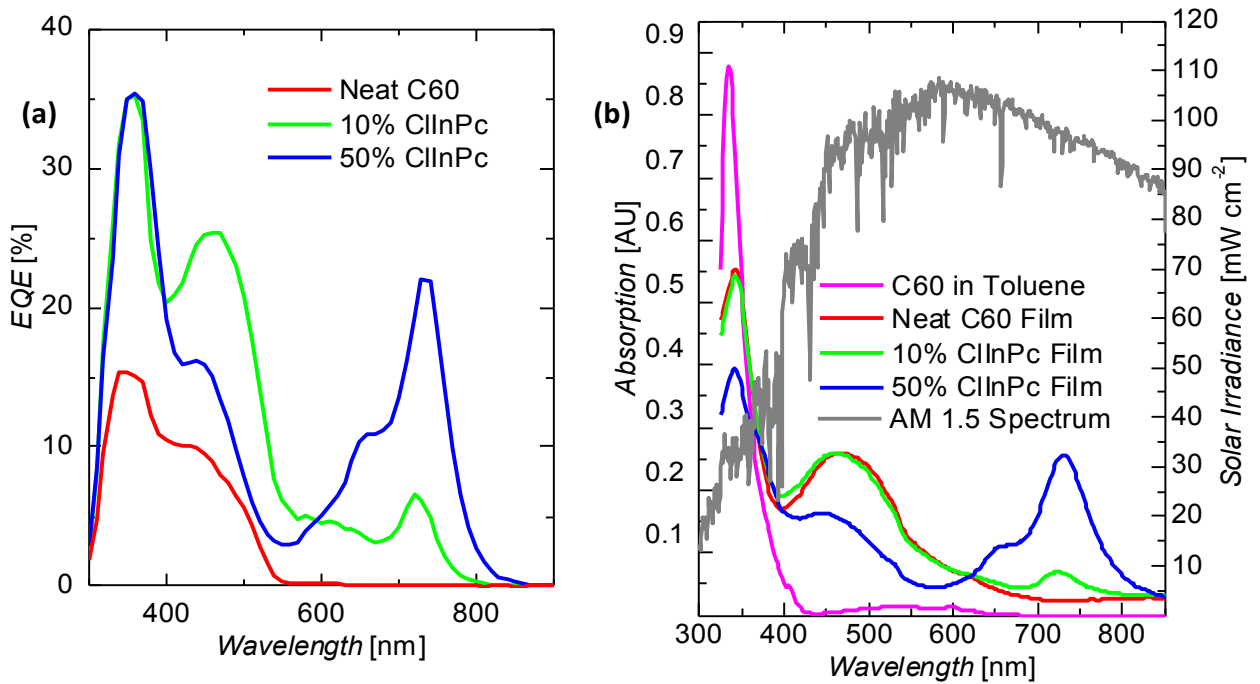


Figure 12 a) EQE spectra of Schottky junction devices with varying donor concentration, and b) UV/Vis absorption spectra of Schottky junction devices. Also shown: UV/Vis absorption spectrum of C_{60} in toluene and the AM1.5 spectrum

In order to better understand the trends in the EQE spectra, UV/Vis absorption spectra of the cells were measured and are plotted in Figure 12(b). The absorption spectrum of neat C_{60} cells shows two features: a narrow band that extends from $\lambda = 330\text{nm}$ to 400nm (peak at 350nm) and a relatively broad band that extends from $\lambda = 400\text{nm}$ to $\lambda > 600\text{nm}$ (peak at 470nm). Interestingly, the EQE measurements for neat C_{60}

cells show that photocurrent is generated only due to the absorption by the 350nm band and not due to the absorption by the 470nm band. At 10% ClInPc concentration, the absorption of C₆₀ at $\lambda = 350\text{nm}$ and $\lambda = 470\text{nm}$ are relatively unchanged, and a new peak corresponding to the ClInPc absorption is observed at $\lambda = 720\text{nm}$. However, considering the EQE measurements for this case, photocurrent is generated from both the 350nm and 470nm bands. It is thus clear that the addition of the small amount of donor material is necessary for photocurrent to be harvested from this 470nm band. Furthermore, in contrast to previous reports in literature, the absorption by the donor material contributes to the generation of photocurrent in spite of its rather low concentration [7].

When the ClInPc concentration is increased to 50%, the absorption by C₆₀ at the 350nm and 470nm bands is suppressed and the absorption due to the ClInPc at the 720nm band increases. From the EQE spectra in Figure 12(a), it can be seen that the photocurrent contribution from the ClInPc at 720nm increases proportionally to the donor concentration and donor absorption. Quite interestingly, the EQE at $\lambda = 350\text{nm}$ is similar for both the 10% ClInPc and 50% ClInPc cells even though the C₆₀ absorption is significantly lower for the 50% ClInPc cell. In contrast, the EQE at $\lambda = 470\text{nm}$ is substantially reduced in the 50% ClInPc cells, which follows as a consequence of the reduced absorption at 470nm. An analysis of the normalized absorption spectra of the cells shows that the suppression of the 470nm C₆₀ absorption band in 50% ClInPc cells cannot be completely explained by the reduction in C₆₀ concentration and suggests that this absorption band might be associated with C₆₀ aggregation.

To further probe the mechanism behind the suppression of the 470nm C₆₀ absorption band in the 50% ClInPc cells, the UV/Vis absorption spectrum of C₆₀ in toluene solution was compared with its absorption in thin films, also shown in Figure 12(b). It can be seen that the absorption of C₆₀ in toluene only displays a peak at $\lambda = 350\text{nm}$ and does not show significant absorption at $\lambda = 470\text{nm}$. It has been established that the first allowed intramolecular transition in C₆₀ falls at 3.53 eV ($\lambda \sim 351\text{nm}$) which explains the presence of this absorption peak for C₆₀ in toluene [23]. It has also been shown that absorption in the range of 2.3 – 3.75 eV ($\lambda \sim 539\text{nm} - 330\text{nm}$) is due to

intermolecular charge transfer (CT) states [23]. Therefore, it is reasonable to conclude that the C_{60} absorption band at 470nm is due to the intermolecular CT states in C_{60} aggregates formed in thin films. The suppression of the 470nm absorption band of C_{60} in 50% ClInPc devices is therefore due to the prevention of C_{60} aggregate formation in the presence of a significant amount of ClInPc molecules.

Since the UV/Vis absorption results suggest aggregation of C_{60} at low (or no) donor concentrations, we can expect the film morphology to reflect these differences – i.e. the morphology of the films with no donor or low donor concentration might be different than the morphology of the films with high donor concentration. In order to investigate these morphological differences, we studied the surface morphology of C_{60} films with 0%, 10%, 20% and 50% ClInPc donor concentration using atomic force microscopy (AFM). AFM scans of these films on CF_4 -treated ITO are shown in Figure 13. The surface of pure C_{60} has many nodules, indicative of C_{60} aggregate formation, and exhibits a root-mean-square (RMS) surface roughness of 3.3nm. At 10% ClInPc concentration the density of nodules appears to be similar to pure C_{60} , but the RMS surface roughness decreases slightly to 3.0nm. At 20% ClInPc concentration the density of nodules is greatly reduced, suggesting a reduction in the formation of C_{60} aggregates. By 50% ClInPc concentration the density of nodules is significantly diminished and the film is much smoother with an RMS surface roughness of 2.5nm, indicating that the formation of C_{60} aggregates has been suppressed. The remarkable similarity between the morphology of 0% and 10% ClInPc concentration films, in contrast to that of 50% ClInPc concentration films, clearly mirrors the findings from the UV/Vis absorption spectra – the aggregation of C_{60} is significant in both the neat and the 10% ClInPc films.

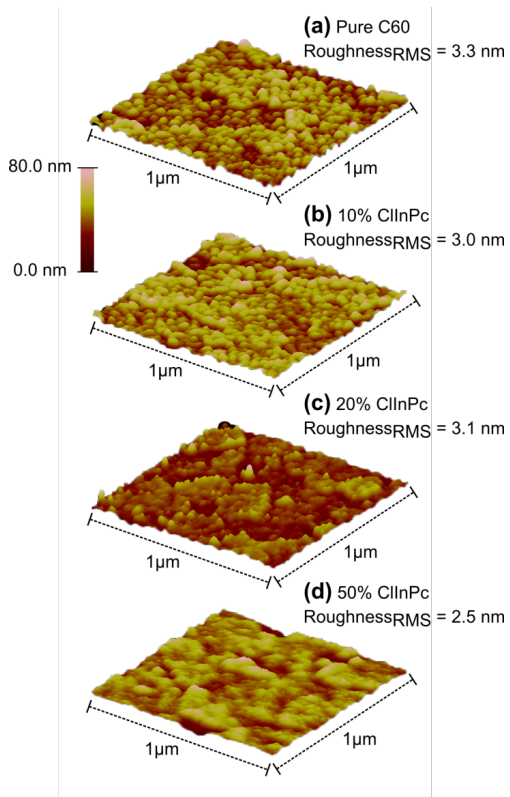


Figure 13: AFM images of 50nm films of a) pure C_{60} , b) 10% ClInPc in C_{60} , c) 20% ClInPc in C_{60} and d) 50% ClInPc in C_{60} on $CF_4:O_2$ plasma treated ITO. Reproduced with permission.

From the overlaid AM1.5 spectrum in Figure 12(b), it can be seen that the C_{60} aggregate absorption band is well matched to the solar spectrum, receiving a solar irradiance of 97.7mW cm^{-2} at $\lambda = 472\text{nm}$. The ClInPc absorption band receives a similar solar irradiance of 97.1mW cm^{-2} at $\lambda = 720\text{nm}$. The 350nm absorption band of C_{60} is, however, poorly matched to the solar spectrum receiving an irradiance of only 35.4mW cm^{-2} at $\lambda = 350\text{nm}$. The contribution to the photocurrent due to the C_{60} aggregate absorption ($\sim 25\%$ EQE at $\lambda = 470\text{nm}$ in 10% ClInPc cells) roughly matches that due to ClInPc donor absorption ($\sim 22\%$ EQE at $\lambda = 720\text{nm}$ in 50% ClInPc cells). Considering that the EQE at 350nm is similar for both 10% and 50% ClInPc cells, the J_{sc} is higher for 10% ClInPc cells due to the higher C_{60} aggregate contribution and due to the presence of the small donor contribution ($\sim 6.5\%$ EQE at $\lambda = 720\text{nm}$ in 10% ClInPc cells). When combined with the enhancement in the V_{oc} due to the formation of the n-type Schottky junction at the ITO/ C_{60} interface for the 10% ClInPc cells, the power conversion

efficiency (PCE) of the 10% ClInPc cells is obviously greater than that of the 50% ClInPc cells.

The EQE, UV/Vis and AFM data convincingly demonstrate that the increase in J_{sc} seen in Schottky OSCs at lower donor concentrations arises primarily from photocurrent produced by absorption due to CT intermolecular states in C_{60} aggregates. These aggregates form at high C_{60} concentrations and absorb in the 400-600nm range, allowing for a good match to the solar spectrum. The presence of the donor molecules is necessary for the efficient extraction of photocurrent from the C_{60} aggregate absorption band. Increasing the donor concentration beyond a certain threshold, however, hinders C_{60} aggregate formation and thus removes its contribution to the photocurrent completely. Therefore, varying the donor-acceptor mixing ratio strongly influences the photocurrent.

5.3.2 Influence of the Choice of Donor Material

In a Schottky junction OSC, the donor material has been suggested to allow for better hole transport and collection through the percolation mechanism. It has also been suggested to contribute to exciton dissociation due to the energy level difference at the donor-acceptor interface [6,10,11]. Presumably, a combination of the two mechanisms is responsible for allowing photocurrent to be harvested, especially from C_{60} aggregate absorption.

We first studied the donor's role in assisting with exciton dissociation by using devices with the structure: ITO/Donor: C_{60} / C_{60} /BCP/Al, as illustrated in Figure 14(a). Donors with different HOMO and LUMO offsets were mixed with C_{60} at 10% concentration in a 10nm layer adjacent to the plasma treated ITO interface. The relative positions of the energy levels of the donors, C_{60} and the ITO/CF₄ anode (obtained from literature) are also illustrated in Figure 14(a) [24–29]. Due to the high concentration of C_{60} in these cells, it is expected that the majority of the excitons will form on C_{60} molecules. Holes from the C_{60} will be transferred to the HOMO level of the donor material provided that the HOMO_{donor}-HOMO _{C_{60}} offset is large enough to make the

transfer energetically favorable. The photovoltaic performance and the EQE spectra of these devices were measured. Table 3 shows the photovoltaic performance of these devices tested under 1-sun AM1.5G irradiation and the EQE spectra of these devices are shown in Figure 14(b).

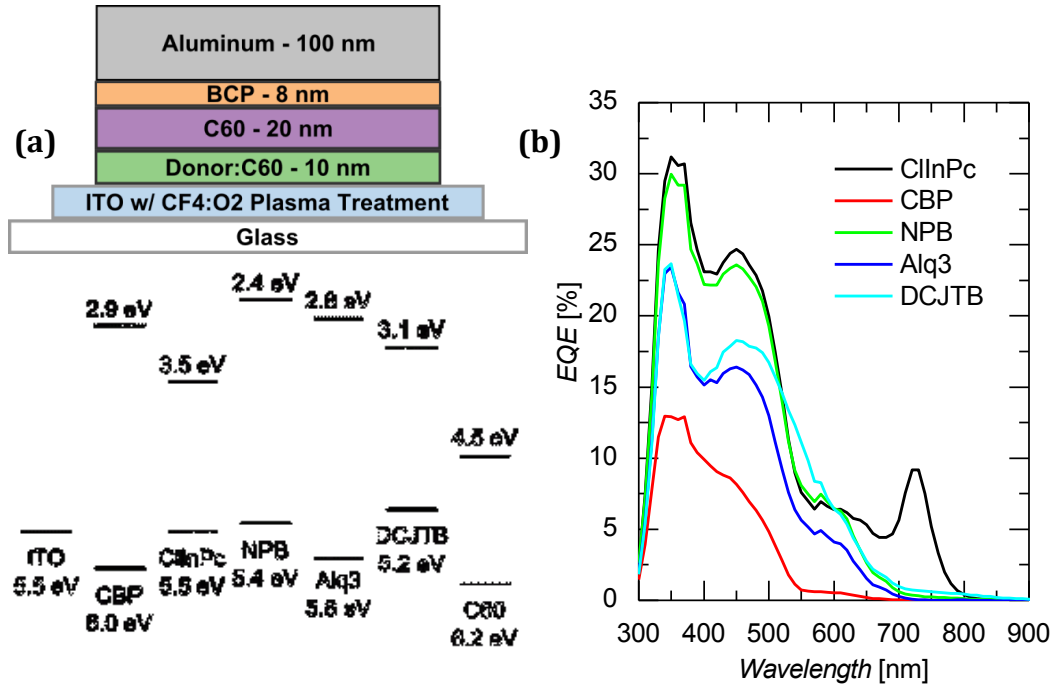


Figure 14: a) Schematic of the Schottky junction device structure used to test the effect of varying the donor material at 10% donor concentration with associated energy levels shown below and b) EQE spectra of devices shown in (a). Reproduced with permission.

From Figure 14(a) and Table 3, it can be seen that, when the $\text{HOMO}_{\text{donor}} - \text{HOMO}_{\text{C60}}$ difference is too low, approximately 0.2 eV in the case with CBP, the J_{sc} is very low. From Figure 14(b), it is evident that EQE spectrum of the CBP:C60 device closely resembles that of the neat C60 device. The presence of the CBP donor does not significantly change the J_{sc} or FF when compared to the neat C60 device, and it can be seen that very little photocurrent is harvested from the C60 aggregate absorption band at 470nm. Furthermore, the V_{oc} is similar to that of the pure C60 cell, indicating that the reduced concentration of C60 at the ITO interface has no significant impact on the formation of the Schottky junction. In contrast, Alq3 has a $\text{HOMO}_{\text{donor}} - \text{HOMO}_{\text{C60}}$ difference of approximately 0.4 eV, which allows for the extraction of photocurrent from

the C₆₀ aggregate absorption band as seen by its EQE of 16% at $\lambda = 470\text{nm}$. Using ClInPc and NPB as a donor increases the HOMO_{donor}-HOMO_{C₆₀} difference to approximately 0.6 eV and 0.7 eV respectively, which increases the J_{sc} even further. The EQE at $\lambda = 470\text{nm}$ for both of these cells are similar (~25%), and the only difference in the EQE spectra between these cells appears to be the ClInPc absorption at $\lambda = 720\text{nm}$. If the HOMO_{donor}-HOMO_{C₆₀} difference is further increased, for example to ~1.0 eV with DCJTb, the EQE due to C₆₀ aggregate absorption at $\lambda = 470\text{nm}$ actually decreases to 18%; however, these devices show stronger tail-end absorption compared to the other devices, with higher EQE in the range of $\lambda = 510 - 590\text{nm}$. Overall, the J_{sc} values for the DCJTb devices are comparable to the Alq₃ devices.

Table 3: Photovoltaic performance of Schottky junction devices with different donor materials at 10% donor concentration. The schematic of the device structure is shown in Figure 4(a). Reproduced with permission.

Donor Material	J _{sc} [mA cm ⁻²]	V _{oc} [V]	FF	PCE [%]
ClInPc	4.20	1.00	50	2.07
NPB	3.80	0.82	49	1.51
DCJTb	2.90	0.61	34	0.61
Alq ₃	2.44	0.73	34	0.61
CBP	1.10	1.19	31	0.41

An analysis of the normalized UV/Vis absorption spectra of these devices revealed that, with the exception of a minor ClInPc absorption peak at $\lambda = 720\text{nm}$, all other devices had absorption spectra similar to that of pure C₆₀.

In order to investigate whether varying the donor material affects the transport and collection of holes across the ITO interface, we first constructed hole-only devices on CF₄-treated ITO with the structure: ITO/Donor:C₆₀/C₆₀/NPB/MoO₃/Al, as shown in

Figure 15(a). For these hole-only devices, the donor-doped C₆₀ layer was 10nm thick and the donor material concentration was fixed at 10%. The doped layer was followed by 10nm of neat C₆₀ in order to resemble the devices in Figure 14(a). 20nm of NPB electron blocking layer was used to ensure hole-only transport through the device and to protect the active organic films from damage during top electrode deposition. Furthermore, 5nm of MoO₃ was used to prevent electron injection and to facilitate hole injection from the top Al electrode. Current-voltage (I-V) measurements were obtained in the dark by applying a negative bias to the ITO electrode. When a negative bias is applied to the ITO electrode, holes are injected from the top Al electrode and traverse through the device to be collected at the ITO electrode. As such, the direction of the hole current in these hole-only devices resembles that of photo-generated holes in the corresponding solar cells.

Figure 15(b) shows the I-V characteristic of these devices when the ITO is under negative bias.

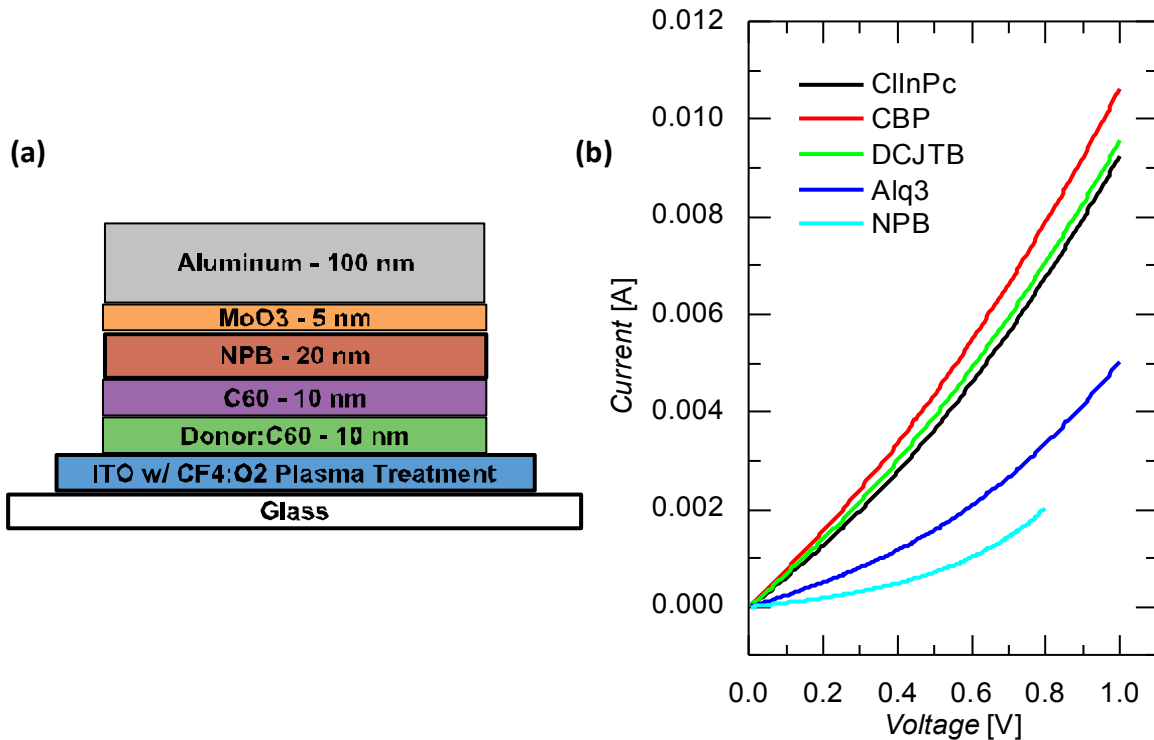


Figure 15: a) Schematic of the hole-only device structure used to study the hole extraction properties of different donor materials and b) IV characteristics of the devices in (a) with different donors

Hole-only devices with DCJTb, CBP and ClInPc donors all show similar hole conduction properties whereas hole-only devices with Alq₃ and NPB donors show markedly reduced hole conduction. Interestingly, the I-V trends of the hole-only devices do not mirror the photovoltaic characteristics of the corresponding solar cells with the same donor materials. For example, even though NPB:C₆₀ devices have the lowest observable current in hole-only devices, the corresponding NPB:C₆₀ solar cells have comparable J_{sc} to the ClInPc:C₆₀ solar cells. As was established previously from our EQE data, the difference in J_{sc} between ClInPc:C₆₀ and NPB:C₆₀ solar cells is solely due to the ClInPc absorption. Similarly, DCJTb:C₆₀ and Alq₃:C₆₀ solar cells demonstrate comparable J_{sc} even though the DCJTb:C₆₀ hole-only devices have a higher hole conductivity than Alq₃:C₆₀ hole-only devices. Therefore, it is reasonable to conclude that the hole conduction properties of the specific donor do not significantly influence the photovoltaic performance of Schottky junction cells.

At this point, it should be noted that the HOMO energy levels quoted in the preceding analysis are based on UPS/XPS data obtained using single layer or bi-layer thin films in other published works. In donor-acceptor mixed layers, however, it has been reported that varying the donor-acceptor mixing ratio can influence the HOMO level of the donor due to changes in the polarization energy caused by variations in the local environment [30]. As a result, it is difficult to determine the optimum HOMO offset with C₆₀ that allows for the greatest dissociation of the aggregate absorption excitons based on literature values alone.

In Table 3, it can be seen that the V_{oc} of the Schottky cells is affected by the choice of the donor material and is not fixed by Schottky junction barrier height as previously reported [6,7] which provides evidence of charge trapping by the donor material. It is feasible that the photovoltaic performance of the solar cells do not correlate with the hole conduction in hole-only devices because the built-in electric field in the solar cells is sufficient to free the trapped charges from the donor material at the tested doped layer thickness of 10nm.

The trapping effect of the donor material could become more evident if the doped layer thickness is increased. The devices shown in **Figure 11** contain a 30nm doped layer whereas the devices in Figure 14(a) contain a 10nm doped layer followed by 20nm of neat C₆₀. Comparing the PV performance of the devices with a 30nm doped layer (Table 2) and 10nm doped layer (Table 3), there is a clear trade-off between the J_{sc} and FF as a function of the doped layer thickness. A thicker doped layer results in higher J_{sc} due to greater dissociation of the excitons formed by C₆₀ aggregate absorption. However, a thicker doped layer also reduces the FF due to increased charge trapping by the donor molecules far away from the ITO interface. If exciton dissociation happens far away from the ITO interface, the dissociated holes have to travel a larger distance in order to be collected and, therefore, have a higher chance of being trapped by the donor molecule. Hence, the probability of recombination is increased. Therefore, Schottky junction devices need to have an optimal doped layer thickness in order to maximize the dissociation of C₆₀ aggregate excitons while minimizing trapping and recombination on the donor molecules.

Following this line of reasoning, we optimized C₇₀:ClInPc devices by keeping the total thickness of the active layer constant at 30nm and varying the thickness of the doped layer. Similar aggregate absorption properties seen with C₆₀ (as discussed above) are expected to apply to C₇₀. These devices thus employed the structure: CF₄-Treated ITO/ClInPc:C₇₀ (x nm)/C₇₀ (30 - x nm)/BCP/Al. The photovoltaic output parameters of these devices are shown in

Table 4. Devices with 17.5 nm doped layer thickness demonstrated the highest achieved PCE of 3.6% with a J_{sc} of 8.4 mA cm^{-2} , a FF of 40% and a V_{oc} of 1.1V. Beyond this doped layer thickness, the donor molecules do not contribute positively to increasing the efficiency because trapping and recombination on the donor sites greatly reduce the FF without proportionally increasing the J_{sc} .

Table 4: Photovoltaic performance of ClInPc:C₇₀ devices for different doped layer thicknesses. The device structure is CF₄-Treated ITO/ClInPc:C₇₀ (x nm)/C₇₀ (30 – x nm)/BCP/Al. Reproduced with permission.

Doper Layer Thickness (x) [nm]	Jsc [mA cm ⁻²]	Voc [V]	FF	PCE [%]
0	1.39	1.25	34	0.58
10	6.37	1.04	51	3.38
12.5	7.76	1.07	43	3.60
17.5	8.43	1.07	40	3.62
30	8.85	1.06	38	3.58

Considering the results of these experiments together, it is evident that the role of the donor material is primarily as an exciton dissociation agent, and that charge extraction is most efficient when the doped layer is kept thin due to charge trapping by the donor molecules. The majority of excitons are formed by C₆₀ due to its absorption by the 350nm and 470nm bands. As mentioned previously, the excitons formed due to the 350nm absorption band are intramolecular Frenkel excitons, whereas the excitons formed due to the 470nm absorption band are intermolecular CT excitons on C₆₀ aggregates. In neat C₆₀ devices, most of the photocurrent is due to the dissociation of the 350nm band Frenkel excitons by the built-in electric field. It is suggested that the 470nm band CT excitons are not dissociated in neat C₆₀ devices because, being sub-bandgap excitons, they have higher binding energies. In the presence of CBP, the sub-bandgap excitons formed due to C₆₀ aggregate absorption are not dissociated due to an insufficient HOMO offset with C₆₀. At low Alq₃, NPB, DCJTb and ClInPc concentrations, the sub-bandgap excitons formed due to C₆₀ aggregate absorption contribute to the photocurrent since dissociation (due to the larger HOMO_{donor}-HOMO_{C60} offset) becomes efficient. The high photocurrent seen in the NPB and ClInPc donor cells may be due to the optimal alignment of the HOMO energy levels with C₆₀ which maximizes the efficiency of dissociation while keeping charge

trapping and recombination to a minimum. The lower photocurrent in the Alq₃ devices can be attributed to its reduced HOMO offset with C₆₀ which reduces its capacity to dissociate the aggregate absorption excitons. The higher EQE seen at longer wavelengths with DCJTB donor is due to the larger HOMO energy level difference between C₆₀ and DCJTB. Longer wavelength absorption by C₆₀, in the range of $\lambda = 540\text{nm} - 730\text{nm}$, has been reported to form sub-bandgap intramolecular Frenkel excitons that have a higher binding energy than the 470nm band CT excitons [23]. The higher HOMO energy level difference between C₆₀ and DCJTB allows for the dissociation of these high binding energy Frenkel excitons leading to enhanced photocurrent at longer wavelengths. However, the high HOMO offset could also contribute to deeper charge trapping, which results in overall lower J_{sc} for the DCJTB devices.

5.4 Conclusions

We have found that the increase in J_{sc} seen in Schottky OSCs at low donor concentrations arises primarily from photocurrent produced by CT intermolecular states in C₆₀ aggregates, which form at high C₆₀ concentrations. These aggregates absorb in the 400-600nm range and thus are well matched to the solar spectrum. The presence of a donor is found to be necessary for the dissociation of these C₆₀ aggregate excitons. The exciton dissociation process is governed primarily by the HOMO_{donor}-HOMO_{C60} difference, and is only efficient when the difference is large enough for energetically favorable transfer of holes from C₆₀ to the donor. Increasing the donor concentration beyond a certain threshold, however, hinders C₆₀ aggregate formation and thus removes its contribution to the photocurrent completely. As a consequence, varying the donor-acceptor mixing ratio strongly influences the photocurrent.

Furthermore, the V_{oc} of the Schottky cell is affected by the choice of donor material and is not set by the Schottky junction barrier height as previously thought, which implies charge trapping by the donor. However, for thin donor-doped layers, the photovoltaic properties of the Schottky cells are independent of the doped layers' hole transport and collection properties, suggesting that the specific donor's hole conductivity

does not play a major role in its collection of holes (i.e. the donor acts primarily as an exciton dissociation agent). As the donor-doped layer thickness increases, trapping and recombination at the donor sites far away from the ITO interface becomes significant, resulting in reduced FF. By optimizing the doped layer thickness, the dissociation of aggregate excitons can be maximized and recombination kept to a minimum.

These results not only uncover and help explain key aspects about the operation mechanism of the emerging and highly promising Schottky junction organic solar cells, but also shed light on the phenomenon of aggregation and associated photovoltaic performance in fullerenes, one of the most widely used acceptor materials in the field. We therefore expect these results to be useful for stimulating and guiding future research efforts in organic solar cells. For example, the enhanced absorption of fullerene aggregates can now be utilized to complement donor material absorption through the judicious design of donor:fullerene bulk-heterojunctions in PMHJ and tandem cell architectures, potentially vastly improving the solar spectral match of organic solar cells.

Chapter 6 – Interplay Between Efficiency and Device Architecture for Small Molecule Organic Solar Cells

Authors: Graeme Williams, Sibi Suttu and Hany Aziz

Published in: *Physical Chemistry Chemical Physics*, vol. 16, iss. 23, pp – 11398-408, 2014. Reproduced with permission from the PCCP Owner Societies.

Chapter Summary

It was shown in Chapter 5 that the donor-acceptor mixing ratio is a crucial parameter in controlling the morphology of the BHJ active layer and influencing the efficiency of BHJ OSCs. In this chapter, the effect of controlling the donor-acceptor mixing ratio, and by extension, the mixing layer morphology, is investigated across the full spectrum of possible OSC device architectures. This chapter addresses the second objective mentioned in Chapter 3. We investigate five different organic solar cell (OSC) structures, including the simple planar heterojunction (PHJ) and bulk heterojunction (BHJ), as well as several planar-mixed structures. Chlorogallium phthalocyanine (ClGaPc) and C₆₀-fullerene are employed as donor and acceptor in this systematic study on OSC device architecture. The different OSC structures are studied over a wide range of ClGaPc:C₆₀ mixing concentrations to gain a comprehensive understanding of their charge transport behavior. Transient photocurrent decay measurements provide crucial information regarding the interplay between charge sweep-out and charge recombination, and ultimately hint toward space charge effects in planar-mixed structures. Results show that the BHJ/acceptor architecture, comprising a BHJ layer with high C₆₀ content, generates OSCs with the highest performance by balancing charge generation with charge collection. The performance of other device architectures is largely limited by hole transport, with associated hole accumulation and space charge effects.

6.1 Introduction

In this work, we examine OSCs of varying device architectures that employ a chlorogallium phthalocyanine (ClGaPc) donor and a fullerene (C_{60}) acceptor while maintaining a constant device thickness. Specifically, we study device architectures including the planar heterojunction (PHJ), the bulk heterojunction (BHJ), a BHJ/acceptor active layer, a donor/BHJ active layer, and the full PM-HJ. The full PM-HJ employs both neat donor and acceptor layers bordering the BHJ. Within this subset of device architectures, we vary the C_{60} content within the active layer from 25% to 87.5%. As mentioned in Chapter 5, high C_{60} concentrations allows for exciton formation and dissociation in C_{60} aggregates leading to high photocurrents. When the donor-acceptor ratio is 1:1 (or 50% C_{60} concentration) the aggregation of C_{60} is inhibited leading to less photocurrent produced from C_{60} aggregates and more photocurrent produced from the donor material [1-4]. By varying the donor-acceptor ratio, the effect of the BHJ morphology on the device physics of the various architectures can be studied.

The different devices are tested for their photovoltaic output parameters, their external quantum efficiency (EQE) spectra and their transient photoresponse to provide a complete picture of their operation and the inherent limitations in their device architectures. The use of transient photocurrent behavior in OSCs in particular is highlighted as a powerful technique to better understand charge transport as well as charge trapping effects, as has been shown in literature [5-8]. It is coupled with the varied device architectures in the present work to help distinguish between charge sweep-out and charge recombination, and to better understand the role of space charge effects in limiting performance of specific device structures.

We have observed that improvement in performance with device architecture is strongly associated with minimizing charge trapping and associated charge recombination effects. To this end, the PM-HJ device architecture is shown to reduce charge recombination effects compared to an equivalent thickness BHJ; however, the poor mobility of the neat donor layer results in space charge effects that ultimately

degrade device performance. The results thus lend credence to the heavily doped organic layers employed in the p-i-n OSCs, such as those used by Riede and coworkers [9]. Schottky OSCs are shown to offer a fast transient response to prevent space charge effects, but are ultimately limited by the poor charge transport properties and associated charge recombination within the thick mixed donor-acceptor layer. It follows that for the ClGaPc:C₆₀ materials system, due to the limited donor hole mobility and the absence of doped organic layers, the highest performing OSCs employ a Schottky architecture with a neat C₆₀ acceptor layer, optimizing the tradeoff between charge generation and charge collection. From a broader viewpoint, we show that optimal device architecture must be determined specifically based on the physical properties of the chosen donor and acceptor materials. Furthermore, the comprehensive set of devices and the associated characterization techniques employed in this work allow for judicious determination of the device architecture required to achieve high efficiency OSCs with optimal charge collection characteristics.

6.2 Experimental

The devices used in this study were fabricated according to the general procedure laid out in Section 4.1. 5 nm of MoO₃ (Sigma Aldrich) was deposited by thermal evaporation ($<5 \times 10^{-6}$ torr base pressure) at a rate of 2 Å/s. The mixed layers were fabricated by the simultaneous co-deposition of C₆₀ (>99.9%, M.E.R. Corporation) and the ClGaPc donor material. Different mixing ratios were achieved by varying the deposition rates of ClGaPc and C₆₀, and the sum total deposition rate of all materials was kept at 2 Å/s. ClGaPc was obtained from the Xerox Research Centre of Canada, where it was also purified by train sublimation. BCP was obtained from Luminescence Technology Corp (>99%, sublimed-grade). 8 nm of BCP was then deposited by thermal evaporation at 2 Å/s prior to the cathode. To finish the OSCs, 100 nm of Al was deposited by thermal evaporation at 3 Å/s. A final device area of 0.2 cm² was defined by the intersection of the Al electrode with the patterned ITO.

Photovoltaic output parameters, UV/Visible absorption spectra, external quantum efficiency spectra were obtained as described in Section 4.2. To remove the ClGaPc EQE contributions to photocurrent (Figure 20) the UV/Vis absorption data was used to first identify the ClGaPc curve shape, which was normalized to the EQE values using the peak (750 nm) intensity. The curve was then subtracted directly from the EQE plot. Transient photocurrent measurements were performed with white or colored LEDs, a Stanford Research Systems DG535 pulse generator (pulsed for 5ms at 100Hz) and a Tektronix TDS5054 oscilloscope. To extract data in the relevant bias point and timeframe for our devices, a 1 kOhm resistor was placed in series with the DUT during illumination, and the voltage was measured over the resistor with the oscilloscope. A custom MATLAB program was used to extract the transient photocurrent decay (falling) data and to calculate single/bi-exponential fits.

6.3 Results and Discussion

ClGaPc is a relatively new donor material in the realm of OSCs, with only a few uses in literature [10, 11]. However, it is shown here to provide reasonable efficiencies (upwards of 2.9% power conversion efficiency (PCE)) when mixed with C₆₀. Its behavior as a donor, with regard to both processing and inherent physical properties, is found to be similar to that of chloroindium phthalocyanine (ClInPc), a donor that is somewhat more studied in literature [3, 4, 12], with strong absorption in the red/near-IR (peak at 750 nm, shoulder at 664 nm). The energy level diagram for the various species employed in the OSCs in this work as well as the absorbance spectra for both ClGaPc and C₆₀ are provided in Figure 16. The highest occupied molecular orbital (HOMO) and lowest unoccupied molecular orbital (LUMO) values for ClGaPc have been estimated from the optical bandgap of the neat film, combined with a HOMO estimate from the V_{oc} of a ClGaPc/C₆₀ PHJ device.

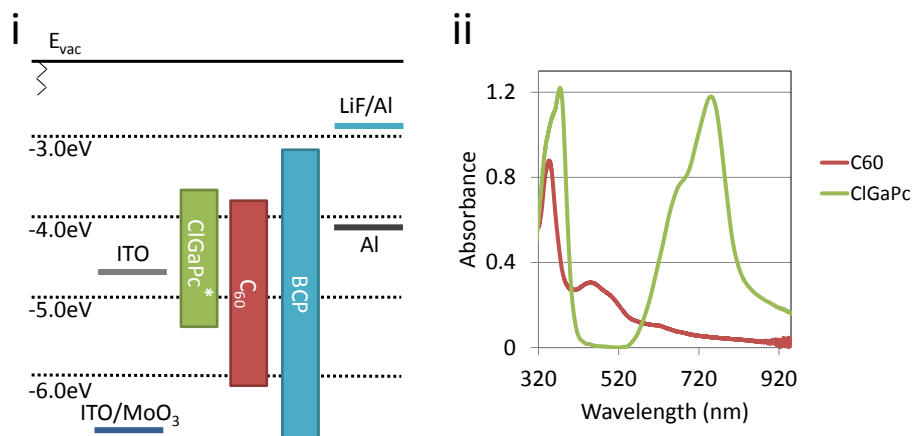


Figure 16: i. Energy level diagram for ClGaPc/C₆₀ organic solar cells. ii. Absorbance spectra of 50 nm films of C₆₀ and ClGaPc. Reproduced with permission from the PCCP Owner Societies.

In the present study, ClGaPc and C₆₀ are incorporated into various device architectures, as detailed in Figure 17 while maintaining a total device thickness of 40nm. The device thickness is specifically chosen to provide reasonable efficiencies – thicker devices generally suffer from poor FFs, while thinner devices suffer from poor short circuit current densities (J_{sc}). In all devices, a 5-nm MoO₃ hole extraction layer (HEL) and an 8-nm BCP electron extraction layer (EEL) are used. The devices are labelled ‘A’ through ‘E’, corresponding to the PHJ, BHJ, BHJ/acceptor, donor/BHJ and full PM-HJ device architectures respectively. Note that with current nomenclature the BHJ/acceptor and donor/BHJ OSCs are technically considered PM-HJ devices; however, for simplicity, we refer to the PM-HJ as the full PM-HJ OSC that includes both neat donor and acceptor layers. In the case of the PHJ, the thicknesses of the layers are varied in order to vary the donor-to-acceptor content. In devices B through E, the donor-to-acceptor ratio within the mixed layer (BHJ) is varied. As will be discussed in greater detail below, for the cases where high C₆₀ content is used and the mixed BHJ layer is in direct contact with the ITO/MoO₃ anode, a Schottky contact is formed. In effect the structures presented in Figure 17 represent the full spread of viable device architectures with the constituent materials, and thus can provide a full picture of charge transport considerations as they relate to OSC efficiency.

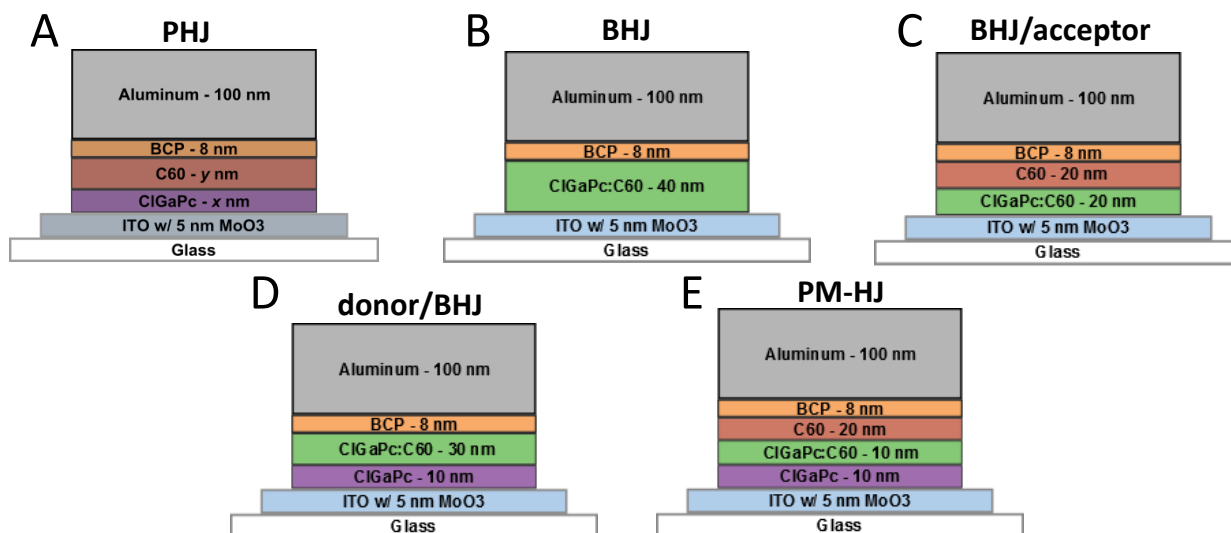


Figure 17 - Illustration of OSC Device Architectures, including: a) planar heterojunction (PHJ), b) bulk heterojunction (BHJ). c) BHJ with a neat acceptor layer, d) BHJ with a neat donor layer and e) planar-mixed molecular heterojunction. Reproduced with permission from the PCCP Owner Societies

The photovoltaic output parameters for devices A through E as a function of C_{60} content are provided in Figure 18. From the first panel in Figure 18, it is clear that the BHJ and BHJ/acceptor device architectures (structures B and C respectively) offer the highest efficiencies – the latter allowing for 2.9% PCE at a 1:7 ClGaPc: C_{60} mixing ratio. The worst performing devices are those that employ a donor/BHJ device architecture (structure D), with PCE values less than half of that of structure C for the same mixing ratios. The PM-HJ device architecture (structure E) grants slightly improved efficiencies compared to that of equivalent PHJ devices (structure A). Interestingly, the PM-HJ drops in efficiency at higher C_{60} content, and so it cannot compete with devices B and C for the 1:3, 1:5 and 1:7 ClGaPc: C_{60} mixing ratios. In general, all devices show improvement in PCE with more C_{60} content than ClGaPc donor content. To better understand these trends in efficiency with changes in device architecture, it is necessary to examine the photovoltaic output parameters (J_{sc} , FF and V_{oc}) in greater depth and in combination with EQE measurements as well as transient photoresponse measurements. To accomplish this task in a meaningful manner, we will compare the device architectures incrementally in terms of their structural complexity.

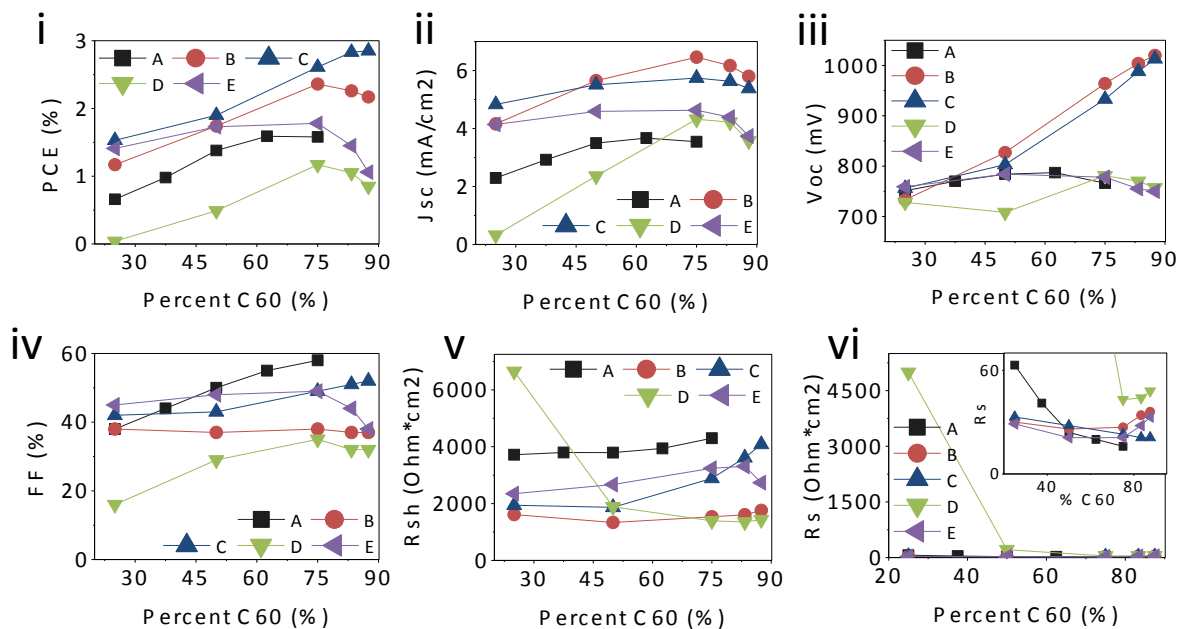


Figure 18 - Photovoltaic output parameters of ClGaPc:C₆₀ OSCs with varying device architectures and varying acceptor (C₆₀) content. Devices A through E correspond to the PHJ, BHJ, BHJ/acceptor, donor/BHJ and PM-HJ device architectures respectively. Reproduced with permission from the PCCP Owner Societies

6.3.1 From Planar Heterojunction to Bulk Heterojunction

We begin our analysis with a comparison of the most straightforward device architectures, the PHJ and BHJ (structures A and B respectively from Figure 17 and Figure 18). This follows naturally from the historical development of OSCs in literature, which evolved from the simple bilayer heterojunction (PHJ),[13] to the BHJ [14-16]. Such comparisons have also recently been made from a theoretical standpoint to better elucidate photocurrent generation [17]. This basic comparison serves as an ideal starting point to allow us to later analyze the more complicated device architectures (structures C through E) in light of our chosen suite of characterization techniques. For the PHJ, the C₆₀ content is varied by changing the layer thicknesses while maintaining a summative active layer thickness of 40 nm. In contrast, the BHJ comprises a fully mixed 40 nm active layer with varied donor-to-acceptor content.

The PHJ device (structure A) shows moderate PCE values, varying from 0.7% to 1.6% with higher performance for thicker C_{60} layers and, accordingly, for thinner ClGaPc layers. Improvement in PCE with a thicker C_{60} layer are largely due to the improvements in FF with increasing C_{60} content, as shown in Figure 18-iv. This improvement in FF is associated with an improvement (i.e. a decrease) in series resistance, as is visible from Figure 18-vi. The stark improvement in series resistance and fill factor with a thicker C_{60} layer is indicative of improved charge transport properties of C_{60} compared to ClGaPc. It is worth noting that optimal PHJ configurations that employ relatively thicker C_{60} layers in bilayer heterojunction devices have been used for numerous other small molecule donor species in literature, so the comparatively poor mobility of ClGaPc is not believed unique to this specific donor [18-20]. The relatively poor hole mobility of CuPc, a close relative of ClGaPc, compared to C_{60} is also well established in literature, and is even more strongly evident when considering hole/electron mobilities in mixed layers [21].

Interestingly, the J_{sc} is also shown to improve with increasing C_{60} layer thickness and decreasing ClGaPc layer thickness. This is counterintuitive, as ClGaPc absorbs much more strongly in the visible wavelengths compared to C_{60} . Therefore, it would seem that decreasing the ClGaPc content should decrease the amount of photocurrent generated within the OSC. In order to understand this effect, it is useful to examine the EQE spectra, as shown in the top panel (A) of Figure 19. It is clear that the photocurrent contributions from ClGaPc are maximized even at the smallest ClGaPc thickness (10 nm ClGaPc / 30 nm C_{60}), suggesting that the ClGaPc exciton diffusion length is the most critical limitation for this device architecture (i.e. excitons generated > 10 nm from the heterojunction do not yield photocurrent). Furthermore, the increase in J_{sc} with increasing C_{60} layer thickness is found to be largely due to the strong increase in EQE at 450 nm, which we have previously shown to be due to C_{60} aggregate absorption. It follows that increasing the thickness of C_{60} increases the number of C_{60} aggregates. An additional contributor to photocurrent with increasing C_{60} layer thickness is the broad increase in EQE from 530 nm to 730 nm. While this increase appears as a hypsochromatic shift of the 750-nm ClGaPc absorption, it is unclear how decreasing the

ClGaPc content would result in such a drastic shift in peak absorption – such changes are not observed in the UV/Vis absorbance of neat films of ClGaPc. Instead, we look toward the increasing C₆₀ layer thickness. To this end, it has been established that the Frenkel exciton bandgap in fullerenes can be quite low in energy – on the order of 1.7 eV to 2.3 eV [22]. Yang et al. showed that these low energy Frenkel excitons can be efficiently harvested when paired with a donor material at low donor concentrations [23].

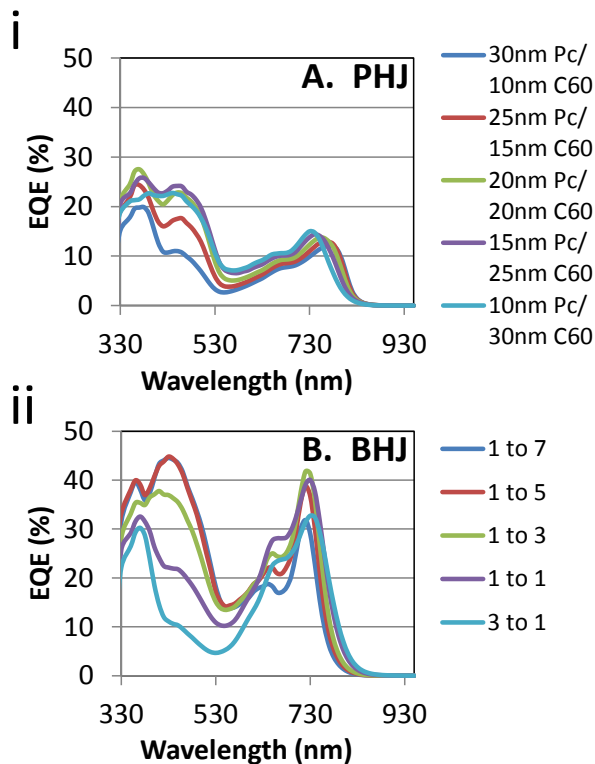


Figure 19 - External quantum efficiency spectra of the PHJ (A) and BHJ (B) ClGaPc/C₆₀ OSCs with different layer thicknesses (PHJ) and C₆₀ content (BHJ). Reproduced with permission from the PCCP Owner Societies.

To study this effect in our devices, it is necessary to decouple the EQE contributions from ClGaPc and from C₆₀. Therefore, as a rough approach to visualize the low energy C₆₀ Frenkel excitons, the 750 nm/664 nm ClGaPc peak/shoulder contributions were removed from the EQE spectra (using the ClGaPc absorption from Figure 16). The modified EQE spectra are shown in Figure 20. These data clearly show that the apparent shift in peak EQE is due to tail-end photocurrent contributions from C₆₀ from low-energy

Frenkel excitons. Consequently, the apparent shift in peak EQE increases with increasing C_{60} layer thickness.

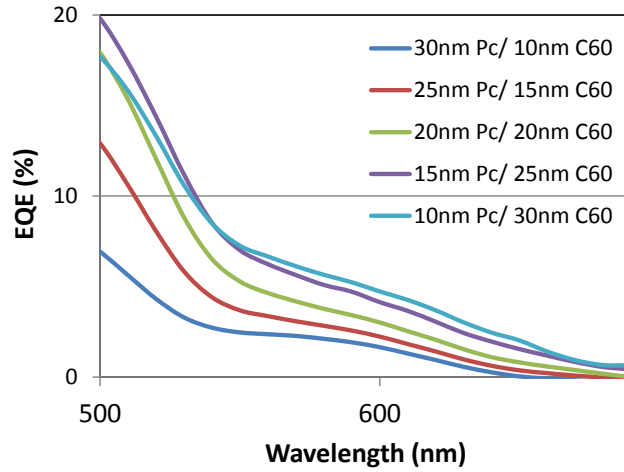


Figure 20 - Modified external quantum efficiency spectra of the PHJ ClGaPc/C₆₀ OSC with varying layer thicknesses. Pc contributions have been subtracted using normalized UV/Vis data (described in the body of the manuscript). Reproduced with permission from the PCCP Owner Societies.

It is now interesting to compare the PHJ device (structure A) architecture to those devices that use a 40-nm BHJ (structure B), as shown by their photovoltaic output parameters in Figure 18. While the PHJ maximizes its PCE at 1.6% with 62.5% C_{60} content, the BHJ reaches a substantially higher PCE of 2.4% at 75% C_{60} content. The most significant improvement in the transition from the PHJ to the BHJ structure is the increase in J_{sc} , owed to the improved exciton collection efficiency from the interpenetrating donor:acceptor network. In terms of EQE, shown in panel B of Figure 19, it is clear that the BHJ shows much improved photocurrent contributions from both ClGaPc and C_{60} at nearly all mixing ratios. As the mixing ratio is varied from ClGaPc-rich to C_{60} -rich in the BHJ, there is a clear tradeoff between ClGaPc photocurrent in the red/near-IR and C_{60} aggregate photocurrent at ~450 nm. In general, it is more difficult to form C_{60} aggregates with high ClGaPc content, and so the 450 nm absorption disappears at the 3:1 ClGaPc: C_{60} mixing ratio. Furthermore, the J_{sc} is optimized at a 1:3 ClGaPc: C_{60} mixing ratio, which balances the ClGaPc and C_{60} photocurrent contributions optimally. The transition from the PHJ to the BHJ structure offers an additional benefit to the V_{oc} , as

shown in Figure 18-iii. For the PHJ, the V_{oc} is relatively constant at $\sim 770\text{mV}$ regardless of C_{60} content; however, for the BHJ, the V_{oc} is observed to increase with increasing C_{60} content to a maximum value of 1020mV at a 1:7 ClGaPc: C_{60} mixing ratio. This enhancement in V_{oc} occurs as a consequence of a Schottky-type junction formed between the mixed layer and the high work function ITO/ MoO_3 anode. Furthermore, the Schottky junction forms when the mixed layer contains a high concentration of C_{60} . The PHJ, which uses a neat donor layer adjacent to the anode, cannot possibly benefit from this Schottky interface. Consequently, for the PHJ, the V_{oc} is dictated by the $\text{HOMO}_{\text{donor}}$ - $\text{LUMO}_{\text{acceptor}}$ offset, whereas for the Schottky device architecture (BHJ with high C_{60} content), the V_{oc} is set by the band-bending at the organic/anode interface – essentially by the C_{60} LUMO and the anode’s effective work function.

While the transition from the PHJ to the BHJ device architecture enhances the J_{sc} , it also degrades the FF due to the poor charge transport properties of the mixed organic layers compared to neat organic layers. From Figure 18-iv, the PHJ shows a 20% improved FF compared to the BHJ when both OSCs have 75% C_{60} content. This loss in FF is primarily manifested as a lower shunt resistance, suggesting that the BHJ is generally more prone to charge recombination effects. To better understand these charge recombination effects, we now examine the transient photoresponse of these two different device architectures. To this end, we excite the OSCs with a pulse of light from an LED, and then measure the photocurrent decay immediately after the light pulse. Single exponential fits are used to characterize the photocurrent decay, as per equation (1) below, to calculate the relevant time constant t .

$$I = A \cdot \exp(-Bt), \quad B = 1/\tau \quad (1)$$

The specific details of the transient photoresponse measurement technique are described in the experimental section; however, some crucial notes for analyzing these data are discussed presently. When considering transient photocurrent decay, there are two major pathways that significantly alter the fall time: sweep-out of free carriers and charge recombination. Faster sweep-out of charge carriers is generally beneficial, and helps to prevent charge trapping and space charge effects. Increased recombination,

however, also serves to reduce the fall time, and is a harmful effect that can lower the fill factor to ultimately degrade the OSC performance. It is thus emphasized that faster devices do not always correspond to more efficient devices, and it is necessary to examine the transient photocurrent measurements in the context of their device architectures and all of their photovoltaic output parameters (as shown in Figure 18).

The extracted τ values as a function of the C_{60} content within the OSC for both the PHJ (structure A) and the BHJ (structure B) are shown in Figure 21. In both cases, it is clear that the τ values, which reflect the photocurrent decay time, decrease with increasing C_{60} content (i.e. C_{60} -rich devices are ‘faster’). In the case of the PHJ, the faster photocurrent transient can be explained simply: C_{60} exhibits superior electron transport properties compared to the hole transport properties of ClGaPc. This conclusion corresponds well to the previous analysis of the OSC photovoltaic output parameters, which showed an increase in FF and decrease in series resistance with increasing C_{60} content. The reduced series resistance results in a smaller voltage drop over the active layers of the device, and so the sweep-out of free carriers is expected to be more effective. With a faster sweep-out of free carriers, the transient photocurrent decay time decreases as is observed in Figure 21.

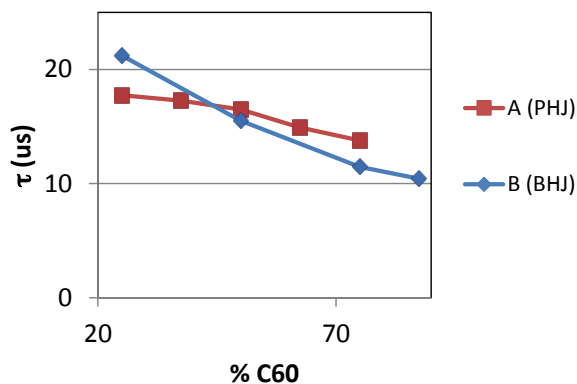


Figure 21 - Single exponential fit tau values for transient photocurrent decay (falling current) after illumination with a white LED pulse. Tau values are plotted vs. C_{60} content for PHJ and BHJ ClGaPc:/ C_{60} OSCs. Reproduced with permission from the PCCP Owner Societies.

The t values for the BHJ OSC are found to change much more strongly with varying C_{60} content compared to the PHJ OSC. With very high donor content (75% ClGaPc), the BHJ OSCs are slower than the PHJ OSCs – 21 ms versus 18 ms for the two structures respectively. This is attributed to the generally poor charge mobilities of the ClGaPc-rich mixed layer hindering sweep-out. At high C_{60} concentrations, the BHJ is much faster than the PHJ, with the BHJ having a t value of 10 ms at its highest C_{60} concentration. The ultimately faster transient photoresponse of the BHJ is attributed to an increase in charge trapping and recombination within the device. Such stipulations are supported by the generally lower fill factors of the BHJ OSCs compared to the PHJ OSCs. Charge trapping and recombination effects are especially prevalent in devices with high C_{60} content, where the low donor concentration may result in islands of donor material and, correspondingly, holes are unable to reach the anode. It is further highlighted that hole transport in C_{60} -rich OSCs would be especially problematic for holes formed far from the anode (i.e. those holes that are formed up to 40 nm away from the hole-collecting electrode). The combination of enhanced sweep-out (due to higher mixed layer C_{60} content as well as Schottky band bending effects), and increased rates of recombination (due to trapped holes deep within the mixed layer) are thus suggested to be responsible for the 10 ms t values in 1:7 ClGaPc: C_{60} BHJ OSCs. This stipulation will be revisited in section 2.2, where neat donor and acceptor layers bordering the BHJ layers are considered for their effect on transient photocurrent.

6.3.2 From Bulk Heterojunction to Planar-Mixed Structures

1. Mixed Layer/Acceptor Structures

We now consider the performance of OSCs that employ the BHJ device architecture (structure B) relative to the OSCs that employ a BHJ in combination with a neat donor and/or a neat acceptor layer (in Figure 17, structures C through E for the BHJ/acceptor, donor/BHJ and PM-HJ respectively). The BHJ/acceptor structure is particularly interesting given its very high performance in literature, with recent tetraphenyldibenzoperiflanthene (DPB): C_{70}/C_{70} OSCs granting 8.1% PCE single cell

efficiencies [24]. In the present work, the BHJ/acceptor structure employs a 20 nm ClGaPc:C₆₀ BHJ adjacent to a 20 nm neat C₆₀ layer, as compared to the 40 nm simple BHJ discussed in Section 6.3.1. As shown in Figure 18-i, both the BHJ and the BHJ/acceptor structures offer similar PCE values when the BHJ employs 25% to 75% C₆₀. Within these mixing ratios, the BHJ/acceptor structure generally has PCE values ~0.2 to 0.3% higher than the BHJ structure. The BHJ/acceptor structure is further the only device architecture that improves in PCE from the 1:3 to the 1:7 donor:acceptor mixing ratios. At a 1:7 ClGaPc:C₆₀ mixing ratio, the BHJ/acceptor structure obtains the highest PCE values for this study at 2.9%.

To understand the variations in PCE, it is necessary to examine the individual photovoltaic output parameters in greater detail. From Figure 18-iii, both the BHJ and the BHJ/acceptor structures share nearly identical V_{oc} values for all donor:acceptor ratios, increasing strongly with increasing C₆₀ concentration. This follows naturally, as both device structures include an MoO₃/ClGaPc:C₆₀ interface, with their V_{oc} values dictated by the Schottky band bending effects (as described in Section 6.3.1). From Figure 18-ii, the J_{sc} values are also similar among the two device structures, with the BHJ generally offering slightly enhanced J_{sc} values compared to the BHJ/acceptor structure with higher C₆₀ content. In terms of EQE, as shown in Figure 22-i versus Figure 22-ii, the higher J_{sc} for the simple BHJ can be understood by slightly improved ClGaPc photocurrent contributions and a strong improvement in C₆₀ aggregate photocurrent contributions. The improvement in C₆₀ aggregate photocurrent with the simple BHJ is unexpected, as it was assumed that the higher C₆₀ content in the BHJ/acceptor structure would result in higher photocurrent contributions from C₆₀. It is suggested that intermolecular C₆₀ excitons may be more efficiently separated into free carriers when the C₆₀ aggregates are homogeneously mixed with the donor, rather than being present in a pure layer and adjacent to a donor or mixed material. This stipulation is supported by our past work, which showed that a small concentration of a suitable donor is required to harvest photocurrent from the intermolecular C₆₀ excitons in any manner,^[23] thus implying that photocurrent generation from this C₆₀ aggregates is strongly dependent on the donor species. Interestingly, the BHJ/acceptor structure shows higher J_{sc} values with lower

mixed layer C_{60} content. This variation can be explained simply from Figure 22, where the presence of the neat C_{60} layer allows for meagre intermolecular C_{60} /aggregate photocurrent contributions even when C_{60} aggregates cannot be formed in the mixed layer (i.e. at 25% C_{60}).

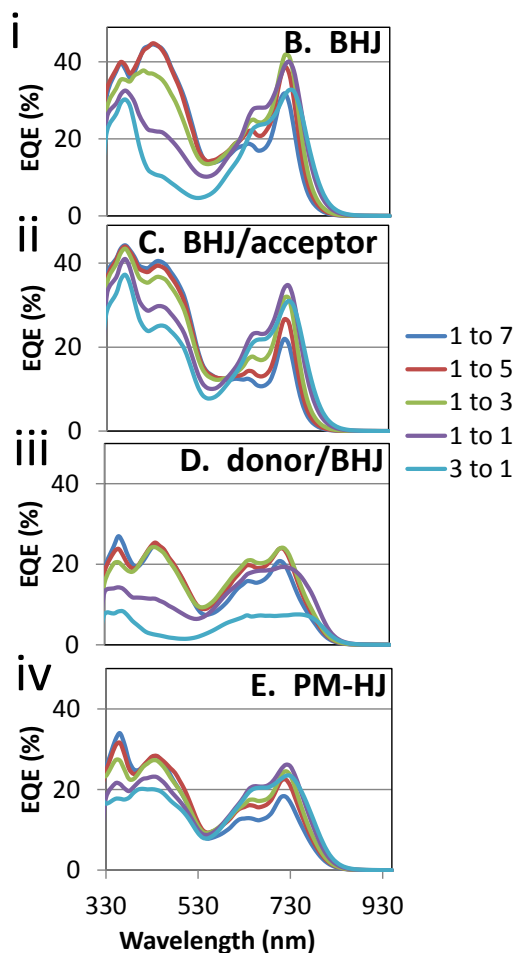


Figure 22 - External quantum efficiency spectra of the BHJ (B), BHJ/acceptor (C), donor/BHJ (D) and PM-HJ (E) ClGaPc: C_{60} OSCs with varying C_{60} content. Reproduced with permission from the PCCP Owner Societies.

Since the V_{oc} is nearly identical for both the BHJ and BHJ/acceptor structures, and the changes in J_{sc} between the structures are not significant, the main differences between these two device architectures must be understood in terms of FF. The BHJ/acceptor structure exhibits strongly improved FF values compared to the BHJ, as shown in Figure 18-iv. Furthermore, while the BHJ structure shows relatively constant

FF values with variations in mixed layer C_{60} content, the BHJ/acceptor structure shows strongly improved FF with increasing C_{60} content. Intuitively, the neat C_{60} layer has a higher electron mobility compared to the mixed layer, thereby reducing the series resistance to enhance the FF. This is especially prevalent at high C_{60} concentrations, as shown in Figure 18-vi. A second consequence of the BHJ/acceptor structure is an effective halving of the mixed layer compared to the BHJ and, more significantly, positioning the thin mixed layer close to the anode. In Section 6.3.1, it was stipulated that isolation and subsequent accumulation of holes within the mixed layer (i.e. far from the hole-collecting electrode) causes significant carrier accumulation and recombination effects. As such, it is natural that removing the mixed layer can substantially improve the fill factor. This fact is further supported by the substantial improvement (increase) in shunt resistance for the BHJ/acceptor device compared to the BHJ, especially with high C_{60} content, shown in Figure 18-v. To better understand the improvement in FF, R_s and R_{sh} , it is convenient to extend the transient photocurrent decay analysis to the BHJ/acceptor structure. The single exponential τ values from transient photocurrent decay experiments for the BHJ and the BHJ/acceptor device are shown in Figure 23, alongside the data for the remaining device structures (D and E, the donor/BHJ and PM-HJ respectively). As with the simple BHJ, the BHJ/acceptor structure exhibits decreasing τ values for increasing C_{60} content. This can similarly be attributed to more efficient sweep-out of free carriers due to the superior transport properties of C_{60} . Of more critical interest, the τ values for the BHJ/acceptor structure are noticeably higher than the simple BHJ structure for nearly all mixing ratios (excluding the 3:1 ClGaPc: C_{60} mixing ratio). In the context of the photovoltaic output parameters described above, the BHJ/acceptor structure has no donor material present deep within the device (near the cathode). As such, holes cannot become isolated and subsequently accumulate in the sparsely distributed donor regions far from the anode. Those holes that are formed do so only in the 20 nm mixed layer adjacent to the anode, where they may be more effectively collected. As such, it is expected that replacement of 20 nm of the mixed layer with neat C_{60} in the BHJ/acceptor structure reduces hole accumulation and subsequent recombination. The effect of reducing recombination is, however, to slow the device,

and so the BHJ/acceptor structure is observed to have a slower transient response (larger τ) compared to the simple BHJ.

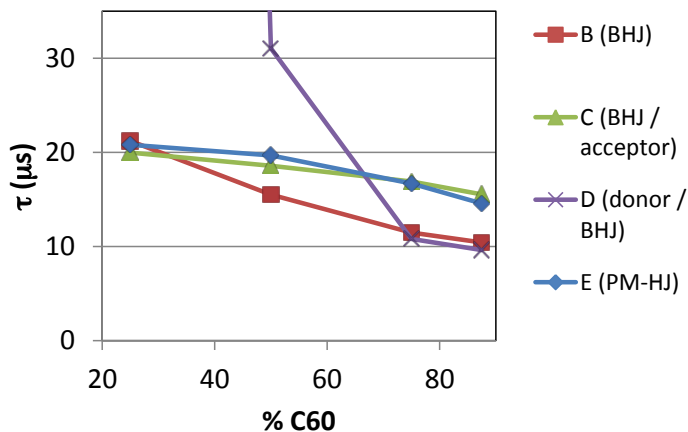


Figure 23 - Single exponential fit tau values for transient photocurrent decay (falling current) after illumination with a white LED pulse. Tau values are plotted vs. C60 content for BHJ. Reproduced with permission from the PCCP Owner Societies.

2. Donor/Mixed Layer Structures

Given the strong enhancement in device performance with the addition of the neat C₆₀ layer to the simple BHJ structure, it is natural to question the effect of instead adding a neat donor layer. As such, we now turn our attention to the donor/BHJ (structure D) as compared to the simple BHJ (structure B). From Figure 17, structure D replaces 10 nm of the mixed layer adjacent to the anode in the simple BHJ with a neat ClGaPc layer. The photovoltaic output parameters for this structure are also plotted in Figure 18, where it is immediately clear that the inclusion of the neat donor layer strongly degrades OSC performance. The donor/BHJ structure is shown to be the worst-performing device architecture, with only 0.3% PCE at a 3:1 ClGaPc:C₆₀ mixing ratio, and PCE values less than half of those of the simple BHJ structure at all other mixing ratios. The most immediate hint for this decrease in efficiency is the generally high series resistance for the donor/BHJ structure, as shown in Figure 18-vi, which increases drastically for the 3:1 and 1:1 ClGaPc:C₆₀ mixing ratios. The strong increase in series resistance follows from

the generally poor charge transport properties of ClGaPc compared to C₆₀, established with the PHJ in Section 6.3.1. The effect of poor charge transport in the donor/BHJ structure, however, is further intensified by two additional factors:

- the poor charge transport properties of the donor:acceptor mixed layer, as compared to the neat C₆₀ film that is employed in the PHJ
- the much higher increase in photogenerated carriers due to presence of the mixed layer, as compared to the single donor-acceptor interface in the PHJ

The combination of these factors results in a device architecture that is incredibly susceptible to space charge effects, and as a consequence, prone to poor charge extraction. To this end, upon illumination, a large number of holes are generated within the mixed layer of the device and traverse to the donor-mixed layer interface. The generally poor hole transport properties of the neat donor layer result in an accumulation of holes to cause space charge effects and further degrade OSC performance. If the mixed layer is highly acceptor-rich, it follows that the performance of this device structure approaches that of the 10nm ClGaPc/30 nm C₆₀ PHJ.

Taking this explanation into consideration, the performance of the donor/BHJ structure may be broken into two different regimes: mixed layers with low/moderate C₆₀ content, and mixed layers with high C₆₀ content. For the low C₆₀-content devices, the series resistance is very high due to the poor charge transport characteristics of the neat donor layer and donor-rich mixed layer. Furthermore, comparing the donor/BHJ structure to the simple BHJ structure at 3:1 and 1:1 donor-acceptor ratios, the neat donor layer effectively acts as a charge blocking layer, resulting in a strong increase in the shunt resistance, as observed in Figure 18-v. It follows that both the FF and J_{sc} suffer strongly at these mixing ratios. As shown by the EQE in Figure 22-iii, photocurrent contributions are strongly decreased across all wavelengths for these mixing ratios. The photocurrent contributions also lose their fine spectral detail, with the peak and shoulder of the ClGaPc photocurrent merging together. Furthermore, both 3:1 and 1:1 ClGaPc mixing ratios provide virtually no C₆₀ aggregate photocurrent contributions, as the C₆₀ content is too low to form aggregates. The poor FF at these mixing ratios is supported by the substantial increase in the time constant of the transient photoresponse of the donor/BHJ

device, shown in Figure 23. Specifically, the t values increase drastically to 31 ms for 1:1 ClGaPc:C₆₀ and 520 ms for 3:1 ClGaPc:C₆₀ (the latter point not shown in the figure). While the poor charge transport properties of the neat donor layer and the donor-rich mixed layer clearly limit the performance of these OSCs, it is worth noting that the charges present within these devices are incredibly long-lived. To this end, the photogenerated carriers are not being swept out quickly; however, they are also not undergoing rapid recombination.

While increasing the C₆₀ content in the mixed layer can alleviate charge transport problems in the donor/BHJ structure, its ultimate performance is still quite poor. Specifically, since this structure employs a neat donor layer, and thus lacks the interface between the mixed layer and the high work function anode, it no longer benefits from the Schottky interface enhancement to V_{oc} . This is observed clearly in Figure 18-iii, where the V_{oc} for structure D generally tracks the V_{oc} values set by the PHJ (structure A). The J_{sc} for the donor/BHJ structure is also lower than that of the BHJ, as the excitons that are formed in the neat ClGaPc layer far from the mixed layer interface do not generate photocurrent. This follows from the low exciton diffusion length for ClGaPc established with the PHJ structure in Section 6.3.1. This effect is clearly visible in the EQE in Figure 22, where the peak photocurrent contributions from the ClGaPc in the donor/BHJ structure (1:3 to 1:7 mixing ratios) are much lower than that of the simple BHJ device, in spite of the 10 nm neat ClGaPc layer. It is also observed that, with the replacement of 10 nm ClGaPc:C₆₀ with 10 nm of ClGaPc (i.e. comparing structure B to D), the C₆₀ photocurrent contributions are reduced accordingly. Interestingly, the t values extracted from the transient photocurrent experiments for the donor/BHJ structure are nearly identical to those of the simple BHJ when both structures employ high C₆₀ content in their mixed layer. This is observed clearly in Figure 23 for 75% and 87.5% C₆₀ content. The fast response at these mixing ratios follows from the high level of recombination due to holes formed in isolated pockets of donor deep within the mixed layer. This is the same effect established for the simple BHJ in Section 6.3.1 – essentially trapped holes formed far from the anode are unable to traverse the mixed layer due to the mixed layer's low donor content.

6.3.3 Full Planar-Mixed Molecular Heterojunction

The final device architecture studied in this work is the full PM-HJ (structure E), which makes use of both a neat donor and a neat acceptor layer. When compared to the simple BHJ (structure B), 10 nm of the mixed layer near the anode is replaced with neat ClGaPc, and 20 nm of the mixed layer near the cathode is replaced with C₆₀. Therefore, this final device structure encompasses both of the alterations made for the BHJ/acceptor structure and the donor/BHJ structures examined above. From Figure 18-i, the PM-HJ structure generates devices with moderate PCE values in between those of the other device structures examined in this work. Furthermore, the PM-HJ structure has PCE values that are the least dependent on C₆₀ content in the mixed layer – between 1.4% and 1.8% for 3:1 to 1:5 ClGaPc:C₆₀ mixing ratios. One major contributor to this independence of PCE on mixing ratio is that the PM-HJ structure exhibits a relatively constant V_{oc} (Figure 18-iii). As noted for the donor/BHJ structure, this is due to the neat ClGaPc layer separating the high work function anode from the C₆₀-rich layer, preventing prevent the Schottky device architecture. Consequently, the V_{oc} is simply set by the HOMO_{donor}-LUMO_{acceptor} offset, and it does not benefit from the Schottky interface enhancement observed in structures B and C. In Figure 18-ii, the PM-HJ structure's J_{sc} is also shown to be relatively constant with variations in C₆₀, with values near ~4mA/cm² for all mixing ratios. From Figure 22, this translates to EQE spectra with much less drastic variations in intensity, especially when compared to the simple BHJ. This is due to the fact that, with neat layers of both ClGaPc and C₆₀, there are always moderate contributions to photocurrent from both the ClGaPc and C₆₀. Furthermore, as the C₆₀ content is increased in the mixed layer, any loss in photocurrent from ClGaPc is compensated by an increase in photocurrent from the C₆₀ aggregate band (and vice versa). Regardless, the J_{sc} for the PM-HJ structure is, as expected, shown to be lower than that of the simple BHJ, since the simple BHJ has a much thicker mixed layer to generate a substantially larger number of free carriers from photogenerated excitons.

Intriguingly, while the PM-HJ structure makes use of a neat donor layer, it does not suffer from the same increases in series resistances as observed for the donor/BHJ

structure. It is thus shown to be the combination of the neat donor layer and a thick (> 10 nm) mixed layer (especially when the mixed layer has low C_{60} content) to be the cause of strongly increased series resistance for the donor/BHJ structure. In fact, the PM-HJ structure is shown to have some of the best shunt and series resistances (highest and lowest in Figure 18-v and Figure 18-vi respectively) for the various device architectures studied in this work. The devices that outperform the PM-HJ in the regard are those that employ the PHJ structure, and those that use the BHJ/acceptor structure with high C_{60} -content mixed layers – the latter was shown to be the highest performing structure in the present study. The PM-HJ structure's high shunt resistances and low series resistances translate to a relatively high FF for the PM-HJ for most mixing ratios, as shown in Figure 18-iv (especially when compared to the simple BHJ). The high FF is explained by the fact that this device structure replaces a large portion of the mixed layer, known to have poor charge transport characteristics and a high propensity for charge recombination, with neat layers that lessen such issues. The operation of the PM-HJ is thus similar to that of the PHJ examined first in Section 6.3.1, but with a higher capacity for photocurrent generation due its use of a 10 nm mixed layer. At very high C_{60} concentrations in its mixed layer, however, the PM-HJ shows a slight reduction in FF, which can be attributed to poor hole transport characteristics through the mixed layer, and increased hole accumulation/recombination effects.

The general transient photocurrent behavior for the PM-HJ is similar to that of the other device structures examined throughout this work. As shown in Figure 23, increasing the C_{60} content in the mixed layer serves to decrease the time constant t , implying that the C_{60} -rich PM-HJ device is faster. As with the simple BHJ, this is attributed to enhanced sweep-out of free carriers, owing to the better charge transport characteristics of C_{60} compared to ClGaPc. The ultimate t value at the highest C_{60} concentration, however, is higher than that of the simple BHJ and the donor/BHJ structure. This further verifies our previous stipulations regarding hole accumulation and trapping deep within the mixed layer (i.e. far from the anode). Since the PM-HJ employs only a 10-nm thin mixed layer, and has a neat 20-nm C_{60} layer near the cathode, isolated domains can only be formed 10 to 20 nm away from the anode. As such, isolated holes

cannot be formed as far away from the anode, and recombination effects due to hole trapping is reduced. By reducing recombination effects, it follows that charges generally show longer lifetimes, as is observed for the PM-HJ structure.

The PM-HJ structure has been shown to generate OSCs with high FF values relative to the other mixed-layer structures examined in this work. However, its maximum FF of ~50% leaves significant room for improvement, especially with optimized polymer OSCs proven to be capable of FF values of 75% [25]. To further understand the limitations of this device architecture, we extended our transient photocurrent analysis by employing colored LEDs with much higher brightness values at the materials' major absorption wavelengths (blue and red LEDs for C₆₀ and ClGaPc respectively). The effect is to substantially increase the number of excitons generated at a given LED power. In literature, it has been shown that increasing the number of excitons, and thus the number of photogenerated carriers, can lead to space charge effects visible in transient photocurrent experiments [6-8,26]. In a transient photocurrent experiment, space charge effects are manifested as a peak increase in photocurrent and subsequent stabilization at lower photocurrents with the initial pulse of light. In some cases, authors have noticed a negative photocurrent peak recovery at the end of the light pulse. The negative photocurrent implies the injection of carriers from the contacts to neutralize carriers that remain within the device due to insufficient sweep-out, essentially arising from space charge effects. It is also worth noting that this negative recovery is strongly dependent on the device architecture, as the carriers must favor accumulation over various potential avenues for recombination (i.e. the charge carrier lifetime must be quite long). This negative photocurrent recovery is demonstrated in Figure 24-i, which shows the transient photocurrent decay for a PM-HJ ClGaPc:C₆₀ OSC with both dim and bright light pulses. In the case of a dim white LED pulse, no negative transient is observed, but in the case of a bright blue LED pulse, a significant negative spike and subsequent recovery is observed. Furthermore, when either bright red or blue LED light pulses are used, all of the mixing ratios in the PM-HJ structure show this negative photocurrent recovery at the end of the light pulse. However, this behavior is not observed for any of the other device architectures – it is unique to the structure E, the full

PM-HJ, and it emphasizes the generally low recombination rates and high FF with this device architecture.

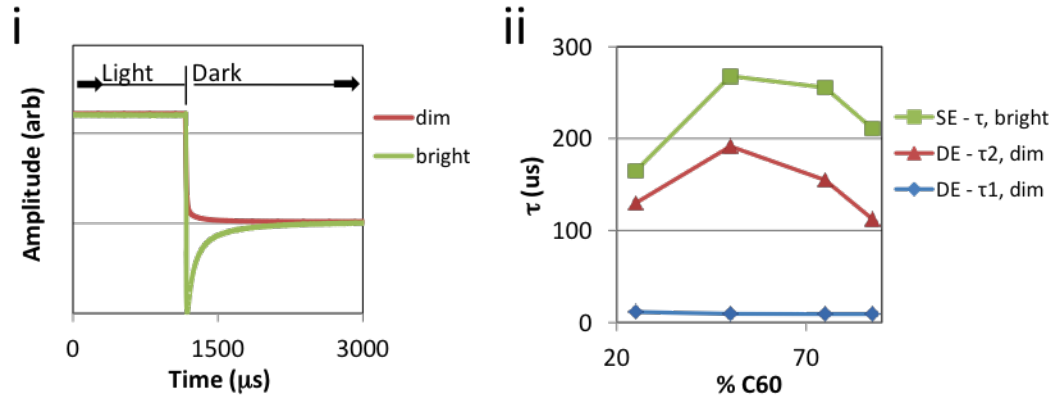


Figure 24 - i. Transient photocurrent decay of a 1:7 ClGaPc:C60 PM-HJ OSC under bright light and dim light. ii. Single exponential fit (SE) and double exponential fit (DE) t values for the transient photocurrent decays of PM-HJ ClGaPc:C₆₀ OSCs. Reproduced with permission from the PCCP Owner Societies.

In order to better understand this effect, a single exponential fit was performed on the negative photocurrent transient recoveries (using a bright blue LED pulse) for the PM-HJ devices, as per equation (1). The t values extracted from this analysis are shown in Figure 24-ii under the label ‘SE – t , bright,’ where SE refers to a single exponential fit. This negative transient recovery occurs over a much longer timescale (hundreds of ms) than the simple transient photocurrent decay observed with dim white light (tens of ms, Figure 23). This is due to the slow injection of carriers from the electrodes to compensate for the accumulated charges within the device, especially compared to the fast sweep-out of free carriers in the PM-HJ under dim white light where space charge effects are not as severe. We also performed a biexponential fit, as per equation (2), on the basic photocurrent transient decay curves of the same devices illuminated with a dim white LED light pulse (i.e. those curves fitted previously with a single exponential term in Figure 23).

$$I = A_1 \cdot \exp(-B_1 t) + A_2 \cdot \exp(-B_2 t), \quad B_1 = 1/\tau_1; \quad B_2 = 1/\tau_2 \quad (2)$$

In this case, the biexponential fit provides slightly better R^2 values (generally >0.999 versus >0.9), indicating that the added exponential term allows for a more accurate representation of the data. The biexponential fitted t_1 and t_2 values for the PM-HJ devices with varying mixing ratios are also shown in Figure 24-ii. The fast t_1 component of the biexponential fit is relatively constant at ~ 10 ms for all mixing ratios. More significantly, from Figure 24, the slow t_2 component of the fit is found to have the same variations with mixing ratio and a similar timing as the t values extracted for the negative transient recovery (when illuminated with the bright blue LED pulse). It is thus strongly implied that the slow component of the biexponential fit is related to a weak space charge effect, which is present even under dim white light. In other words, even with low light intensity, the PM-HJ structure is susceptible to charge accumulation and associated space charge effects. These space charge effects become dominant with more intense light and, correspondingly, a higher exciton generation rate that leads to a larger number of charges within the photo-active layers. As the space charge effects become dominant, the transient photoresponse of the device slows. Furthermore, in the case where the charges do not rapidly recombine at the end of the light pulse, a negative photocurrent transient is observed.

Interestingly, while structures C and D (BHJ/acceptor and donor/BHJ respectively) did not show the negative photocurrent transients with bright red/blue LED pulses, their transient photocurrent decays were also successfully fit with a biexponential model (for dim white LED pulses). To this end, these structures' photocurrent decays showed slightly improved R^2 values with biexponential fits, had non-zero pre-exponents (A_1 and A_2 in equation (2)) and exhibited realistic t_1 and t_2 values (with a fast t_1 and a slow t_2 for each fit). However, when the biexponential fit was applied to the photocurrent decays of structures A and B (the PHJ and simple BHJ respectively), the second pre-exponential term always converged to zero, indicating that the single exponential model already adequately described their transients. Having established the slow t_2 value in the biexponential fit to be related to space charge effects, it follows that structures C, D and E may all suffer from weak space charge effects. The commonality in these structures is the combination of a mixed layer with a neat donor and/or acceptor layer. Upon

illumination, the interface between the mixed layer and the neat donor or acceptor layer is a region of high charge density, as this interface contains charges from two exciton sources:

- excitons formed throughout the full thickness of the mixed layer
- excitons formed in the neat layer and within the exciton diffusion length of the mixed/pure interface

The large concentration of free carriers at this interface is a potential contributor to space charge effects, especially in light of the generally poor hole transport within these materials, as established through our previous analysis. In the case of structure C (BHJ/acceptor), the large concentration of holes at this interface must traverse the entire thickness of the mixed layer, with the mixed layer known to have poor hole transport properties. In the case of structure D (donor/BHJ), the large number of holes must traverse the full thickness of the neat ClGaPc layer, which has also been demonstrated to have relatively poor hole transport properties especially compared to electron transport in C₆₀. Structure E (full PM-HJ) has both interfaces present, and so it suffers from these effects most strongly. While space charge effects have been noted as a strong limiter toward device performance for the PM-HJ, the remarkably long free carrier lifetimes in this device architecture are re-emphasized. The PM-HJ structure is therefore a promising device architecture for high performance OSCs, but only in the case where both the donor and acceptor materials are optimized for high free carrier mobilities and thus to prevent space charge effects. An ideally designed donor would also optimally have an HOMO to provide V_{oc} values near 1V so that Schottky effects do not provide substantial performance enhancements – essentially granting greater freedom in device architecture. The success of more complicated device structures in literature, such as the p-i-n architecture, or those that employ gradient mixed layers, [15] can at least in part be attributed to their tackling space charge effects. In the prior case, this is accomplished explicitly by bolstering the charge transport properties of the neat layers. In the latter case, space charge effects can be minimized implicitly by minimizing the accumulation of charges at any specific region within the photo-active layers.

6.4 Conclusions

In this work, we have shown that the optimal device architecture relates strongly to the charge transport characteristics of the active materials, and is ultimately limited by poor donor and mixed layer hole mobility for the ClGaPc:C₆₀ materials system. To this end, the highest performing OSCs are found to employ a BHJ/acceptor device structure. By combining photovoltaic output parameters with EQE spectra and transient photocurrent measurements, we have demonstrated that the BHJ/acceptor structure optimizes the tradeoff between charge generation and charge collection. The improvement in performance with device architecture is strongly associated with enhanced sweep-out, and thus associated with minimizing both charge trapping and charge recombination effects. This is further accomplished while maintaining a relatively high J_{sc} by balancing ClGaPc photocurrent contributions with the contributions from intermolecular/aggregate C₆₀. The BHJ/acceptor structure also benefits from Schottky contact effects to increase its V_{oc} to values in excess of 1V, and so its performance is maximized at very high C₆₀ ratios. In contrast, the full PM-HJ device structure, which employs both a neat donor and a neat acceptor layer, effectively reduces charge recombination, but ultimately suffers from hole accumulation and space charge effects that limit its sweep-out. Transient photocurrent measurements suggest that space charge effects may be present and potentially problematic for any device architecture that employs both neat and mixed layers in any combination. Doped transport layers and gradient mixed layers are suggested as avenues to minimize these effects and to achieve high efficiency vacuum deposited small molecule OSCs.

Chapter 7 – Effect of PTCDA and CuI Templating on Hole Mobility and Performance of Phthalocyanine/C60 Organic Solar Cells

Chapter Summary

Molecular templating is emerging as a new avenue for enhancing the efficiency of phthalocyanine based organic solar cells. Templating forces the phthalocyanine molecules to lie flat on the substrate leading to improved electrical and optical properties. In this study, we examine the interplay between molecular templating, charge transport and photovoltaic performance of zinc phthalocyanine, chloro-aluminum phthalocyanine and boron subphthalocyanine planar heterojunction (PHJ) OSCs. We use both perylenetetracarboxylic dianhydride (PTCDA) and copper iodide (CuI) as templating layers in order to compare their templating efficacy in PHJ OSCs and differences in interaction with each phthalocyanine. This chapter addresses objectives 3 and 4 of the research work.

PTCDA-templated ZnPc OSCs show a 65.7% increase in efficiency and CuI-templated ZnPc OSCs show a 43.4% increase in efficiency over control OSCs. The performance improvements in templated ZnPc OSCs are mainly due to improved exciton dissociation in the device. Contrary to expectations, templating reduces charge mobility in ZnPc. PTCDA-templated ClAlPc PHJ OSCs show a 98.7% increase in efficiency and CuI-templated ClAlPc PHJ OSCs show a 12.7% increase in efficiency over control OSCs. The performance improvements in templated ClAlPc OSCs are due to improvements in both exciton dissociation efficiency and charge transport. SubPc is only templated by PTCDA and is unaffected by CuI. However, PTCDA templated SubPc devices show reduced exciton dissociation and hence lower performance over controls. Our findings indicate that the interaction between the phthalocyanines and templating layers are unique to each combination and affect different aspects of OSC device physics.

7.1 Introduction

Small-molecule organic solar cells have made large gains in efficiency in recent years, reaching values as high as 8% [1]. Traditionally, the choice of donor/acceptor materials and device architecture has been used to increase the efficiency of these OSCs [2–8]. In recent times, control over the molecular orientation of the donor material has emerged as a new avenue to realize large efficiency gains in OSCs [9–17].

The molecular orientation of a material affects its light absorption properties, charge transport through the material and its exciton dynamics as described in detail in Section 1.2 [14,15,18–22]. As a result, the molecular orientation plays a crucial role in influencing the J_{sc} of an OSC. Absorption is maximized when the transition dipole moment of the molecule is parallel to the electric field of oncoming light [14]. Charge transport and exciton diffusion should be maximized in a material along the π - π stacking direction of its molecular planes. Since OSCs utilize vertical device architectures, molecules with their planes lying flat on the substrate are preferred to molecules with their planes arranged vertically on the substrate.

Recent reports in literature have shown that the molecular orientation of phthalocyanine donor materials can be influenced by the use of templating layers such as perylenetetracarboxylic dianhydride (PTCDA) or copper iodide (CuI) [17,23–29]. A detailed background of molecular templating is provided in Section 2.2. When phthalocyanines are deposited on top of weakly interacting substrates such as ITO/MoO₃, their molecules arrange themselves vertically or with a moderate tilt angle (from the vertical) on the substrate [14]. On the other hand, when they are deposited on top of templating layers, the phthalocyanine molecules lie with their planes flat on the substrate or with a large tilt angle from the vertical [11,29,30]. For example, ZnPc molecules align with their planes vertical (tilt angle $\sim 0^\circ$) on the substrate when deposited on weakly interacting substrates such as ITO/MoO₃ [14,16]. However, when deposited on CuI, the tilt angle of ZnPc molecules increases to approximately 55° . Similarly, ClAlPc molecules

have a random orientation on ITO/MoO₃ but a large tilt angle of 76° when deposited on PTCDA [25].

The use of templating layers in planar heterojunction (PHJ) OSCs results in large gains in efficiency due to the more favorable molecular orientation of the phthalocyanine donor material. However, the degree of improvement in performance varies widely depending on the choice of templating layer and the particular phthalocyanine used. It is still unclear to what extent templating affects the three main OSC processes – absorption, exciton dissociation and charge transport. Reports in literature have focused on understanding how templating layers affect absorption and exciton dynamics but there have been no works that examine the effect of templating on the hole transport in phthalocyanines. In order to fully understand the impact of varying molecular orientation on OSC performance, it is important to understand how hole transport is affected in addition to absorption and exciton diffusion.

In this study, we analyze the factors influencing the performance enhancement of PTCDA and CuI templated ZnPc, ClAlPc and SubPc planar heterojunction (PHJ) OSCs by comparing the PV parameters, external quantum efficiency (EQE) and UV/vis absorption. In addition, we focus on understanding how hole transport is affected upon templating by measuring the space charge limited conductivity (SCLC) hole mobilities of templated and control phthalocyanines. Both PTCDA and CuI are used in this study because they are the main templating layers studied in literature. We conduct a systematic study of the interaction of each phthalocyanine with the two templating layers in order to elucidate the differences between them and how they affect OSC performance.

7.2 Experimental Methods

The general fabrication procedure for all OSCs is outlined in Section 4.1. PHJ OSCs were fabricated with the device structure: ITO/MoO₃ (7 nm)/PTCDA or CuI (2 nm or 0 nm)/Phthalocyanine donor/C60 (35 nm)/BCP (8 nm)/Al (100 nm). 15 nm of ZnPc, 15 nm of ClAlPc or 7 nm of SubPc were used as donor materials in the PHJ OSCs. 2 nm

PTCDA or 2 nm CuI was used as a templating layer to modify the molecular orientation of the phthalocyanine donor materials. Control devices had no templating layer and the anode was simply composed of ITO/MoO₃. C60 was used as the acceptor in both PHJ OSCs. BCP was used as the exciton blocking layer and Al was used as the cathode.

Unipolar hole-only devices were fabricated with the structure: ITO/MoO₃ (7 nm)/phthalocyanine (100 nm)/MoO₃ (25 nm)/Al (100 nm). Templated unipolar devices were fabricated by depositing 2 nm of PTCDA or CuI before the phthalocyanine. In addition, unipolar devices with PTCDA or CuI deposited on top of the phthalocyanine close to the MoO₃/Al interface were also fabricated. These devices were used to rule out possible contributions of interface modification to the measured hole-mobility. Hole mobility was calculated by using space charge limited current (SCLC) equations as given in [31].

The PV parameters, external quantum efficiency (EQE) spectra, UV/Visible absorption spectra and atomic force microscopy images were obtained as described in Section 4.2

7.3 Results and Discussion

7.3.1 Effect of Templating on Photovoltaic Properties

Table 5 shows the PV parameters of control and templated ZnPc, ClAlPc and SubPc PHJ OSCs.

Table 5: PV Parameters of control and PTCDA templated ZnPc, ClAlPc and SubPc PHJ OSCs

Donor Material	Templating Layer	J_{sc} (mA/cm ²)	V_{oc} (mV)	FF (%)	Efficiency (%)	Shunt Resistance (kOhm.cm ²)	Series Resistance (Ohm.cm ²)
ZnPc	Control	3.19	438.44	47.64	0.67	3.32	20.60
	PTCDA	4.10	512.76	52.77	1.11	5.42	14.14
	CuI	3.93	487.68	49.93	0.96	4.39	17.17
ClAlPc	Control	3.22	699.43	35.28	0.79	2.60	62.61
	PTCDA	4.33	692.99	52.23	1.57	3.25	23.42
	CuI	4.29	392.19	52.84	0.89	2.35	8.73
SubPc	Control	3.82	1036.84	61.59	2.44	6.92	14.18
	PTCDA	3.55	1062.19	58.74	2.21	7.78	18.54

When templated with PTCDA, the J_{sc} , V_{oc} and FF of the ZnPc PHJ OSC increase by 28.5%, 17.0% and 10.8% respectively. As a result, the efficiency increases by 65.7%. Templating with CuI results in lower performance gains than templating with PTCDA. CuI-templated ZnPc PHJ OSCs show a 23.2% increase in J_{sc} , 11.2% increase in V_{oc} and 4.8% increase in FF leading to a 43.3% increase in efficiency.

Interestingly, compared to templated ZnPc OSCs, templating the ClAlPc OSCs with PTCDA provides much larger gains in J_{sc} and FF. The J_{sc} and FF of PTCDA templated ClAlPc OSCs increase by 34.5% and 48.0% respectively leading to an efficiency increase of 98.7%. Unlike PTCDA templated ZnPc OSCs, the V_{oc} of PTCDA templated ClAlPc OSCs drops slightly from 699.43 mV to 692.99 mV. CuI templated ClAlPc OSCs show similar gains in J_{sc} (+33.2%) and FF (+49.8%) compared to the PTCDA templated OSCs. However, the V_{oc} of CuI templated ClAlPc OSCs decreases by 43.9% leading to much smaller gains in overall power conversion efficiency (+12.7%).

Finally, in contrast to the both ZnPc and ClAlPc OSCs, PTCDA templated SubPc OSCs have lower J_{sc} (-7.1%) and FF (-4.6%), which leads to a reduced PCE (-9.4%).

7.3.2 Effect of Templating on EQE and Absorption

In order to understand the changes in the PV properties due to templating, the external quantum efficiency (EQE) and UV/visible absorption of the OSCs were measured. Figure 25 shows the EQE spectra and Figure 26 shows the UV/Vis absorption spectra of templated and control PHJ OSCs.

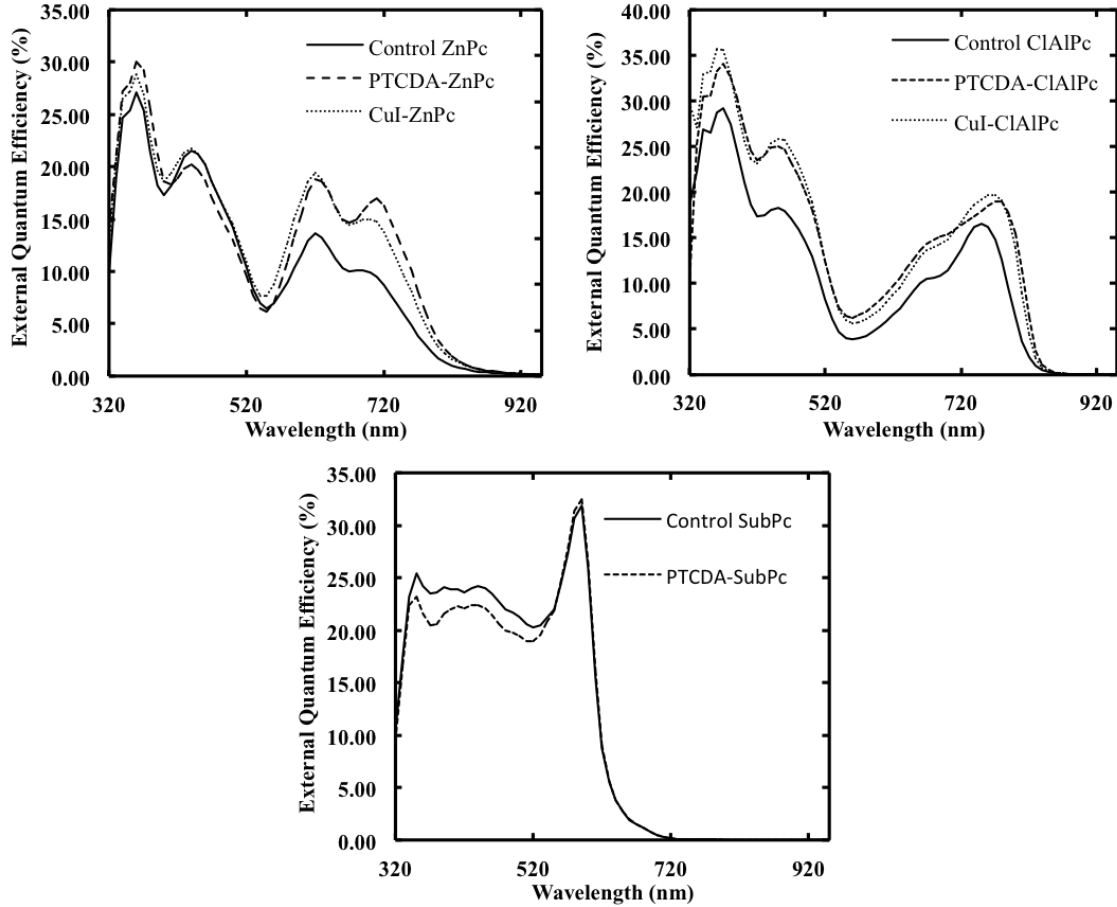


Figure 25: EQE spectra of control and PTCDA templated ZnPc, CIAIPc and SubPc PHJ OSCs

As shown in Figure 25, PTCDA and CuI templated ZnPc OSCs demonstrate a substantial increase in EQE in the wavelengths corresponding to ZnPc absorption ($\lambda = 550$ nm to 950 nm). In this wavelength range, the EQE of PTCDA templated OSCs increases by 57.5% on average and CuI templated OSCs increases by 49.7% on average. In addition, PTCDA templating also leads to a small decrease in the EQE in the C_{60} absorption band ($\lambda = 400$ nm – 550 nm), but this is not seen in the CuI templated OSCs.

In this wavelength range, the EQE of the PTCDA templated devices is 5.7% lower than controls on average. Over the entire wavelength range of 400 nm – 950 nm, PTCDA templating results in a 40.6% EQE increase and CuI templating results in a 37.3% EQE increase. The differences in EQE agree well with the differences in J_{sc} observed in PTCDA and CuI templated ZnPc OSCs.

Figure 26 shows the UV/Vis absorption spectrum of templated and control ZnPc OSCs. PTCDA templated ZnPc OSCs show a 8.3% average increase in absorption in the ZnPc band from 550 nm – 800 nm and a 6.7% average increase in absorption in the in the C₆₀ band from 400 nm – 500 nm. In comparison, CuI templated ZnPc OSCs show only a 5.3% average increase in absorption in the ZnPc band and only a 0.2% average increase in absorption in the C₆₀ absorption band. First, based on the average increase in absorption in the ZnPc band, PTCDA seems to be more effective at increasing the absorption cross section of ZnPc than CuI, indicating that PTCDA is a better templating layer for ZnPc. Secondly, the ZnPc absorption enhancements in both PTCDA and CuI templated devices are much lower than the observed EQE enhancements suggesting that increases in absorption only explain part of the increases in EQE. Therefore, exciton dissociation or charge transport must be improved in templated ZnPc OSCs to account for the remaining EQE enhancement. Finally, the EQE decreases whereas the UV/Vis absorption increases in the C₆₀ absorption band for PTCDA templated ZnPc OSCs. The increase in UV/Vis absorption in this band for PTCDA templated devices could be due to the presence of PTCDA, which demonstrates strong absorption from 400 nm – 600 nm, or also due to a change in the morphology of C₆₀ itself. Modified interference patterns within the OSC arising from the different optical constants of templated ZnPc could also lead to changes in absorption over this wavelength [8]. The decrease in EQE for this band could be due to reduced exciton dissociation or charge transport from templating. The effect of templating on charge transport is investigated in the next section.

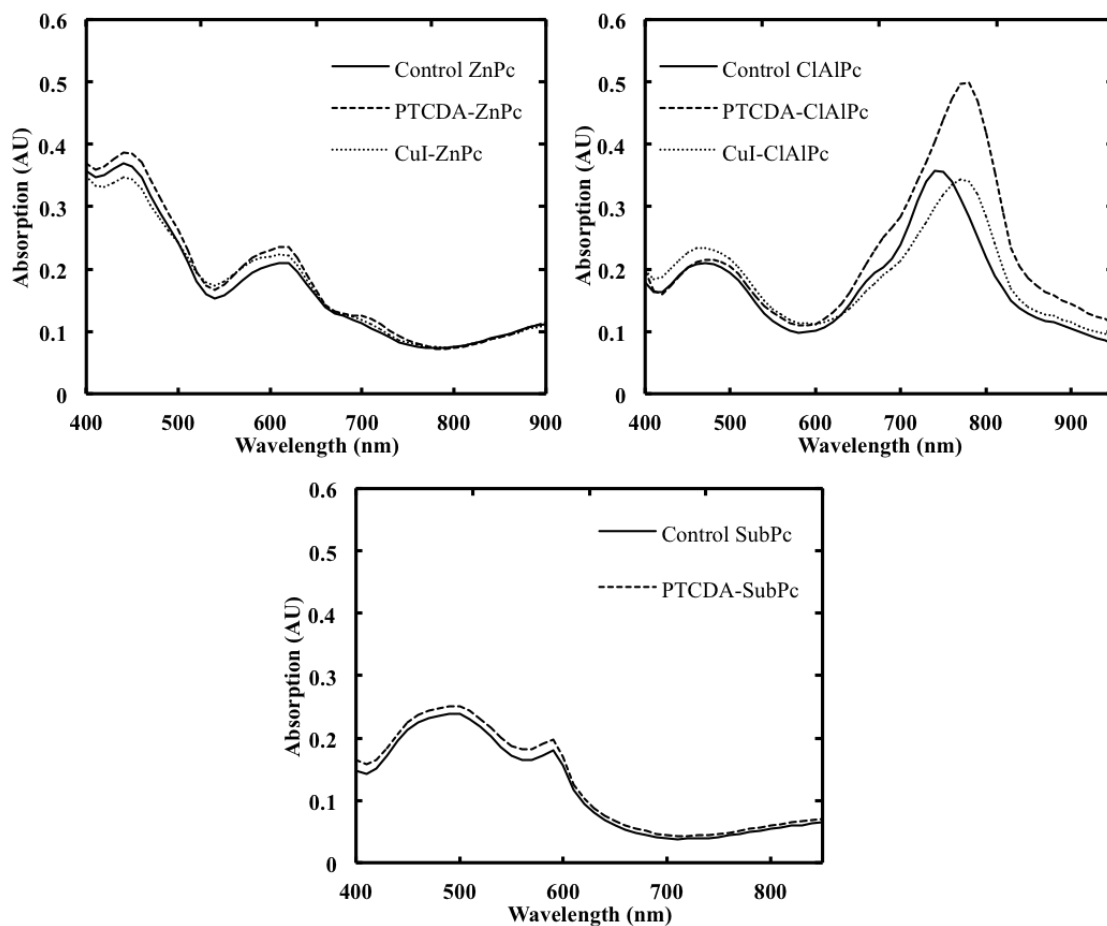


Figure 26: UV/vis absorption spectra of templated and control ZnPc and ClAlPc PHJ OSCs

In contrast to ZnPc OSCs, templated ClAlPc PHJ OSCs show broadband EQE enhancement over all wavelengths compared to controls, as seen in Figure 25b. The magnitude of EQE enhancement is approximately the same, around 58%, for both CuI and PTCDA templated OSCs over the wavelength range of 400 nm to 950 nm. The EQE enhancements agree well with the observed J_{sc} enhancements for PTCDA and CuI templated ClAlPc OSCs. Compared to control devices, there is also a red shift of 40 nm in the EQE wavelengths corresponding to ClAlPc absorption ($\lambda = 600 \text{ nm} - 850 \text{ nm}$) in the templated devices.

As seen in Figure 26, PTCDA-templated ClAlPc OSCs show an increase in absorption intensity and significant redshift upon templating in the wavelength range from 600 nm to beyond 900 nm compared to controls. The control ClAlPc absorption

peak is at 740 nm whereas the PTCDA-templated CIAIPc absorption peak is at 780 nm. The absorption intensity of PTCDA templated CIAIPc at 780 nm is 39.7% higher than the absorption intensity of control CIAIPc at 740 nm.

The presence of the red shift in the absorption spectrum suggests the evolution of a new lower bandgap phase of CIAIPc in the PTCDA templated OSCs. The small drop in V_{oc} in templated devices can be explained by the presence of a new lower bandgap phase of CIAIPc, which would necessarily have a smaller $HOMO_{donor}$ - $LUMO_{acceptor}$ energy level offset, leading to lower V_{oc} .

The increase in absorption suggests that the molecules are oriented face-on on the substrate leading to a larger absorption cross-section. Similar to PTCDA templated ZnPc OSCs, there is a small 4.1% increase in absorption from $\lambda = 400 \text{ nm} - 550 \text{ nm}$. This increase in absorption could be due to absorption from PTCDA or due to changes in C_{60} morphology. Modified interference patterns within the OSC arising from the different optical constants of templated CIAIPc could also lead to changes in absorption in this wavelength range.

CuI-templated CIAIPc OSCs only show a 40nm red shift in the CIAIPc absorption region without any increase in absorption intensity. This suggests that CuI templating of CIAIPc results in the evolution of the new lower bandgap phase of CIAIPc but not necessarily in reorientation of the molecules towards the face-on orientation. Finally, CuI templated CIAIPc OSCs show a 12.8% increase in C_{60} absorption from 400 nm – 550 nm. This increase in absorption could be due to modified interference patterns within the OSC due to different optical constants of templated CIAIPc or due to changes in the C_{60} morphology itself.

The increase in intensity of CIAIPc absorption when templated with PTCDA could completely account for the increase in EQE seen in the CIAIPc absorption bands. However, it does not explain why the PTCDA templated CIAIPc OSCs show broadband EQE enhancement over the C_{60} absorption bands, where there is relatively little absorption enhancement. Secondly, despite the lack of absorption enhancement in CuI-

templated ClAlPc OSCs in the ClAlPc absorption band, the EQE increase is comparable to that of PTCDA-templated OSCs. This suggests that the charge transport or exciton dissociation is enhanced by the presence of the new phase of ClAlPc and is the main driver for the improvements in J_{sc} observed. The impact of templating on hole transport in ClAlPc is investigated in the next section.

Finally, PTCDA templated SubPc PHJ OSCs show a 6.8% decrease in EQE in the wavelength corresponding to C_{60} absorption ($\lambda = 400 - 500$ nm) on average and almost no change in the wavelengths corresponding to SubPc absorption ($\lambda = 550$ nm – 750 nm). This is reflected in the lower J_{sc} of the PTCDA templated SubPc devices.

PTCDA templated SubPc OSCs show a small increase in absorption from $\lambda = 400$ nm to 700 nm which suggests that PTCDA templating increases the absorption cross section of SubPc. Since the absorption of SubPc overlaps with that of C_{60} , it's difficult to distinguish whether C_{60} absorption is affected as well. However, despite the increase in absorption, the overall EQE of the templated SubPc OSCs decreases over this wavelength range, suggesting that charge transport or exciton dissociation is affected. The impact of templating on hole transport in SubPc is investigated in the next section.

7.3.3. Effect of Templating on Hole Transport

In order to investigate the effect of templating on hole transport, unipolar hole-only devices were fabricated with ZnPc, ClAlPc and SubPc. To isolate the effect of molecular orientation on hole-mobility, PTCDA or CuI was deposited at the anode interface before the phthalocyanine in one set of devices and also on top of the phthalocyanine in another set of devices. When phthalocyanine is deposited on top of PTCDA or CuI, the molecular orientation of the phthalocyanine is affected due to epitaxial growth. These devices are labeled as PTCDA-Pc or CuI-Pc in Figure 27, Figure 28, Figure 29 and Figure 30. However, when PTCDA or CuI are deposited on top of the phthalocyanine, a change in the molecular orientation of the phthalocyanine should not be expected. These devices are labeled as Pc-PTCDA or Pc-CuI in Figure 27, Figure 28,

Figure 29 and Figure 30. The UV/visible absorption spectra of the unipolar devices are shown in Figure 27. It shows the absorption enhancement of the Pcs when they are deposited on top of the templating material and also proves that when the templating layers are deposited on top of phthalocyanine, there is no enhancement in absorption associated with a flat lying molecular orientation.

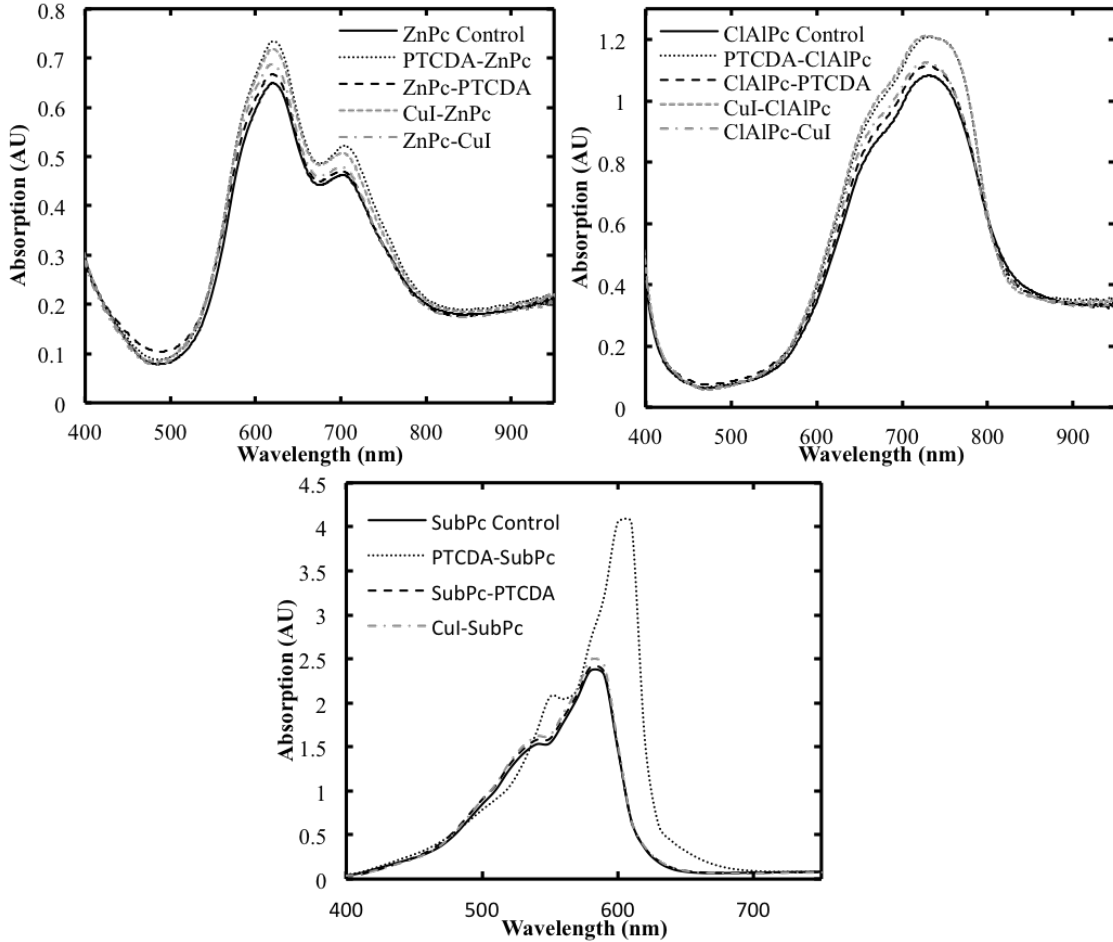


Figure 27: UV/visible absorption spectrum of neat ZnPc and CIAIPc films with PTCDA deposited before and after the phthalocyanines

The hole-mobility was extracted by fitting to space charge limited current equations as given in [31]. The dielectric constant of the organic layers was assumed to be approximately 3 and the trapping factor θ was assumed to be 1 for all devices in order to facilitate easier comparisons. The current density is linearly proportional to both the dielectric constant and trapping factor and keeping them constant for all hole-only devices will allow for the fitting current density to be dictated by the zero-field mobility

and field activation parameter. The extracted zero-field mobilities and field-activation parameters are given in Table 6. SubPc hole-only devices demonstrated very poor conductivity and hence were not fit to the SCLC equations.

Table 6: Zero-field mobilities and field activation parameters of templated and untemplated ZnPc and ClAlPc hole only devices

Donor Material	Templating Layer	Zero-field Mobility (cm^2/Vs)	Field-activation parameter (cm/V) ^{1/2}
ZnPc	Control	1.51E-5	5.67E-4
	PTCDA-ZnPc	6.34E-6	1.35E-3
	ZnPc-PTCDA	1.19E-5	4.98E-4
	CuI-ZnPc	5.84E-6	1.50E-3
	ZnPc-CuI	2.04E-5	6.56E-5
ClAlPc	Control	1.34E-8	5.49E-3
	PTCDA-ClAlPc	5.07E-8	5.03E-3
	ClAlPc-PTCDA	8.24E-9	6.07E-3
	CuI-ClAlPc	4.67E-7	2.53E-3
	ClAlPc-CuI	8.01E-8	4.14E-3

The J-V curve (solid lines) of ZnPc hole-only devices and the corresponding SCLC fits (dotted lines) are shown in Figure 28.

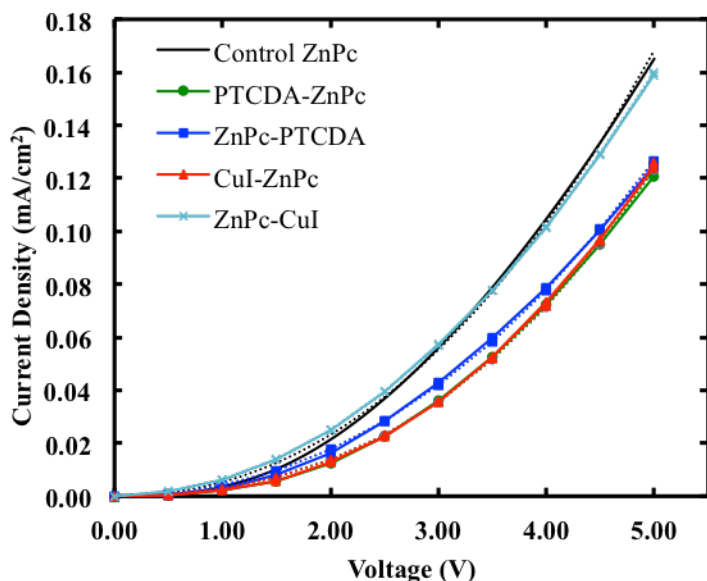


Figure 28: J-V curves (solid lines) and SCLC fits (dotted lines) of ZnPc hole-only devices

Surprisingly, the zero-field hole-mobility of PTCDA and CuI templated ZnPc decreases significantly compared to control ZnPc indicating that the flat-lying molecular orientation degrades hole transport. This is contrary to expectations since a flat-lying molecular orientation on the substrate should improve hole transport in the vertical direction because the π - π stacking direction is along the direction of charge transport. The field activation parameter of the templated ZnPc is higher than controls. The field-activation parameter reflects the dependence of the J-V curve on the electric field. A higher field-activation parameter suggests a greater degree of disorder within the organic films. Since the templated ZnPc devices show a higher field activation parameter, it suggests that there is more disorder in the templated ZnPc. Greater disorder points towards decreased overlap of the π molecular orbitals which in turn, could lead to lower hole mobility.

An examination of samples in which PTCDA is deposited on top of ZnPc reveals that the zero-field hole-mobility degrades as well but not as severely as when the ZnPc is templated. This suggests that the presence of the PTCDA at the interface degrades hole transport aside from the effect of the flat-lying molecular orientation. When CuI is deposited on top of ZnPc, the hole mobility is unaffected indicating that CuI does not

interfere with hole injection. Therefore, improvements in hole transport can be ruled out as the cause for the enhanced J_{sc} and FF seen in templated ZnPc PHJ OSCs.

The analysis presented in the previous section showed that enhancement in absorption only accounts for a portion of the observed J_{sc} increase in templated ZnPc OSCs. The only remaining factor that can explain the observed J_{sc} and FF increase is improvement in exciton dissociation within the device. Previous studies have reported that the efficiency of charge transfer between donor molecules and C_{60} acceptor molecules is enhanced when the donor molecules are face-on with respect to C_{60} . Another factor that can increase exciton dissociation efficiency is a larger contact area between donor molecules and C_{60} , which provides more exciton dissociation sites. A larger contact area can arise due to increased surface roughness of ZnPc caused by templating. The surface roughness of ZnPc is investigated in the next section using atomic force microscopy.

The J-V curve (solid lines) and the corresponding SCLC fits (dotted lines) of the CIAIPc hole-only devices are shown in Figure 29.

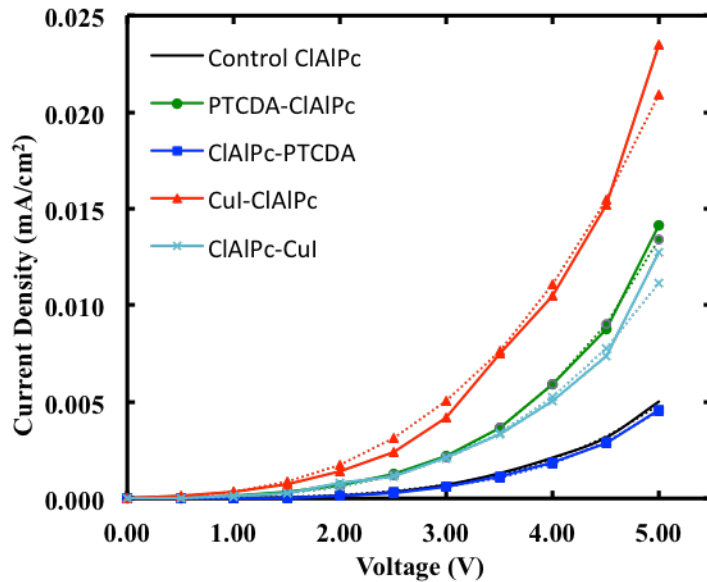


Figure 29: J-V curve (solid lines) and SCLC fits (dotted lines) of the CIAIPc hole-only devices

In contrast to ZnPc, PTCDA and CuI templated CIAIPc devices show a large improvement in hole conductivity. CuI-templated CIAIPc shows a greater increase in hole mobility than PTCDA-templated CIAIPc. This could be because CuI helps hole injection/extraction in the device as seen by the improvement in hole mobility when CuI is deposited on top of CIAIPc. CuI-templated CIAIPc OSCs have much lower series resistance than PTCDA-templated CIAIPc OSCs reflecting the trends seen in the hole-only devices. When PTCDA is deposited on top of CIAIPc, there is no change in hole conductivity indicating that the presence of PTCDA at the CIAIPc interface does not affect hole injection/extraction.

The increase in hole mobility upon templating could be due to decreased π - π stacking distance of the flat-lying CIAIPc molecules. The redshift in the UV/Vis absorption spectrum of templated CIAIPc molecules also support the conclusion that the π - π stacking distance of the CIAIPc molecules is decreased. Furthermore, the field-activation parameter of both PTCDA and CuI templated OSCs decreases upon templating suggesting a greater degree of order in the film. It is interesting to note that the CuI templated CIAIPc has a much lower field activation parameter than PTCDA templated CIAIPc, which suggests that the CuI-templated CIAIPc films are more ordered. This could also contribute to the higher hole mobility of CuI-templated CIAIPc films.

The large increase in hole-mobility upon templating explains the significant decrease in series resistance and corresponding increase in FF seen in templated PHJ OSCs. The increase in FF of templated CIAIPc PHJ OSC is the major factor contributing to their enhanced efficiency.

The analysis presented in the previous section showed that improved charge transport or exciton dissociation must be considered in order to explain the broadband EQE enhancement seen in templated CIAIPc OSCs. The hole-mobility data convincingly shows that improved hole mobility in templated CIAIPc is one of the main reasons for the broadband enhancement in EQE observed. Also, CuI-templated OSCs show EQE comparable to PTCDA-templated OSCs despite having less absorption intensity in the

CIAIPc bands. This could be because CuI-templated CIAIPC OSCs show higher hole mobility than PTCDA-templated OSCs.

In addition to improving hole mobility, templating CIAIPc could also affect its surface roughness and associated CIAIPc/C₆₀ interfacial contact area. The surface roughness of CIAIPc is investigated in the next section using atomic force microscopy.

Figure 30 shows the I-V curve of SubPc hole-only devices. The conductivity of the devices was extremely poor and therefore, was unable to be modeled by the SCLC equations. Comparing the conductivities in the I-V curves, PTCDA-templated SubPc appears to be more conductive than controls. However, when PTCDA is deposited on top of SubPc, the conductivity is decreased suggesting that PTCDA hinders hole injection/extraction in the device. Therefore, the improvement in hole-conductivity can be attributed to the change in the molecular orientation of the SubPc molecules. Regardless of the improvement in hole conductivity for templated-SubPc devices, the FF decreases slightly. This could be due to degraded hole extraction when PTCDA is present at the interface. The analysis in the previous section also showed that the reduction in the J_{sc} was mainly due to a reduction in EQE in the C₆₀ absorption wavelengths. This could indicate that excitons formed in C₆₀ are not dissociated as efficiently when SubPc is templated with PTCDA.

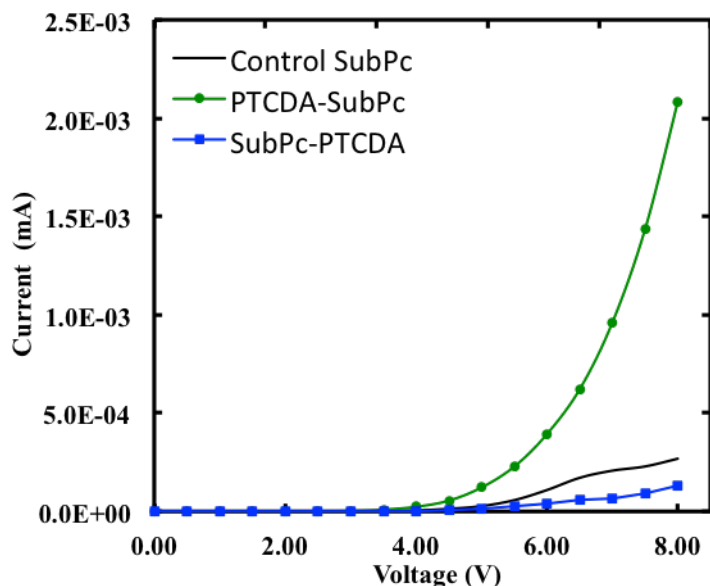


Figure 30: I-V curve of SubPc Hole Only Devices

7.3.4 Effect of Templating on Surface Morphology

In addition to changing the molecular orientation of the phthalocyanines, templating layers also affect their surface roughness. Increased surface roughness results in a larger contact area between C_{60} and phthalocyanine, which promotes increased exciton dissociation. The surface morphology of the templated and control ZnPc and ClAlPc films was analyzed using atomic force microscopy. $2\ \mu\text{m} \times 2\ \mu\text{m}$ scans of the neat ZnPc phthalocyanine films and $1\ \mu\text{m} \times 1\ \mu\text{m}$ scans of the neat ClAlPc phthalocyanine films are shown in Figure 31. The rms roughness values shown in the figure are analyzed for a larger $5\ \mu\text{m} \times 5\ \mu\text{m}$ scan area in order to account for minor variations in topography.

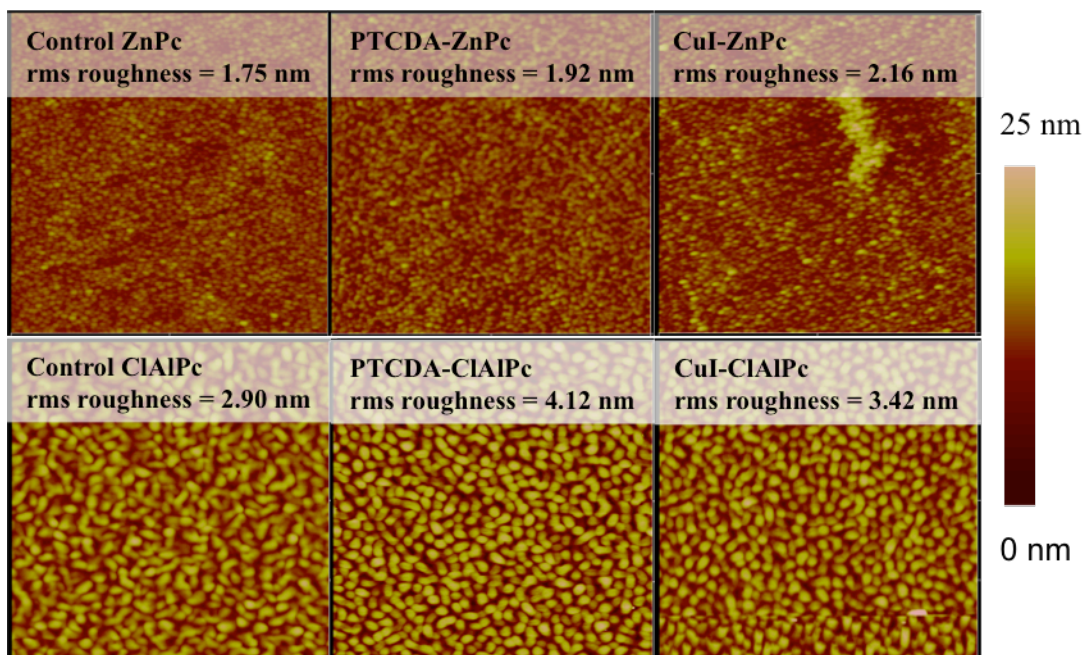


Figure 31: AFM scans of templated and untemplated ZnPc and ClAlPc

For ZnPc, templating with PTCDA increases its surface roughness by 9.7% and templating with CuI increases its surface roughness by 23.4%. The analysis presented in previous sections showed that hole transport does not play a role and improvements in absorption only accounts for part of the J_{sc} and FF enhancement seen in templated ZnPc OSCs. The increase in templated ZnPc surface roughness shows that the ZnPc/ C_{60} contact area increases and therefore improves exciton dissociation in the templated devices. Even though the surface roughness of CuI-templated devices increases by a larger amount than PTCDA-templated devices, the J_{sc} improvement is higher for PTCDA-templated devices. As seen in the previous section, the absorption enhancement is higher for PTCDA-templated devices in the 400 nm – 950 nm wavelength range. This suggests that PTCDA is more effective at re-orienting the ZnPc molecules to the face-on orientation. As reported in literature, improved charge transfer efficiency arising from face-on orientation of ZnPc relative to C_{60} is also responsible for the J_{sc} and FF enhancement observed in the templated OSCs [15]. Since PTCDA is more effective at re-orienting ZnPc, it could also lead to higher charge transfer efficiency, which could explain why PTCDA-templated devices show higher J_{sc} than CuI-templated devices. Finally, the small increase in fill factor in the templated ZnPc OSCs can be attributed to

decreased recombination in the device since shunt resistance increases by 63% and possible enhancements in electron mobility since the series resistance decreases by 31%. The increased shunt resistance decreases the magnitude of the dark current, which also explains the small increase in V_{oc} seen in templated devices.

In CIAIPc OSCs, PTCDA templating increases its surface roughness by 42% and CuI templating increases its surface roughness by 18%. In both cases, the rougher surface increases the CIAIPc/ C_{60} contact area resulting in increased exciton dissociation. PTCDA-templated CIAIPc is rougher than CuI-templated CIAIPc, which suggests that exciton dissociation is enhanced more in PTCDA-templated CIAIPc OSCs than CuI-templated CIAIPc OSCs. However, PTCDA-templated CIAIPc also has lower hole-mobility than CuI-templated CIAIPc. These factors could balance out to result in approximately the same J_{sc} that is observed in the OSCs. Finally, the V_{oc} of CuI-templated CIAIPc OSCs is significantly lower than controls and PTCDA-templated CIAIPc OSCs. The reasons for this decrease could be due to charge accumulation at the ITO/CuI/CIAIPc interface resulting in increased recombination. This is supported by the fact that CuI-templated CIAIPc devices have lower shunt resistance than controls.

7.4 Conclusions

Molecular templating is a promising approach to increase the performance of PHJ OSCs. The magnitude of performance increase from templating depends on the properties of the donor material and the templating layer. Templating layers affect OSCs fabricated with different phthalocyanines in different ways. In ZnPc PHJ OSCs, the efficiency enhancement due to templating is primarily due to improvements in exciton dissociation efficiency. Our study indicates that exciton dissociation efficiency is improved due to increased ZnPc/ C_{60} interfacial contact area. Other studies have shown that flat-lying ZnPc has better charge transfer efficiency compared to edge-on ZnPc. Contrary to expectations, templated ZnPc shows lower hole mobility than control ZnPc suggesting that flat-lying molecular orientation is not beneficial for charge transport in ZnPc PHJ OSCs. In CIAIPc PHJ OSCs, the efficiency enhancement is due to

improvements in both exciton dissociation and charge transport. The exciton dissociation is improved due to increased interfacial contact area. Charge transport is improved due to a lower π - π distance between templated ClAlPc molecules. Finally, in SubPc PHJ OSCs, templating improves hole transport but lowers the overall performance of the OSCs due to reduced exciton dissociation, mainly of the excitons formed in C₆₀. The cause for the reduced exciton dissociation is unclear.

PTCDA-templated and CuI-templated OSCs show different behavior for the same phthalocyanine material. For ZnPc, PTCDA is a more effective templating layer. It reorients ZnPc molecules to a larger degree compared to CuI leading to better absorption and exciton dissociation. Despite CuI-templated ZnPc having a higher surface roughness than PTCDA-templated ZnPc, CuI-templated OSCs do not result have higher performance than PTCDA-templated OSCs. For ClAlPc, CuI templating improves hole conductivity to a greater extent than PTCDA templating. As a result, the series resistance of CuI-templated OSCs is much lower than PTCDA-templated OSCs. However, the ITO/CuI/ClAlPc interface shows higher recombination of excitons and charge carriers resulting in lower V_{oc} and shunt resistance, ultimately limiting the performance of CuI-templated ClAlPc OSCs. PTCDA-templated ClAlPc is much rougher than CuI-templated ClAlPc, which results in better exciton dissociation in PTCDA-templated OSCs. The improved charge transport in CuI-templated ClAlPc OSCs balances out the improved exciton dissociation in PTCDA-templated ClAlPc OSCs leading to similar J_{sc} and FF. Finally, SubPc is only templated PTCDA and is unaffected by CuI. Our results show that the interaction between phthalocyanines and templating layers are unique to each combination and molecular templating warrants further study to realize its full potential as an avenue for OSC performance enhancement.

Chapter 8 – Influence of the Donor Material on the Degradation Behavior of C60-Based Planar Heterojunction Organic Solar Cells

Chapter Summary

The limited lifetime of small-molecule organic solar cells (OSCs) is a major barrier that stands in the way of their commercialization. Photo-oxidation of C60 is one of the main mechanisms that is responsible for the lower lifetimes small-molecule OSCs. However, there are no studies in literature that examines how the donor material affects the extent of C60 photo-oxidation in planar heterojunction (PHJ) OSCs. In this study, we first investigate the degradation of Schottky-type C60-only OSCs and then compare the degradation behavior of PHJ OSCs made with ZnPc, ClInPc and SubPc donors. We also study the influence of molecular orientation of ZnPc and ClInPc on the degradation behavior of PHJ OSCs by using PTCDA or CuI templating layers to template the phthalocyanines. This chapter addresses the fifth and final objective of this research work.

Photo-oxidation of C60 results in the formation of lower bandgap impurities that act as trap states leading to increased recombination. In C60 Schottky OSCs, this results in a drop in photocurrent generation from the C60 aggregates. Surprisingly, the degradation behavior of all three PHJ OSCs is dominated by C60 photo-oxidation but to different extents depending on the phthalocyanine used. Our results suggest that the extent of C60 photo-oxidation is primarily influenced by the surface roughness of the C60 layer, which in-turn is dictated by the morphology of the donor material. The molecular orientation of the phthalocyanine donors has only a minor impact on the aging behavior of PHJ OSCs.

8.1 Introduction

One of the main barriers towards the commercialization of small molecule OSCs is their limited lifetime [1-6]. The following device structure is most often used in literature to study the performance and lifetime of small molecule OSCs: ITO/Anode buffer layer/Active layer/Cathode buffer layer/Cathode metal. Anode buffer layers (such as MoO₃ and other transition metal oxides) aid in extraction of holes whereas the cathode buffer layers (such as BCP, Alq₃, BCP:C60) aid in the extraction of electrons, reduce exciton quenching at the cathode and protect the active layers from damage during cathode deposition [7-11]. The active layer of these OSCs is composed of either a planar heterojunction or a bulk heterojunction. In a planar heterojunction (PHJ) OSC, neat films of donor and acceptor materials are deposited on top of each other. In a bulk heterojunction (BHJ) OSC, the donor and acceptor materials are molecularly mixed in a single layer.

The performance of both PHJ and BHJ OSCs degrades under illumination in atmospheric as well as inert conditions. The mechanisms responsible for the loss in performance can be grouped into two categories – i) degradation of the electrodes and interfacial layers and ii) degradation of the donor and acceptor materials in the active layer [3,9]. Extensive studies in literature have shown that the use of anode and cathode buffer layers with good thermal stability and resistance to oxygen and moisture penetration can increase the lifetime of small-molecule OSCs [3,7,9,11–15]. However, only relatively small body of work has investigated the degradation of small molecule donor and acceptor materials in the active layer.

While numerous donor materials have been reported in literature for use in the active layer, most high-efficiency small molecule OSCs still use fullerenes, such as C60 and C70, as the acceptor material. One of the most common degradation mechanisms of fullerenes is photo-oxidation in the presence of oxygen, which results in the formation of recombination centers, which quench excitons and lower electron mobility in the material [16-19]. Exposure to atmospheric conditions and the presence oxygen impurities in the

interfacial layers and donor materials are some of the ways that the C60 layer can come in contact with oxygen. Studies in literature have already shown using buffer layers with lower oxygen and moisture penetration can increase lifetime significantly by reducing the photo-oxidation of C60. However, there are no studies to date that examine the influence of the donor material in affecting the photo-oxidation of C60 and the lifetime of the OSC. Even though studies in literature use a wide variety of donor materials, different aging conditions, device architectures and buffer layers of the OSCs make cross comparisons difficult or invalid.

In this study, we conduct a systematic investigation into how the donor material affects the photo-degradation of C60. First, we study the degradation of Schottky-type C60-only OSCs in order to establish the degradation behavior of C60 without the presence of any donor material. In these Schottky-OSCs, C60 serves as both the exciton generation and charge transport material. They demonstrate relatively high V_{oc} and J_{sc} due to interfacial charge transfer and band bending at the $MoO_3/C60$ interface [20, 21]. Then, we move on to studying the degradation of phthalocyanine/C60 PHJ OSCs using ZnPc, ClInPc and SubPc as the donor materials. We chose these three phthalocyanines due to their morphological differences. The surface roughness, crystallinity and molecular orientation of the donor material is known to affect the morphology of C60 deposited on top [22-24]. SubPc is known to be an amorphous material that forms smooth films with random molecular orientation. ZnPc and ClInPc are polycrystalline materials with a higher surface roughness and crystallinity than SubPc. ZnPc molecules orient themselves with their planes vertical to the substrate whereas ClInPc molecules have a mean tilt angle of approximately 60° to 70° from the vertical [25-27]. The molecular orientations of ZnPc and ClInPc can also be modified through the use of templating layers such as PTCDA or CuI. By studying the degradation behavior of these PHJ OSCs, insight into how the morphology of C60 affects its degradation behavior can be obtained. In all cases, we use the same anode and cathode buffer layers to ensure that cross comparisons between the devices is justifiable.

8.2 Experimental Methods

The general fabrication procedure described in Section 4.1 was used to fabricate the OSCs used in this study. PHJ OSCs were fabricated with the structure: ITO/MoO₃ (7 nm)/phthalocyanine donor/C60 (35 nm)/BCP (8 nm)/Al (100 nm). The following donor thicknesses were used because it resulted in optimum PHJ OSC performance: ZnPc – 15 nm, ClInPc – 20 nm and SubPc 7 nm. C60 Schottky OSCs were fabricated with the same structure but without the donor material. Templated PHJ OSCs were also fabricated by depositing a templating layer before the phthalocyanine donor material. 2 nm of PTCDA or 2 nm of CuI were used as the templating layer. Optimum performance with PTCDA was obtained when it was deposited on top of 7 nm MoO₃ whereas optimum performance with CuI was obtained when it was deposited directly on ITO without MoO₃. 8 nm of BCP was used as an exciton-blocking layer. 100 nm of aluminum was deposited as the cathode. For AFM samples, BCP and Al were not used.

The OSCs were aged under a halogen lamp at 120 mW/cm² light intensity. An inert atmosphere was maintained during aging by constantly flowing nitrogen through the enclosure containing the OSCs. The temperature of the OSCs during aging was measured to be approximately 30⁰C using a thermocouple taped to the backside of the glass substrate. External quantum efficiency (EQE) and UV/visible absorption spectra of the OSCs were measured when the OSCs were fresh and at the conclusion of aging. PV parameters were measured regularly and aging was halted once the efficiency of the OSCs dropped below 80% of the initial value.

The PV parameters, EQE spectra, UV/Visible absorption spectra and atomic force microscopy images were obtained following the procedures described in Section 4.2.

8.3 Results and Discussion

8.3.1 Degradation of C60 Schottky OSCs

Figure 32 shows the normalized PV parameters of a C60 Schottky OSC and ZnPc, ClInPc and SubPc PHJ OSCs as a function of aging time. The PV parameters at time 0 for these OSCs are shown in the appendix in Table A8.

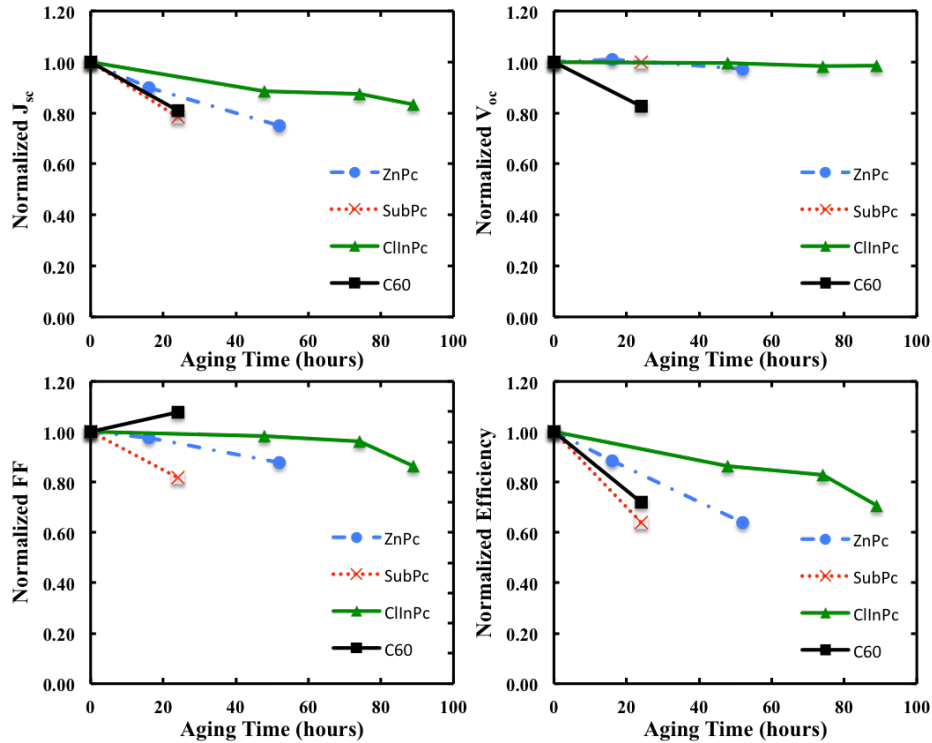


Figure 32: PV parameters of ZnPc, SubPc and ClInPc PHJ OSCs as a function of aging time

During aging, the J_{sc} of the C60 Schottky OSC drops to 81% and the V_{oc} drops to 83% of their initial value. The fill factor shows a small increase of approximately 8% from its initial value. As a result, the overall efficiency of the OSC drops to 72% of its initial value.

In order to further investigate the loss in J_{sc} , the external quantum efficiency (EQE) of the OSC was measured before and after aging. The EQE spectrum is shown in Figure 33. It can be seen that the loss in EQE between the fresh and the aged samples occurs mainly in the wavelength range of $\lambda = 420 - 530$ nm. Neat films of C60 contain

C60 aggregates (which absorb in the $\lambda = 400 \text{ nm} - 550 \text{ nm}$ wavelength range) and C60 monomers (which absorb in the $\lambda = 325 - 400 \text{ nm}$ wavelength range) [28-30]. The decrease in EQE is primarily in the C60 aggregate band, which suggests that the excitons formed in the aggregates contribute less to the photocurrent upon aging.

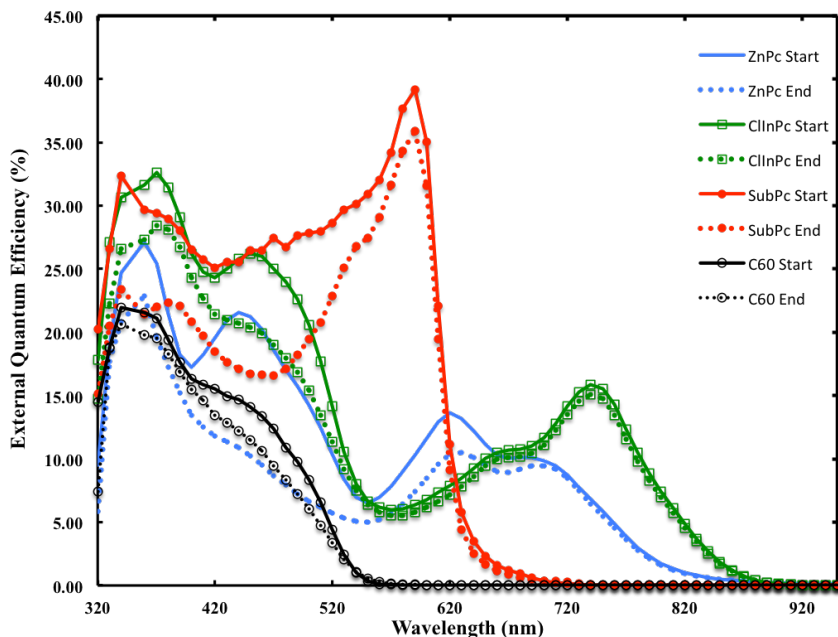


Figure 33: External quantum efficiency spectra of fresh and aged samples of C60 only OSCs, ZnPc PHJ OSCs, ClInPc PHJ OSCs and SubPc PHJ OSCs.

The UV/Vis absorption spectrum of the C60 Schottky OSC was also measured before and after aging in order to determine whether the decrease in the EQE in the C60 aggregate band corresponds to a decrease in absorption over the same wavelength range. The absorption spectra are shown in Figure 34. The absorption bands of the aged C60 Schottky OSC are slightly broader than the fresh OSCs but there is no significant difference in the absorption intensity of the aggregate band. This suggests that the aging results in the formation of impurities in C60 with a lower band-gap but no differences in extent of aggregation.

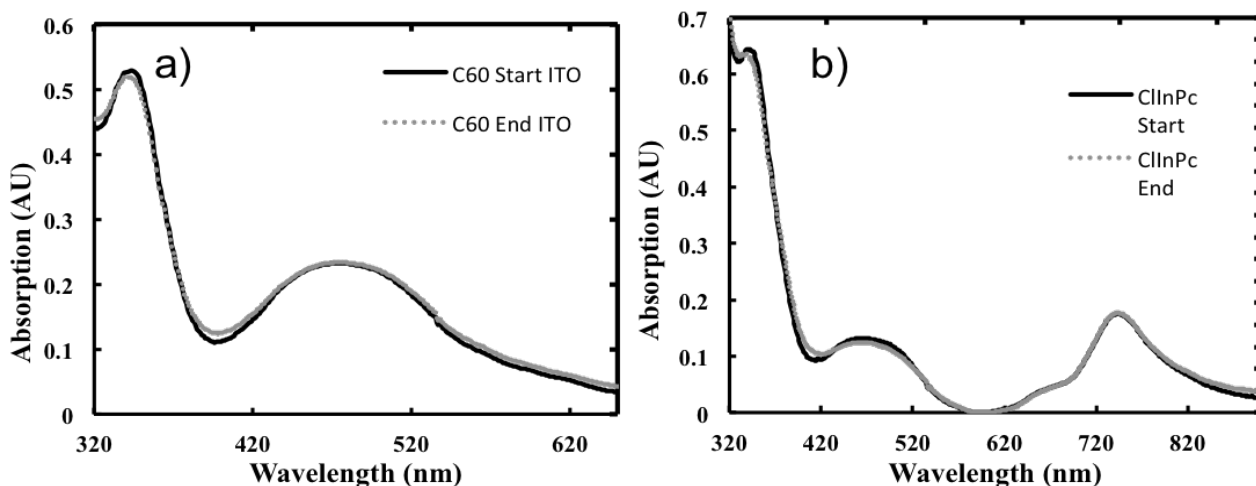


Figure 34: a) Absorption of C60 only OSC before and after aging and b) Absorption of ClInPc/C60 PHJ OSC before and after aging

In order to verify whether the aggregation of C60 is affected upon aging, atomic force microscopy images of C60 Schottky films before and after aging were compared. The initial rms surface roughness of the C60 Schottky OSC was 1.12 nm. Only a 5.2% increase in rms surface roughness was observed in the aged samples (images in supplemental information), which supports the hypothesis that the C60 aggregation is not affected by aging.

Considering the EQE, UV/Vis and AFM data together, it can be concluded that the reduction in J_{sc} of the C60 Schottky OSCs upon aging is likely due to the formation of lower band-gap impurities. Previous studies have shown that C60 reacts readily with molecular oxygen to form C60=O which is then subsequently broken down to smaller fullerene molecules such as C58 [18]. C58 has been reported to have a bandgap of 1.2 eV, which is smaller than the C60 bandgap of 1.7 eV [31,32]. Due to the large difference in bandgaps between C58 and C60, C58 acts as trap states in C60 that increases recombination of excitons and therefore reduces the photocurrent of the OSC.

Furthermore, the V_{oc} of the aged C60 Schottky OSCs is lower than that of the fresh OSCs. Since in these devices, the V_{oc} is around 1.1V – 1.3V due to interfacial charge transfer and the formation of a band-bending region at the MoO₃/C60 interface

[32], it is possible that the charge transfer is reduced with the formation of C58 after aging resulting in a lower V_{oc} .

8.3.2 Degradation of Phthalocyanine/C60 PHJ OSCs

During the aging of PHJ OSCs, only the J_{sc} and FF degrade whereas, in contrast to the C60 Schottky OSCs, the V_{oc} stays constant. The extent of J_{sc} and FF degradation depends upon the donor material used in the OSC. ClInPc PHJ OSCs are the most stable showing only a 11% loss in J_{sc} and FF over 89 hours of aging. SubPc PHJ OSCs are the least stable showing a 22% loss in J_{sc} and 18% loss in FF within 24 hours of aging. ZnPc PHJ OSCs show intermediate degradation losing 25% J_{sc} and 12% FF over 52 hours of aging. The reason for the variation in degradation behavior could be due to differences in the degradation behavior of the phthalocyanines or the C60 deposited on top of the phthalocyanines. Since the buffer layers are the same for all these devices, the contribution of the buffer layer to the degradation is expected to be similar for all the OSCs.

In order to further investigate the loss in J_{sc} for the three OSCs, the EQE spectra of the devices before and after aging were measured and shown in Figure 33. For all three PHJ OSCs, the major degradation is in the C60 aggregate band in the wavelength range of $\lambda = 400 \text{ nm} - 550 \text{ nm}$. The loss in the EQE in the phthalocyanine band is relatively small compared to the loss in the C60 aggregate bands. This is a surprising finding because it suggests the differences in lifetime for these OSCs are mainly due to the differences in C60 degradation. The UV/Vis absorption of fresh and aged phthalocyanine PHJ OSCs was measured in order to determine whether the EQE loss in the C60 aggregate band corresponds to changes in the absorption spectrum. The UV/Vis absorption spectra of fresh and aged ClInPc PHJ OSCs are shown in Figure 34(b). Similar to the C60 Schottky OSC, the C60 aggregate absorption band is broader in the aged PHJ OSCs. However, there is relatively little change in the absorption of the ClInPc. Similar trends were observed for the ZnPc and SubPc OSCs (absorption data in supplementary information). These observations suggest that the primary cause of J_{sc} loss

in PHJ OSCs during aging is, once again, primarily due to the degradation of C60. The loss in C60 aggregate band EQE can be attributed to the formation of lower bandgap impurities such as C58, which act as trap states causing increased recombination and lower J_{sc} , similar to the C60 Schottky OSC.

The FF loss upon aging for the phthalocyanine/C60 OSCs follows the same trend as the J_{sc} loss for the three donor materials. SubPc PHJ OSCs show the highest FF loss followed by ZnPc PHJ OSCs. ClInPc PHJ OSCs show the lowest FF loss. For all three materials, the loss in FF is due to an increase in series resistance with very little to no change in shunt resistance. Increasing series resistance suggests a decrease in charge mobility in the OSC. From the EQE and UV/Vis data, it was determined that the majority of the J_{sc} loss is due to C60 degradation. Therefore, it is reasonable to assume that the increase in series resistance is due to decreased electron mobility in the aged C60 layers [16].

Finally, the V_{oc} of all three PHJ OSCs shows no change upon aging. This suggests that the $HOMO_{donor}$ - $LUMO_{acceptor}$ energy level offset is unaffected at the donor/acceptor interface. Previous reports have shown that exposure of PHJ OSCs to molecular oxygen close to the donor/acceptor interface leads to a V_{oc} loss upon aging [33]. However, this loss is not seen if molecular oxygen is introduced further away from the donor/acceptor interface [33]. Therefore, the loss in J_{sc} and FF observed in the three PHJ OSCs in this study can be attributed to degradation of C60 away from the donor/acceptor interface. This is likely due to the penetration of moisture and oxygen from the Al electrode [3,12]. Furthermore, since the V_{oc} is not affected for any of the three PHJs in this study, it can be concluded that the energetic difference between the donor/acceptor is not a factor in the aging of the PHJ OSCs.

8.3.3 Influence of C60 Morphology on Degradation Behavior

In the previous section, it was established that only C60 degradation is responsible for the differences in degradation behavior of phthalocyanine/C60 OSCs. In addition, it was also established that the energetic differences at the donor/acceptor

interface could be ruled out as one of the contributors to the differences in degradation behavior. Therefore, there can only be one other major factor that can explain these interesting observations - the different morphology of C60 on the three phthalocyanines. There are two factors that affect the morphology of C60 when it is deposited on top of a phthalocyanine donor material – i) the crystallinity and surface roughness of the phthalocyanine and ii) the molecular orientation of the phthalocyanine.

In order to determine how the morphology of C60 changes when deposited on top of different phthalocyanines, AFM images of C60 deposited on top of ClInPc and SubPc were obtained. The scan area of the AFM images was 5 μm x 5 μm . ClInPc and SubPc were chosen because they represent the extreme ends of the degradation in the devices studied. ClInPc OSCs are the most stable whereas SubPc OSCs are the least stable. The AFM images are shown in Figure 35. Visually, the C60 layer on top of ClInPc is much rougher than the C60 layer on top of SubPc. RMS roughness analysis shows that ClInPc/C60 has a roughness of 2.81 nm whereas SubPc/C60 has a roughness of 1.23 nm. The higher surface roughness of ClInPc/C60 indicates that the C60 is more crystalline when deposited on top of ClInPc than when deposited on SubPc. SubPc, which has amorphous morphology, forms smooth films with low surface roughness [34]. When C60 is deposited on SubPc, the resulting C60 film is also smooth. The surface roughness of C60 Schottky OSCs is similar to the surface roughness of SubPc/C60. ClInPc and ZnPc, meanwhile, are polycrystalline and form granulated films with a high surface roughness. As a result, C60 deposited on top of ClInPc has a higher surface roughness and larger grain size than SubPc films.

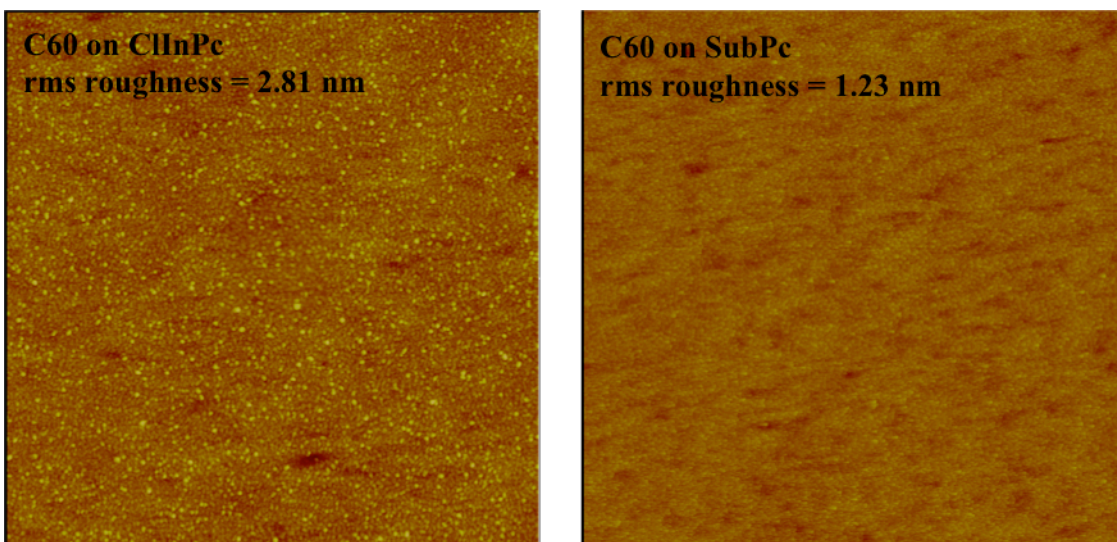


Figure 35: AFM Images of C60 on top of ClInPc and SubPc

The large differences in surface roughness and crystallinity of C60 when deposited on top of different phthalocyanines could be a major factor in influencing the aging behavior of the phthalocyanine/C60 PHJ OSCs. Greater aggregation and crystallinity of C60, such as when deposited on ClInPc, could lead to lower degradation compared to smoother films, such as when deposited on SubPc. Furthermore, C60 Schottky OSCs and SubPc/C60 PHJ OSCs show similar degradation behavior such as rapid degradation of J_{sc} within the first 24 hours aging. They also have similar surface roughness of around 1.2 nm rms. This suggests that their degradation behavior could be similar due to the smoothness of their C60 in both cases.

In addition to the crystallinity and surface roughness, changes in molecular orientation of ClInPc and ZnPc could also affect the morphology of the C60 on top. When deposited on weakly interacting materials such as ITO or MoO₃, ClInPc has a mean tilt angle of ~60-70° and ZnPc has a mean tilt angle of 0°. When ClInPc or ZnPc are deposited on PTCDA or CuI templating layers, their mean tilt angle increases to near 90° so that the majority of the molecules lie parallel to the substrate. The resulting change in the molecular orientation can affect the packing of C60 molecules deposited on top of the phthalocyanine.

In order to determine whether the molecular orientation of the phthalocyanine may play a significant role in affecting the degradation behavior of PHJ OSCs, we fabricated and aged PTCDA and CuI templated ZnPc and ClInPc PHJ OSCs under similar conditions to non-templated control samples. SubPc OSCs were not included in this experiment because SubPc does not demonstrate significant change in molecular orientation when deposited on PTCDA or CuI. The normalized PV parameters of templated ZnPc PHJ OSCs as a function of aging time is shown in Figure 36. The PV parameters of these OSCs at time-zero are given in the appendix in Table A9.

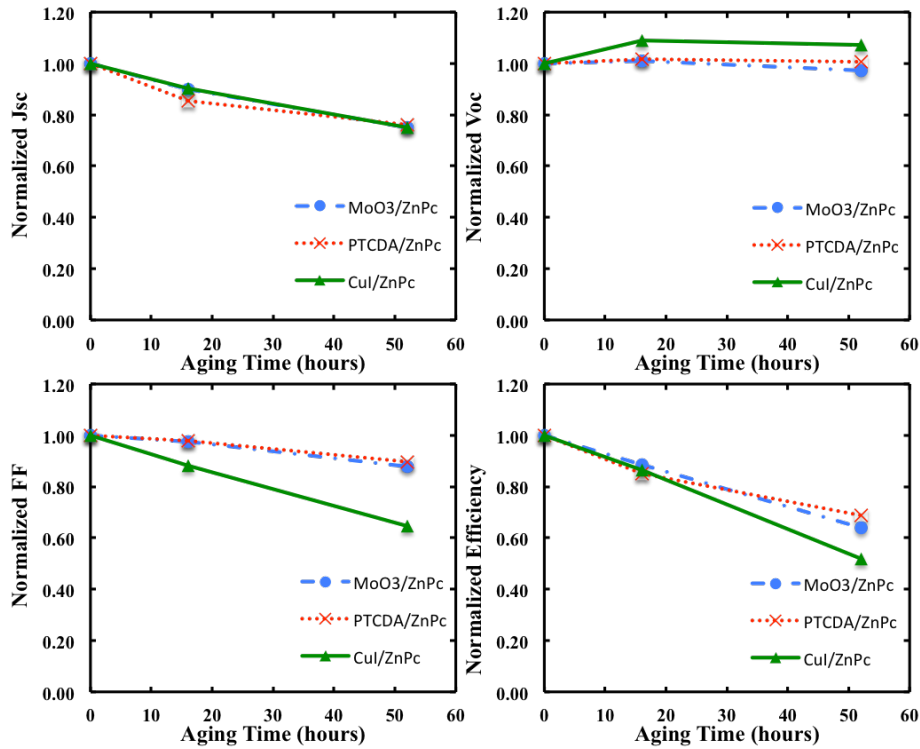


Figure 36: PV parameters of templated and non-templated ZnPc PHJ OSCs as a function of aging time

For ZnPc PHJ OSCs, the J_{sc} degradation of PTCDA and CuI templated and non-templated OSCs is similar. However, the FF of CuI templated ZnPc PHJ OSCs degrades much faster than non-templated or PTCDA templated PHJ OSCs. The degradation of efficiency is similar for PTCDA-templated and non-templated ZnPc PHJ OSCs but due to the rapid FF deterioration, CuI templated ZnPc PHJ OSCs are the less stable. The V_{oc} of templated and non-templated OSCs show no change upon aging.

The normalized PV parameters of ClInPc PHJ OSCs as a function of aging time are shown in Figure 37. The time-zero PV performance of these OSCs are shown in the appendix in Table A10.

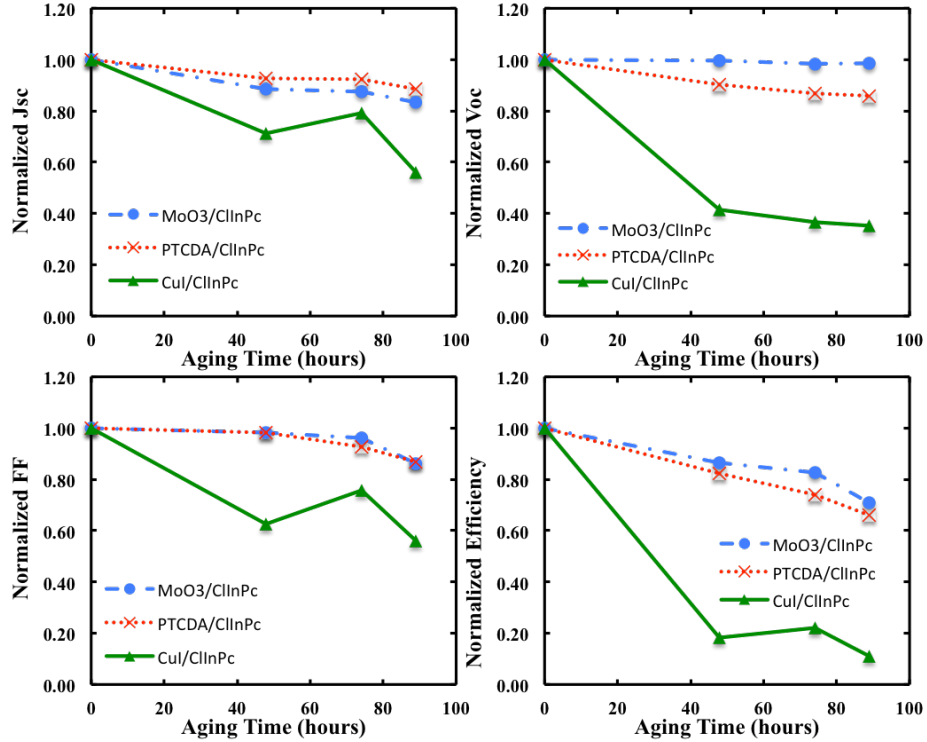


Figure 37: PV parameters of templated and non-templated ClInPc PHJ OSCs as a function of aging time

For ClInPc PHJ OSCs, PTCDA templated OSCs show greater J_{sc} stability but larger V_{oc} degradation than non-templated OSCs. Due to the increased V_{oc} degradation, the efficiency of PTCDA templated ClInPc PHJ OSCs degrades faster than non-templated OSCs. CuI-templated ClInPc PHJ OSCs show rapid degradation of all PV parameters within a short time indicating that the CuI/ClInPc interface is unstable.

In order to further examine the differences in J_{sc} degradation between the templated and non-templated OSCs, the external quantum efficiency spectra of the fresh and aged OSCs with and without templating layers were measured. For templated and non-templated ZnPc and ClInPc OSCs, the majority of the degradation still occurs in the C60 aggregate band as observed in the previous cases. The only exception is the CuI/ClInPc device where the EQE degrades over the entire spectrum, suggesting the

phenomenon arises from the instability of the CuI/ClInPc interface. The percent difference between the EQE of fresh and aged samples was calculated at the maximum absorption wavelength of the C60 aggregates (440 nm), ClInPc (740 nm) and ZnPc (630 nm). The percent differences are shown in Table 7. The full EQE spectra are available in the supplemental information.

For ClInPc PHJ OSCs, PTCDA templating reduces the EQE degradation for both C60 and ClInPc by a small margin. PTCDA/ClInPc/C60 layers are also 12% rougher than non-templated ClInPc/C60 layers, which again suggests that there is a correlation between an increase in roughness of C60 and higher OSC stability. Interestingly, for ZnPc PHJ OSCs, templating with PTCDA and CuI increases the degradation of the C60 EQE but reduces the degradation of the ZnPc EQE. Templating could affect the aging behavior by altering the penetration and reaction rates of oxygen from the cathode through the C60 layers due to small differences in the C60 morphology.

For both materials, the differences in EQE upon aging due to templating are small compared to the differences in aging behavior between the phthalocyanine materials. One of the reasons for this could be the fact that there is only a small difference in surface roughness between templated and non-templated phthalocyanine/C60 layers. For ClInPc, the surface roughness only increases by 12% when templated with PTCDA. Whereas non-templated ClInPc/C60 layers are 56% rougher than SubPc/C60 layers.

Table 7: EQE percent differences between fresh and aged samples for templated and control ClInPc and ZnPc PHJ OSCs

Donor Material	Peak Wavelength	Control (MoO ₃ /Pc)	PTCDA templated (MoO ₃ /PTCDA/Pc)	CuI templated (CuI/Pc)
ClInPc	C60 (440 nm)	-22.3	-18.4	-60.4
	ClInPc (740 nm)	-4.9	-2.6	-49.5
ZnPc	C60 (440 nm)	-49.4	-52.9	-59.3
	ZnPc (630 nm)	-20.4	-14.9	-13.1

8.4 Conclusions

One of the leading causes of degradation of small molecule OSCs is the formation of trap states in C60 due to photo-oxidation in the presence of oxygen. In a PHJ OSC, we've found that the extent of C60 degradation due to photo-oxidation is dictated by the C60 morphology, which in turn is influenced by the donor material used. The surface roughness, crystallinity and molecular orientation of the donor material are mimicked by the C60 when deposited on top. Our results suggest a correlation between C60 roughness and degradation – rougher films are less prone to degradation than smoother films. In the rough C60 case, the adhesion of the C60 to the cathode could be higher, which in turn allows for lower oxygen penetration. Recent high efficiency device architectures for small molecule OSCs are composed of more than 90% fullerene and it is not possible to directly control the morphology to minimize the effects of degradation. Therefore, the development of buffer layers with high resistance to oxygen penetration is crucial to prevent the degradation of C60 and extend the lifetime of small-molecule OSCs.

Chapter 9 – Conclusions and Future Work

The first objective of this research work was to examine the role of the donor-acceptor mixing ratio in influencing the morphology and performance of bulk heterojunction organic solar cells. The findings established in Chapter 5 have shown that the high short circuit current (J_{sc}) seen in BHJ OSCs with low donor concentrations, so-called Schottky-junction OSCs, arise primarily from photocurrent contributions from charge-transfer intermolecular states in C_{60} aggregates. These aggregates absorb light at 400-600nm and are thus well matched to the solar spectrum. The presence of the donor molecules is shown to be necessary for the dissociation of the C_{60} aggregate excitons, which ultimately allows for enhanced photocurrents. Increasing the donor concentration beyond a certain threshold hinders C_{60} aggregate formation and thus removes its contribution to photocurrent completely. The second objective of this research work was to examine the role of the donor-acceptor mixing ratio and associated morphological changes in all organic solar cell device architectures. Building on the insights in Chapter 5, the findings of Chapter 6 show that the BHJ/acceptor architecture, comprising a BHJ layer with high C_{60} content followed by a neat C_{60} layer, generates OSCs with the highest performance by balancing charge generation with charge collection. The performance of other device architectures, such as the planar mixed heterojunction (PMHJ), planar heterojunction (PHJ), bulk heterojunction (BHJ) and donor/BHJ, is largely limited by hole transport, with associated hole accumulation and space charge effects. Together, the results presented in Chapter 5 and 6 have thoroughly examined the role of the donor-acceptor mixing ratio in phthalocyanine/ C_{60} OSCs and how the associated morphological changes affect device performance, answering a hitherto unexamined question in literature. In general, the significance of these results is in highlighting the importance of fullerene aggregation in influencing the performance of small-molecule OSCs. Future work should examine whether favorable fullerene aggregation can be increased using external treatments such as substrate heating during deposition and solvent annealing and

also whether new donor molecules can be identified that promote fullerene aggregation while retaining excellent exciton dissociation and hole transport properties.

The molecular orientation of organic semiconductors in an OSC affects all fundamental OSC processes – absorption, exciton dissociation and charge transport. The effect of molecular orientation on the device physics of OSCs is a subject of recent and intense interest in literature. Molecular orientation can be controlled in planar heterojunction (PHJ) OSCs by using templating layers such as PTCDA and CuI. The third objective of this research work is to determine the effect of molecular templating on hole mobility of phthalocyanine/C60 planar heterojunction OSCs and examine associated changes in device physics. In addition, the fourth objective of this research work is to compare the templating efficacy of the two common templating layers, CuI and PTCDA, across a wider variety of phthalocyanine donor materials. The findings in Chapter 7 show that the interaction between different phthalocyanines and templating layers are unique to each combination and affect different aspects of OSC device physics. For example, the performance improvements in templated ZnPc OSCs are mainly due to improved exciton dissociation in the device and contrary to expectations, templating reduces charge mobility in ZnPc. In contrast to ZnPc, the performance improvements in templated ClAlPc OSCs are due to improvements in both exciton dissociation efficiency and charge transport. Finally, SubPc is only templated by PTCDA and is unaffected by CuI. However, PTCDA templated SubPc devices show reduced exciton dissociation and hence lower performance over controls. These findings are significant because they show that the hole mobility of phthalocyanines is not necessarily improved by templating, which runs contrary to expectations. Templating layers affect the molecular orientation as well as the aggregation, crystallinity and packing of the phthalocyanine films. Even if molecular orientation is favorable for hole transport, a greater degree of disorder in the templating phthalocyanine films can result in lower hole mobility. Future work should examine whether the molecular orientation a bulk heterojunction can be controlled as well. To this end, potential approaches include molecular modification of donor materials, deposition on a heated substrate and deposition of bulk heterojunctions on templated neat layers of organic materials.

The final objective of this research work is to investigate the degradation behavior of templated phthalocyanine/C60 planar heterojunction OSCs. Chapter 8 addresses this objective by studying the degradation of templated and untemplated ZnPc, ClInPc and SubPc PHJ OSCs. One of the leading causes of degradation of small molecule OSCs is the formation of trap states in C60 due to photo-oxidation in the presence of oxygen. In the PHJ OSCs, our results show that the extent of C60 degradation due to photo-oxidation is dictated by the C60 morphology, which in turn is influenced by the donor material used. The surface roughness, crystallinity and molecular orientation of the donor material are mimicked by the C60 when deposited on top. Our results suggest a correlation between C60 roughness and degradation – rougher films are less prone to degradation than smoother films. However, the effect of templating the ZnPc and ClInPc donors with PTCDA or CuI has little effect on the overall stability of the PHJ OSCs, indicating that molecular orientation is not an important factor in determining the stability of PHJ OSCs. This study is significant because it is the first to show that the photo-oxidation of C60 in a PHJ OSC is affected by C60 morphology, which in turn is determined by the morphology of the donor material used. Future work examining the degradation behavior of OSCs should focus on identifying cathode buffer materials with low oxygen and moisture penetration rates in hopes of reducing the photo-oxidation of C60.

Letters of Copyright Permission

Permission for Figure 1, Figure 4 and Figure 9:



RightsLink®

Home

Create Account

Help



Title: Organic Semiconductors and their Applications in Photovoltaic Devices
Author: Jason D. Myers, Jiangeng Xue
Publication: Journal of Macromolecular Science Part C -- Polymer Reviews
Publisher: Taylor & Francis
Date: Jan 1, 2012
Copyright © 2012 Taylor & Francis

LOGIN

If you're a **copyright.com user**, you can login to RightsLink using your copyright.com credentials. Already a **RightsLink user** or want to [learn more?](#)

Thesis/Dissertation Reuse Request

Taylor & Francis is pleased to offer reuses of its content for a thesis or dissertation free of charge contingent on resubmission of permission request if work is published.

BACK

CLOSE WINDOW

Copyright © 2016 Copyright Clearance Center, Inc. All Rights Reserved. [Privacy statement](#). [Terms and Conditions](#). Comments? We would like to hear from you. E-mail us at customercare@copyright.com

Permission for Figure 5 and Figure 7:

AIP PUBLISHING LLC LICENSE
TERMS AND CONDITIONS

Jan 05, 2016

All payments must be made in full to CCC. For payment instructions, please see information listed at the bottom of this form.

License Number	3782800666959
Order Date	Jan 05, 2016
Publisher	AIP Publishing LLC
Publication	Applied Physics Letters
Article Title	Structural templating effects in molecular heterostructures grown by organic molecular-beam deposition
Author	S. Heutz,R. Cloots,T. S. Jones
Online Publication Date	Dec 11, 2000
Volume number	77
Issue number	24
Type of Use	Thesis/Dissertation
Requestor type	Student

Format	Print and electronic
Portion	Figure/Table
Number of figures/tables	2
Title of your thesis / dissertation	The Influence of Morphology and Molecular Orientation on the Efficiency and Lifetime of Organic Solar Cells
Expected completion date	Jan 2016
Estimated size (number of pages)	150
Total	0.00 USD
Terms and Conditions	
AIP Publishing LLC	-- Terms and Conditions: Permissions Uses

AIP Publishing LLC ("AIPP") hereby grants to you the non-exclusive right and license to use and/or distribute the Material according to the use specified in your order, on a one-time basis, for the specified term, with a maximum distribution equal to the number that you have ordered. Any links or other content accompanying the Material are not the subject of this license.

1. You agree to include the following copyright and permission notice with the reproduction of the Material: "Reprinted with permission from [FULL CITATION]. Copyright [PUBLICATION YEAR], AIP Publishing LLC." For an article, the copyright and permission notice must be printed on the first page of the article or book chapter. For photographs, covers, or tables, the copyright and permission notice may appear with the Material, in a footnote, or in the reference list.
2. If you have licensed reuse of a figure, photograph, cover, or table, it is your responsibility to ensure that the material is original to AIPP and does not contain the copyright of another entity, and that the copyright notice of the figure, photograph, cover, or table does not indicate that it was reprinted by AIPP, with permission, from another source. Under no circumstances does AIPP, purport or intend to grant permission to reuse material to which it does not hold copyright.
3. You may not alter or modify the Material in any manner. You may translate the Material into another language only if you have licensed translation rights. You may not use the Material for promotional purposes. AIPP reserves all rights not specifically granted herein.
4. The foregoing license shall not take effect unless and until AIPP or its agent, Copyright Clearance Center, receives the Payment in accordance with Copyright Clearance Center Billing and Payment Terms and Conditions, which are incorporated herein by reference.
5. AIPP or the Copyright Clearance Center may, within two business days of granting this license, revoke the license for any reason whatsoever, with a full refund payable to you. Should you violate the terms of this license at any time, AIPP, AIP Publishing LLC, or Copyright Clearance Center may revoke the license with no refund to you. Notice of such revocation will be made using the contact information provided by you. Failure to receive such notice will not nullify the revocation.
6. AIPP makes no representations or warranties with respect to the Material. You agree to indemnify and hold harmless AIPP, AIP Publishing LLC, and their officers, directors, employees or agents from and against any and all claims arising out of your use of the Material other than as specifically authorized herein.
7. The permission granted herein is personal to you and is not transferable or assignable without the prior written permission of AIPP. This license may not be amended except in a writing signed by the party to be charged.
8. If purchase orders, acknowledgments or check endorsements are issued on any forms containing terms and conditions which are inconsistent with these provisions, such inconsistent terms and conditions shall be of no force and effect. This document, including the CCC Billing and Payment Terms and Conditions, shall be the entire agreement between the parties relating to the

subject matter hereof.

This Agreement shall be governed by and construed in accordance with the laws of the State of New York. Both parties hereby submit to the jurisdiction of the courts of New York County for purposes of resolving any disputes that may arise hereunder.

Questions? customercare@copyright.com or +1-855-239-3415 (toll free in the US) or +1-978-646-2777.

Figure 6 Permission:

AIP PUBLISHING LLC LICENSE
TERMS AND CONDITIONS

Jan 05, 2016

All payments must be made in full to CCC. For payment instructions, please see information listed at the bottom of this form.

License Number 3782801221873
Order Date Jan 05, 2016
Publisher AIP Publishing LLC
Publication Applied Physics Letters
Article Title Highly efficient bulk heterojunction photovoltaic cell based on tris[4-(5-phenylthiophen-2-yl)phenyl]amine and C70 combined with optimized electron transport layer
Author Yan-qiong Zheng, William J. Potscavage Jr., Takeshi Komino, et al.
Online Publication Date Apr 16, 2013
Volume number 102
Issue number 15
Type of Use Thesis/Dissertation
Requestor type Student
Format Print and electronic
Portion Figure/Table
Number of 1
figures/tables
Title of your thesis / dissertation The Influence of Morphology and Molecular Orientation on the Efficiency and Lifetime of Organic Solar Cells
Expected completion date Jan 2016
Estimated size (number of pages) 150
Total 0.00 USD

Terms and Conditions

AIP Publishing LLC -- Terms and Conditions: Permissions Uses

AIP Publishing LLC ("AIPP") hereby grants to you the non-exclusive right and license to use and/or distribute the Material according to the use specified in your order, on a one-time basis, for the specified term, with a maximum distribution equal to the number that you have ordered. Any links or other content

accompanying the Material are not the subject of this license.

1. You agree to include the following copyright and permission notice with the reproduction of the Material: "Reprinted with permission from [FULL CITATION]. Copyright [PUBLICATION YEAR], AIP Publishing LLC." For an article, the copyright and permission notice must be printed on the first page of the article or book chapter. For photographs, covers, or tables, the copyright and permission notice may appear with the Material, in a footnote, or in the reference list.
2. If you have licensed reuse of a figure, photograph, cover, or table, it is your responsibility to ensure that the material is original to AIPP and does not contain the copyright of another entity, and that the copyright notice of the figure, photograph, cover, or table does not indicate that it was reprinted by AIPP, with permission, from another source. Under no circumstances does AIPP, purport or intend to grant permission to reuse material to which it does not hold copyright.
3. You may not alter or modify the Material in any manner. You may translate the Material into another language only if you have licensed translation rights. You may not use the Material for promotional purposes. AIPP reserves all rights not specifically granted herein.
4. The foregoing license shall not take effect unless and until AIPP or its agent, Copyright Clearance Center, receives the Payment in accordance with Copyright Clearance Center Billing and Payment Terms and Conditions, which are incorporated herein by reference.
5. AIPP or the Copyright Clearance Center may, within two business days of granting this license, revoke the license for any reason whatsoever, with a full refund payable to you. Should you violate the terms of this license at any time, AIPP, AIP Publishing LLC, or Copyright Clearance Center may revoke the license with no refund to you. Notice of such revocation will be made using the contact information provided by you. Failure to receive such notice will not nullify the revocation.
6. AIPP makes no representations or warranties with respect to the Material. You agree to indemnify and hold harmless AIPP, AIP Publishing LLC, and their officers, directors, employees or agents from and against any and all claims arising out of your use of the Material other than as specifically authorized herein.
7. The permission granted herein is personal to you and is not transferable or assignable without the prior written permission of AIPP. This license may not be amended except in a writing signed by the party to be charged.
8. If purchase orders, acknowledgments or check endorsements are issued on any forms containing terms and conditions which are inconsistent with these provisions, such inconsistent terms and conditions shall be of no force and effect. This document, including the CCC Billing and Payment Terms and Conditions, shall be the entire agreement between the parties relating to the subject matter hereof.

This Agreement shall be governed by and construed in accordance with the laws of the State of New York. Both parties hereby submit to the jurisdiction of the courts of New York County for purposes of resolving any disputes that may arise hereunder.

Questions? customercare@copyright.com or +1-855-239-3415 (toll free in the US) or +1-978-646-2777.

Figure 8 Permission:

Controlling templating effects at the organic/inorganic interface using (111) oriented copper iodide

L. A. Rochford, D. S. Keeble, O. J. Holmes, G. J. Clarkson and T. S. Jones, *J. Mater. Chem. C*, 2014, **2**, 6056

DOI: 10.1039/C4TC00759J

This article is licensed under a [Creative Commons Attribution 3.0 Unported Licence](#). Material from this article can be used in other publications provided that the correct acknowledgement is given with the reproduced material.

Reproduced material should be attributed as follows:

For reproduction of material from NJC:

[Original citation] - Published by The Royal Society of Chemistry (RSC) on behalf of the Centre National de la Recherche Scientifique (CNRS) and the RSC.

For reproduction of material from PCCP:

[Original citation] - Published by the PCCP Owner Societies.

For reproduction of material from PPS:

[Original citation] - Published by The Royal Society of Chemistry (RSC) on behalf of the European Society for Photobiology, the European Photochemistry Association, and RSC.

For reproduction of material from all other RSC journals:

[Original citation] - Published by The Royal Society of Chemistry.

Information about reproducing material from RSC articles with different licences is available on our [Permission Requests page](#).

Chapter 5 Permission:

ELSEVIER

LICENSE

TERMS AND CONDITIONS

Jan 06, 2016

This is a License Agreement between Sibi Sutti ("You") and Elsevier ("Elsevier") provided by Copyright Clearance Center ("CCC"). The license consists of your order details, the terms and conditions provided by Elsevier, and the payment terms and conditions.

All payments must be made in full to CCC. For payment instructions, please see information listed at the bottom of this form.

Supplier	Elsevier The Boulevard, Langford Kidlington, Oxford, OX5 1GB, UK	Limited Lane
Registered Company Number	1982084	
Customer name	Sibi Sutti	
Customer address	200, University Avenue West	

	Waterloo, ON N2L3G1
License number	3783281481216
License date	Jan 06, 2016
Licensed content publisher	Elsevier
Licensed content publication	Organic Electronics
Licensed content title	Role of the donor material and the donor–acceptor mixing ratio in increasing the efficiency of Schottky junction organic solar cells
Licensed content author	Sibi Suttu,Graeme Williams,Hany Aziz
Licensed content date	October 2013
Licensed content volume number	14
Licensed content issue number	10
Number of pages	9
Start Page	2392
End Page	2400
Type of Use	reuse in a thesis/dissertation
Portion	full article
Format	both print and electronic
Are you the author of this Elsevier article?	Yes
Will you be translating?	No
Title of your thesis/dissertation	The Influence of Morphology and Molecular Orientation on the Efficiency and Lifetime of Organic Solar Cells
Expected completion date	Jan 2016
Estimated size (number of pages)	150
Elsevier VAT number	GB 494 6272 12
Permissions price	0.00 USD
VAT/Local Sales Tax	0.00 USD / 0.00 GBP
Total	0.00 USD
Terms and Conditions	

INTRODUCTION

1. The publisher for this copyrighted material is Elsevier. By clicking "accept" in connection with completing this licensing transaction, you agree that the following terms and conditions apply to this transaction (along with the Billing and Payment terms and conditions established by Copyright Clearance Center, Inc. ("CCC"), at the time that you opened your Rightslink account and that are available at any time at <http://myaccount.copyright.com>).

GENERAL TERMS

2. Elsevier hereby grants you permission to reproduce the aforementioned material subject to the terms and conditions indicated.

3. Acknowledgement: If any part of the material to be used (for example, figures) has appeared in our publication with credit or acknowledgement to another source, permission must also be sought from that source. If such permission is not obtained then that material may not be included in your

publication/copies. Suitable acknowledgement to the source must be made, either as a footnote or in a reference list at the end of your publication, as follows:

"Reprinted from Publication title, Vol /edition number, Author(s), Title of article / title of chapter, Pages No., Copyright (Year), with permission from Elsevier [OR APPLICABLE SOCIETY COPYRIGHT OWNER]." Also Lancet special credit - "Reprinted from The Lancet, Vol. number, Author(s), Title of article, Pages No., Copyright (Year), with permission from Elsevier."

4. Reproduction of this material is confined to the purpose and/or media for which permission is hereby given.

5. Altering/Modifying Material: Not Permitted. However figures and illustrations may be altered/adapted minimally to serve your work. Any other abbreviations, additions, deletions and/or any other alterations shall be made only with prior written authorization of Elsevier Ltd. (Please contact Elsevier at permissions@elsevier.com)

6. If the permission fee for the requested use of our material is waived in this instance, please be advised that your future requests for Elsevier materials may attract a fee.

7. Reservation of Rights: Publisher reserves all rights not specifically granted in the combination of (i) the license details provided by you and accepted in the course of this licensing transaction, (ii) these terms and conditions and (iii) CCC's Billing and Payment terms and conditions.

8. License Contingent Upon Payment: While you may exercise the rights licensed immediately upon issuance of the license at the end of the licensing process for the transaction, provided that you have disclosed complete and accurate details of your proposed use, no license is finally effective unless and until full payment is received from you (either by publisher or by CCC) as provided in CCC's Billing and Payment terms and conditions. If full payment is not received on a timely basis, then any license preliminarily granted shall be deemed automatically revoked and shall be void as if never granted. Further, in the event that you breach any of these terms and conditions or any of CCC's Billing and Payment terms and conditions, the license is automatically revoked and shall be void as if never granted. Use of materials as described in a revoked license, as well as any use of the materials beyond the scope of an unrevoked license, may constitute copyright infringement and publisher reserves the right to take any and all action to protect its copyright in the materials.

9. Warranties: Publisher makes no representations or warranties with respect to the licensed material.

10. Indemnity: You hereby indemnify and agree to hold harmless publisher and CCC, and their respective officers, directors, employees and agents, from and against any and all claims arising out of your use of the licensed material other than as specifically authorized pursuant to this license.

11. No Transfer of License: This license is personal to you and may not be sublicensed, assigned, or transferred by you to any other person without publisher's written permission.

12. No Amendment Except in Writing: This license may not be amended except in a writing signed by both parties (or, in the case of publisher, by CCC on publisher's behalf).

13. Objection to Contrary Terms: Publisher hereby objects to any terms contained in any purchase order, acknowledgment, check endorsement or other writing prepared by you, which terms are inconsistent with these terms and conditions or CCC's Billing and Payment terms and conditions. These terms and conditions, together with CCC's Billing and Payment terms and conditions (which are incorporated herein), comprise the entire agreement between you and publisher (and CCC) concerning this licensing transaction. In the event of any conflict between your obligations established by these terms and

conditions and those established by CCC's Billing and Payment terms and conditions, these terms and conditions shall control.

14. **Revocation:** Elsevier or Copyright Clearance Center may deny the permissions described in this License at their sole discretion, for any reason or no reason, with a full refund payable to you. Notice of such denial will be made using the contact information provided by you. Failure to receive such notice will not alter or invalidate the denial. In no event will Elsevier or Copyright Clearance Center be responsible or liable for any costs, expenses or damage incurred by you as a result of a denial of your permission request, other than a refund of the amount(s) paid by you to Elsevier and/or Copyright Clearance Center for denied permissions.

LIMITED LICENSE

The following terms and conditions apply only to specific license types:

15. **Translation:** This permission is granted for non-exclusive world **English** rights only unless your license was granted for translation rights. If you licensed translation rights you may only translate this content into the languages you requested. A professional translator must perform all translations and reproduce the content word for word preserving the integrity of the article.

16. **Posting licensed content on any Website:** The following terms and conditions apply as follows: Licensing material from an Elsevier journal: All content posted to the web site must maintain the copyright information line on the bottom of each image; A hyper-text must be included to the Homepage of the journal from which you are licensing at <http://www.sciencedirect.com/science/journal/xxxx> or the Elsevier homepage for books at <http://www.elsevier.com>; Central Storage: This license does not include permission for a scanned version of the material to be stored in a central repository such as that provided by Heron/XanEdu.

Licensing material from an Elsevier book: A hyper-text link must be included to the Elsevier homepage at <http://www.elsevier.com> . All content posted to the web site must maintain the copyright information line on the bottom of each image.

Posting licensed content on Electronic reserve: In addition to the above the following clauses are applicable: The web site must be password-protected and made available only to bona fide students registered on a relevant course. This permission is granted for 1 year only. You may obtain a new license for future website posting.

17. **For journal authors:** the following clauses are applicable in addition to the above:

Preprints:

A preprint is an author's own write-up of research results and analysis, it has not been peer-reviewed, nor has it had any other value added to it by a publisher (such as formatting, copyright, technical enhancement etc.).

Authors can share their preprints anywhere at any time. Preprints should not be added to or enhanced in any way in order to appear more like, or to substitute for, the final versions of articles however authors can update their preprints on arXiv or RePEc with their Accepted Author Manuscript (see below).

If accepted for publication, we encourage authors to link from the preprint to their formal publication via its DOI. Millions of researchers have access to the formal publications on ScienceDirect, and so links will help users to find, access, cite and use the best available version. Please note that Cell Press, The

Lancet and some society-owned have different preprint policies. Information on these policies is available on the journal homepage.

Accepted Author Manuscripts: An accepted author manuscript is the manuscript of an article that has been accepted for publication and which typically includes author-incorporated changes suggested during submission, peer review and editor-author communications.

Authors can share their accepted author manuscript:

- – immediately
 - via their non-commercial person homepage or blog
 - by updating a preprint in arXiv or RePEc with the accepted manuscript
 - via their research institute or institutional repository for internal institutional uses or as part of an invitation-only research collaboration work-group
 - directly by providing copies to their students or to research collaborators for their personal use
 - for private scholarly sharing as part of an invitation-only work group on commercial sites with which Elsevier has an agreement
- – after the embargo period
 - via non-commercial hosting platforms such as their institutional repository
 - via commercial sites with which Elsevier has an agreement

In all cases accepted manuscripts should:

- – link to the formal publication via its DOI
- – bear a CC-BY-NC-ND license - this is easy to do
- – if aggregated with other manuscripts, for example in a repository or other site, be shared in alignment with our hosting policy not be added to or enhanced in any way to appear more like, or to substitute for, the published journal article.

Published journal article (JPA): A published journal article (PJA) is the definitive final record of published research that appears or will appear in the journal and embodies all value-adding publishing activities including peer review co-ordination, copy-editing, formatting, (if relevant) pagination and online enrichment.

Policies for sharing publishing journal articles differ for subscription and gold open access articles:

Subscription Articles: If you are an author, please share a link to your article rather than the full-text. Millions of researchers have access to the formal publications on ScienceDirect, and so links will help your users to find, access, cite, and use the best available version.

Theses and dissertations which contain embedded PJAs as part of the formal submission can be posted publicly by the awarding institution with DOI links back to the formal publications on ScienceDirect.

If you are affiliated with a library that subscribes to ScienceDirect you have additional private sharing rights for others' research accessed under that agreement. This includes use for classroom teaching and internal training at the institution (including use in course packs and courseware programs), and inclusion of the article for grant funding purposes.

Gold Open Access Articles: May be shared according to the author-selected end-user license and should contain a [CrossMark logo](#), the end user license, and a DOI link to the formal publication on

ScienceDirect.

Please refer to Elsevier's [posting policy](#) for further information.

18. **For book authors** the following clauses are applicable in addition to the above: Authors are permitted to place a brief summary of their work online only. You are not allowed to download and post the published electronic version of your chapter, nor may you scan the printed edition to create an electronic version. **Posting to a repository:** Authors are permitted to post a summary of their chapter only in their institution's repository.

19. **Thesis/Dissertation:** If your license is for use in a thesis/dissertation your thesis may be submitted to your institution in either print or electronic form. Should your thesis be published commercially, please reapply for permission. These requirements include permission for the Library and Archives of Canada to supply single copies, on demand, of the complete thesis and include permission for Proquest/UMI to supply single copies, on demand, of the complete thesis. Should your thesis be published commercially, please reapply for permission. Theses and dissertations which contain embedded PJAs as part of the formal submission can be posted publicly by the awarding institution with DOI links back to the formal publications on ScienceDirect.

Elsevier Open Access Terms and Conditions

You can publish open access with Elsevier in hundreds of open access journals or in nearly 2000 established subscription journals that support open access publishing. Permitted third party re-use of these open access articles is defined by the author's choice of Creative Commons user license. See our [open access license policy](#) for more information.

Terms & Conditions applicable to all Open Access articles published with Elsevier:

Any reuse of the article must not represent the author as endorsing the adaptation of the article nor should the article be modified in such a way as to damage the author's honour or reputation. If any changes have been made, such changes must be clearly indicated.

The author(s) must be appropriately credited and we ask that you include the end user license and a DOI link to the formal publication on ScienceDirect.

If any part of the material to be used (for example, figures) has appeared in our publication with credit or acknowledgement to another source it is the responsibility of the user to ensure their reuse complies with the terms and conditions determined by the rights holder.

Additional Terms & Conditions applicable to each Creative Commons user license:

CC BY: The CC-BY license allows users to copy, to create extracts, abstracts and new works from the Article, to alter and revise the Article and to make commercial use of the Article (including reuse and/or resale of the Article by commercial entities), provided the user gives appropriate credit (with a link to the formal publication through the relevant DOI), provides a link to the license, indicates if changes were made and the licensor is not represented as endorsing the use made of the work. The full details of the license are available at <http://creativecommons.org/licenses/by/4.0>.

CC BY NC SA: The CC BY-NC-SA license allows users to copy, to create extracts, abstracts and new works from the Article, to alter and revise the Article, provided this is not done for commercial purposes, and that the user gives appropriate credit (with a link to the formal publication through the relevant DOI),

provides a link to the license, indicates if changes were made and the licensor is not represented as endorsing the use made of the work. Further, any new works must be made available on the same conditions. The full details of the license are available at <http://creativecommons.org/licenses/by-nc-sa/4.0>.

CC BY NC ND: The CC BY-NC-ND license allows users to copy and distribute the Article, provided this is not done for commercial purposes and further does not permit distribution of the Article if it is changed or edited in any way, and provided the user gives appropriate credit (with a link to the formal publication through the relevant DOI), provides a link to the license, and that the licensor is not represented as endorsing the use made of the work. The full details of the license are available at <http://creativecommons.org/licenses/by-nc-nd/4.0>. Any commercial reuse of Open Access articles published with a CC BY NC SA or CC BY NC ND license requires permission from Elsevier and will be subject to a fee.

Commercial reuse includes:

- – Associating advertising with the full text of the Article
- – Charging fees for document delivery or access
- – Article aggregation
- – Systematic distribution via e-mail lists or share buttons

Posting or linking by commercial companies for use by customers of those companies

20. Other Conditions:

v1.8

Questions? customercare@copyright.com or +1-855-239-3415 (toll free in the US) or +1-978-646-2777.

Chapter 6 Permission:

Interplay between efficiency and device architecture for small molecule organic solar cells

G. Williams, S. Suttty and H. Aziz, *Phys. Chem. Chem. Phys.*, 2014, **16**, 11398

DOI: 10.1039/C4CP01295J

If you are not the author of this article and you wish to reproduce material from it in a third party non-RSC publication you must [formally request permission](#) using RightsLink. Go to our [Instructions for using RightsLink page](#) for details.

Authors contributing to RSC publications (journal articles, books or book chapters) do not need to formally request permission to reproduce material contained in this article provided that the correct acknowledgement is given with the reproduced material.

Reproduced material should be attributed as follows:

- > For reproduction of material from NJC:
Reproduced from Ref. XX with permission from the Centre National de la Recherche Scientifique (CNRS) and The Royal Society of Chemistry.
- > For reproduction of material from PCCP:
Reproduced from Ref. XX with permission from the PCCP Owner Societies.
- > For reproduction of material from PPS:
Reproduced from Ref. XX with permission from the European Society for Photobiology, the European Photochemistry Association, and The Royal Society of Chemistry.

References

Chapter 1

- [1] O. Morton, "A New Day Dawning? Silicon Valley sunrise," *Nature*, vol. 443, no. September, pp. 19–22, 2006.
- [2] International Energy Agency, "WORLD ENERGY OUTLOOK 2014 FACTSHEET," 2015.
- [3] J. Hansen, M. Sato, P. Kharecha, D. Beerling, V. Masson-delmotte, M. Pagani, M. Raymo, D. L. Royer, and J. C. Zachos, "Target Atmospheric CO₂ : Where Should Humanity Aim?," 2008.
- [4] R. Koningstein and D. Fork, "What It Would Really Take to Reverse Climate Change," *IEEE Spectrum*, 2014. [Online]. Available: <http://spectrum.ieee.org/energy/renewables/what-it-would-really-take-to-reverse-climate-change>. [Accessed: 04-Dec-2014].
- [5] International Energy Agency, "Renewable Energy FAQ." [Online]. Available: <http://www.iea.org/aboutus/faqs/renewableenergy/>. [Accessed: 04-Dec-2014].
- [6] First Solar, "Topaz Solar Farm." [Online]. Available: <http://www.firstsolar.com/en/about-us/projects/topaz-solar-farm>. [Accessed: 04-Dec-2014].
- [7] Heliatek, "Heliatek consolidates its technology leadership by establishing a new world record for organic solar technology with a cell efficiency of 12%," 2013. [Online]. Available: http://www.heliatek.com/newscenter/latest_news/neuer-weltrekord-fur-organische-solarzellen-heliatek-behauptet-sich-mit-12-zelleffizienz-als-technologiefuhrer/?lang=en. [Accessed: 14-Jan-2015].
- [8] M. A. Green, K. Emery, Y. Hishikawa, W. Warta, and E. D. Dunlop, "Solar cell efficiency tables (version 42)," *Prog. Org. Coatings*, vol. 21, pp. 827–837, 2013.
- [9] T. D. Nielsen, C. Cruickshank, S. Foged, J. Thorsen, and F. C. Krebs, "Business, market and intellectual property analysis of polymer solar cells," *Sol. Energy Mater. Sol. Cells*, vol. 94, no. 10, pp. 1553–1571, Oct. 2010.
- [10] J. Kalowekamo and E. Baker, "Estimating the manufacturing cost of purely organic solar cells," *Sol. Energy*, vol. 83, no. 8, pp. 1224–1231, Aug. 2009.
- [11] J. D. Myers and J. Xue, "Organic Semiconductors and their Applications in Photovoltaic Devices," *Polym. Rev.*, vol. 52, no. 1, pp. 1–37, Jan. 2012.

- [12] V. Coropceanu, A. Demetrio, S. Filho, Y. Olivier, R. Silbey, and J. Bredas, "Charge Transport in Organic Semiconductors," *Chem. Rev.*, vol. 107, pp. 659–676, 2007.
- [13] C. Schünemann, D. Wynands, K. Eichhorn, M. Stamm, K. Leo, and M. Riede, "Evaluation and Control of the Orientation of Small Molecules for Strongly Absorbing Organic Thin Films," *J. Phys. Chem. C*, vol. 117, pp. 11600–11609, 2013.
- [14] R. R. Lunt, J. B. Benziger, and S. R. Forrest, "Relationship between crystalline order and exciton diffusion length in molecular organic semiconductors.," *Adv. Mater.*, vol. 22, no. 11, pp. 1233–6, Mar. 2010.
- [15] G. A. Chamberlain, "Organic solar cells: A review," *Sol. Cells*, vol. 8, no. 1, pp. 47–83, Feb. 1983.
- [16] C. W. Tang, "Two-layer organic photovoltaic cell," *Appl. Phys. Lett.*, vol. 48, no. 2, p. 183, 1986.
- [17] M. Riede, T. Mueller, W. Tress, R. Schueppel, and K. Leo, "Small-molecule solar cells-status and perspectives.," *Nanotechnology*, vol. 19, no. 42, p. 424001, Oct. 2008.
- [18] J. Meyer, S. Hamwi, M. Kröger, W. Kowalsky, T. Riedl, and A. Kahn, "Transition metal oxides for organic electronics: energetics, device physics and applications.," *Adv. Mater.*, vol. 24, no. 40, pp. 5408–27, Oct. 2012.
- [19] V. Shrotriya, G. Li, Y. Yao, C.-W. Chu, and Y. Yang, "Transition metal oxides as the buffer layer for polymer photovoltaic cells," *Appl. Phys. Lett.*, vol. 88, no. 7, p. 073508, 2006.
- [20] S. Yoo, W. J. Potscavage, B. Domercq, S.-H. Han, T.-D. Li, S. C. Jones, R. Szoszkiewicz, D. Levi, E. Riedo, S. R. Marder, and B. Kippelen, "Analysis of improved photovoltaic properties of pentacene/C60 organic solar cells: Effects of exciton blocking layer thickness and thermal annealing," *Solid. State. Electron.*, vol. 51, no. 10, pp. 1367–1375, Oct. 2007.
- [21] V. Tripathi, D. Datta, G. S. Samal, A. Awasthi, and S. Kumar, "Role of exciton blocking layers in improving efficiency of copper phthalocyanine based organic solar cells," *J. Non. Cryst. Solids*, vol. 354, no. 19–25, pp. 2901–2904, May 2008.
- [22] B. P. Rand, J. Genoe, P. Heremans, and J. Poortmans, "Solar Cells Utilizing Small Molecular Weight Organic Semiconductors," *Prog. Photovoltaics Res. Appl.*, vol. 15, pp. 659–676, 2007.

- [23] A. L. Ayzner, D. Nordlund, D.-H. Kim, Z. Bao, and M. F. Toney, "Ultrafast Electron Transfer at Organic Semiconductor Interfaces: Importance of Molecular Orientation," *J. Phys. Chem. Lett.*, p. 141204140234004, Dec. 2014.
- [24] R. A. J. Janssen and J. Nelson, "Factors limiting device efficiency in organic photovoltaics.," *Adv. Mater.*, vol. 25, no. 13, pp. 1847–58, Apr. 2013.
- [25] U. Hörmann, C. Lorch, A. Hinderhofer, A. Gerlach, M. Gruber, J. Kraus, B. Sykora, S. Grob, T. Linderl, A. Wilke, A. Opitz, R. Hansson, A. S. Anselmo, Y. Ozawa, Y. Nakayama, H. Ishii, N. Koch, E. Moons, F. Schreiber, and W. Brütting, "Voc from a Morphology Point of View: the Influence of Molecular Orientation on the Open Circuit Voltage of Organic Planar Heterojunction Solar Cells," *J. Phys. Chem. C*, vol. 118, no. 46, pp. 26462–26470, Nov. 2014.
- [26] Y. Lin, Y. Li, and X. Zhan, "Small molecule semiconductors for high-efficiency organic photovoltaics.," *Chem. Soc. Rev.*, vol. 41, no. 11, pp. 4245–72, Jun. 2012.
- [27] Y. Liu, J. Zhao, Z. Li, C. Mu, W. Ma, H. Hu, K. Jiang, H. Lin, H. Ade, and H. Yan, "Aggregation and morphology control enables multiple cases of high-efficiency polymer solar cells.," *Nat. Commun.*, vol. 5, no. 9, p. 5293, Jan. 2014.
- [28] Q. Zhang, B. Kan, F. Liu, G. Long, X. Wan, X. Chen, Y. Zuo, W. Ni, H. Zhang, M. Li, Z. Hu, F. Huang, Y. Cao, Z. Liang, M. Zhang, T. P. Russell, and Y. Chen, "Small-molecule solar cells with efficiency over 9%," *Nat. Photonics*, no. November, pp. 1–7, Nov. 2014.
- [29] X. Xiao, K. J. Bergemann, J. D. Zimmerman, K. Lee, and S. R. Forrest, "Small-Molecule Planar-Mixed Heterojunction Photovoltaic Cells with Fullerene-Based Electron Filtering Buffers," *Adv. Energy Mater.*, vol. 4, no. 7, May 2014.

Chapter 2

- [1] B. P. Rand, J. Genoe, P. Heremans, and J. Poortmans, "Solar Cells Utilizing Small Molecular Weight Organic Semiconductors," *Prog. Photovoltaics Res. Appl.*, vol. 15, pp. 659–676, 2007.
- [2] Y. Lin, Y. Li, and X. Zhan, "Small molecule semiconductors for high-efficiency organic photovoltaics.," *Chem. Soc. Rev.*, vol. 41, no. 11, pp. 4245–72, Jun. 2012.
- [3] S. Heutz, R. Cloots, T.S. Jones, Structural templating effects in molecular heterostructures grown by organic molecular-beam deposition, *Appl. Phys. Lett.* 77 (2000) 3938. doi:10.1063/1.1332820.
- [4] P. Sullivan, S. Heutz, S.M. Schultes, T.S. Jones, Influence of codeposition on the

performance of CuPc–C60 heterojunction photovoltaic devices, *Appl. Phys. Lett.* 84 (2004) 1210. doi:10.1063/1.1643549.

- [5] A. Opitz, M. Bronner, W. Brütting, Ambipolar charge carrier transport in mixed organic layers of phthalocyanine and fullerene, *J. Appl. Phys.* 101 (2007) 063709. doi:10.1063/1.2436836.
- [6] M. Zhang, H. Wang, H. Tian, Y. Geng, C.W. Tang, Bulk heterojunction photovoltaic cells with low donor concentration., *Adv. Mater.* 23 (2011) 4960–4. doi:10.1002/adma.201102173.
- [7] R. Pandey, A. a. Gunawan, K.A. Mkhoyan, R.J. Holmes, Efficient Organic Photovoltaic Cells Based on Nanocrystalline Mixtures of Boron Subphthalocyanine Chloride and C60, *Adv. Funct. Mater.* 22 (2012) 617–624. doi:10.1002/adfm.201101948.
- [8] Y. Zheng, W.J. Potscavage, T. Komino, C. Adachi, Highly efficient bulk heterojunction photovoltaic cell based on tris[4-(5-phenylthiophen-2-yl)phenyl]amine and C70 combined with optimized electron transport layer, *Appl. Phys. Lett.* 102 (2013) 153302. doi:10.1063/1.4801954.
- [9] Y. Zheng, W.J. Potscavage, Q. Zhang, T. Komino, M. Taneda, C. Adachi, Comparison of small amounts of polycrystalline donor materials in C70-based bulk heterojunction photovoltaics and optimization of dinaphthothienothiophene based photovoltaic, *Org. Electron.* 15 (2014) 878–885. doi:10.1016/j.orgel.2014.01.012.
- [10] S.M. Bayliss, S. Heutz, R. Cloots, R.L. Middleton, G. Rumbles, T.S. Jones, Templating Effects in the Growth of Metal-Free Phthalocyanine Polymorphic Double Layers, *Adv. Mater.* 12 (2000) 202–206. doi:10.1002/(SICI)1521-4095(200002)12:3<202::AID-ADMA202>3.0.CO;2-L.
- [11] T. Ogawa, K. Kuwamoto, S. Isoda, T. Kobayashi, N. Karl, 3,4:9,10-Perylenetetracarboxylic dianhydride (PTCDA) by electron crystallography, *Acta Crystallogr. Sect. B Struct. Sci.* 55 (1999) 123–130. doi:10.1107/S0108768198009872.
- [12] S. Heutz, T.S. Jones, Structural and morphological modifications in double layer heterostructures containing H₂Pc, perylene-3, 4, 9, 10-tetracarboxylic dianhydride and Alq₃, *J. Appl. Phys.* 92 (2002) 3039. doi:10.1063/1.1499743.

- [13] T. Sakurai, S. Kawai, R. Fukasawa, J. Shibata, K. Akimoto, Influence of 3,4,9,10-Perylene Tetracarboxylic Dianhydride Intermediate Layer on Molecular Orientation of Phthalocyanine, *Jpn. J. Appl. Phys.* 44 (2005) 1982–1986. doi:10.1143/JJAP.44.1982.
- [14] T. Sakurai, R. Fukasawa, K. Akimoto, Growth Process of Phthalocyanine Films Deposited on 3,4,9,10-Perylene Tetracarboxylic Dianhydride Template Layers, *Jpn. J. Appl. Phys.* 45 (2006) 255–259. doi:10.1143/JJAP.45.255.
- [15] T. Sakurai, R. Fukasawa, K. Saito, K. Akimoto, Control of molecular orientation of organic p–i–n structures by using molecular templating effect at heterointerfaces, *Org. Electron.* 8 (2007) 702–708. doi:10.1016/j.orgel.2007.06.004.
- [16] P. Sullivan, T.S. Jones, a. J. Ferguson, S. Heutz, Structural templating as a route to improved photovoltaic performance in copper phthalocyanine/fullerene (C₆₀) heterojunctions, *Appl. Phys. Lett.* 91 (2007) 233114. doi:10.1063/1.2821229.
- [17] B.E. Lassiter, R.R. Lunt, C.K. Renshaw, S.R. Forrest, Structural templating of multiple polycrystalline layers in organic photovoltaic cells., *Opt. Express.* 18 (2010) A444–50. <http://www.ncbi.nlm.nih.gov/pubmed/21165074>.
- [18] C.H. Cheng, J. Wang, G.T. Du, S.H. Shi, Z.J. Du, Z.Q. Fan, et al., Organic solar cells with remarkable enhanced efficiency by using a CuI buffer to control the molecular orientation and modify the anode, *Appl. Phys. Lett.* 97 (2010) 083305. doi:10.1063/1.3483159.
- [19] L. Cattin, J.C. Bernède, Y. Lare, S. Dabos-Seignon, N. Stephant, M. Morsli, et al., Improved performance of organic solar cells by growth optimization of MoO₃/CuI double-anode buffer, *Phys. Status Solidi.* 210 (2013) 802–808. doi:10.1002/pssa.201228665.
- [20] J.C. Bernède, L. Cattin, M. Morsli, S.R.B. Kanth, S. Patil, N. Stephant, Improvement of the Efficiency of Organic Solar Cells Using the Terthiophene-Pyran-Malononitrile (T3PM) as Electron Donor, through the use of a MoO₃/CuI Anode Buffer Layer, *Energy Procedia.* 31 (2012) 81–88. doi:10.1016/j.egypro.2012.11.168.
- [21] B.P. Rand, D. Cheyns, K. Vasseur, N.C. Giebink, S. Mothy, Y. Yi, et al., The Impact of Molecular Orientation on the Photovoltaic Properties of a Phthalocyanine / Fullerene Heterojunction, *Adv. Funct. Mater.* 22 (2012) 2987–2995. doi:10.1002/adfm.201200512.

- [22] J. Lee, D. Park, I. Heo, S. Yim, Effect of cuprous halide interlayers on the device performance of ZnPc/C60 organic solar cells, *Mater. Res. Bull.* 58 (2014) 132–135. doi:10.1016/j.materresbull.2014.03.030.
- [23] H. Jung Kim, H. Shim, J. Whan Kim, H. Hwi Lee, J. Kim, CuI interlayers in lead phthalocyanine thin films enhance near-infrared light absorption, *Appl. Phys. Lett.* 100 (2012) 263303. doi:10.1063/1.4730604.
- [24] J.W. Kim, H.J. Kim, T.-M. Kim, T.G. Kim, J.-H. Lee, J.W. Kim, et al., High performance organic planar heterojunction solar cells by controlling the molecular orientation, *Curr. Appl. Phys.* 13 (2013) 7–11. doi:10.1016/j.cap.2012.06.003.
- [25] T. Kim, H. Shim, M. Choi, H.J. Kim, J. Kim, Multilayer Epitaxial Growth of Lead Phthalocyanine and C 70 Using CuBr as a Templating Layer for Enhancing the Efficiency of Organic Photovoltaic Cells, (2014).
- [26] T.-M. Kim, H.J. Kim, H.-S. Shim, M.-S. Choi, J.W. Kim, J.-J. Kim, The epitaxial growth of lead phthalocyanine on copper halogen compounds as the origin of templating effects, *J. Mater. Chem. A* 2 (2014) 8730. doi:10.1039/c4ta00332b.
- [27] K. Vasseur, K. Broch, A.L. Ayzner, B.P. Rand, D. Cheyns, C. Frank, et al., Controlling the texture and crystallinity of evaporated lead phthalocyanine thin films for near-infrared sensitive solar cells., *ACS Appl. Mater. Interfaces* 5 (2013) 8505–15. doi:10.1021/am401933d.
- [28] L. A. Rochford, D.S. Keeble, O.J. Holmes, G.J. Clarkson, T.S. Jones, Controlling templating effects at the organic/inorganic interface using (111) oriented copper iodide, *J. Mater. Chem. C* 2 (2014) 6056. doi:10.1039/C4TC00759J.
- [29] L. A Rochford, A.J. Ramadan, S. Heutz, T.S. Jones, Selective nucleation of iron phthalocyanine crystals on micro-structured copper iodide., *Phys. Chem. Chem. Phys.* 16 (2014) 25404–8. doi:10.1039/c4cp04217d.

Chapter 4

- [1] J. D. Myers and J. Xue, “Organic Semiconductors and their Applications in Photovoltaic Devices,” *Polym. Rev.*, vol. 52, no. 1, pp. 1–37, Jan. 2012.

Chapter 5

- [1] M. Riede, T. Mueller, W. Tress, R. Schueppel, K. Leo, Small-molecule solar cells-status and perspectives., *Nanotechnology*. 19 (2008) 424001.
- [2] J. Xue, B.P. Rand, S. Uchida, S.R. Forrest, Mixed donor-acceptor molecular heterojunctions for photovoltaic applications. II. Device performance, *J. Appl. Phys.* 98 (2005) 124903.
- [3] J. Xue, Carrier transport in multilayer organic photodetectors: II. Effects of anode preparation, *J. Appl. Phys.* 95 (2004) 1869.
- [4] D. Gebeyehu, B. Maennig, J. Drechsel, K. Leo, M. Pfeiffer, Bulk-heterojunction photovoltaic devices based on donor-acceptor organic small molecule blends, *Sol. Energy Mater. and Sol. Cells*. 79 (2003) 81–92.
- [5] M. Zhang, H. Ding, Y. Gao, C.W. Tang, Organic Schottky barrier photovoltaic cells based on MoOx/C60, *Appl. Phys. Lett.* 96 (2010) 183301.
- [6] B. Yang, F. Guo, Y. Yuan, Z. Xiao, Y. Lu, Q. Dong, et al., Solution-Processed Fullerene-Based Organic Schottky Junction Devices for Large-Open-Circuit-Voltage Organic Solar Cells, *Adv. Mater.* 25 (2012) 572–577.
- [7] M. Zhang, H. Wang, H. Tian, Y. Geng, C.W. Tang, Bulk heterojunction photovoltaic cells with low donor concentration., *Adv. Mater.* 23 (2011) 4960–4.
- [8] M.C. Scharber, D. Mühlbacher, M. Koppe, P. Denk, C. Waldauf, A. J. Heeger, et al., Design Rules for Donors in Bulk-Heterojunction Solar Cells—Towards 10% Energy-Conversion Efficiency, *Adv. Mater.* 18 (2006) 789–794.
- [9] M. Zhang, H. Ding, C.W. Tang, Y. Gao, Strong interface p-doping and band bending in C60 on MoOx, *Org. Electron.* 12 (2011) 1588–1593.
- [10] X. Xiao, J.D. Zimmerman, B.E. Lassiter, K.J. Bergemann, S.R. Forrest, A hybrid planar-mixed tetraphenyldibenzoperiflanthene/C70 photovoltaic cell, *Appl. Phys. Lett.* 102 (2013) 073302.
- [11] R. Pandey, A. A. Gunawan, K.A. Mkhoyan, R.J. Holmes, Efficient Organic Photovoltaic Cells Based on Nanocrystalline Mixtures of Boron Subphthalocyanine Chloride and C60, *Adv. Funct. Mater.* 22 (2012) 617–624.
- [12] H.X. Wei, J. Li, Y. Cai, Z.Q. Xu, S.T. Lee, Y.Q. Li, et al., Electronic structures of planar and mixed C70/CuPc heterojunctions in organic photovoltaic devices, *Org. Electron.* 12 (2011) 1422–1428.

- [13] C. Schünemann, D. Wynands, L. Wilde, M.P. Hein, S. Pfützner, C. Elschner, et al., Phase separation analysis of bulk heterojunctions in small-molecule organic solar cells using zinc-phthalocyanine and C60, *Phys. Rev. B.* 85 (2012) 245314.
- [14] S.-W. Liu, W.-C. Su, C.-C. Lee, C.-W. Cheng, C.-C. Chou, C.-F. Lin, Absorbing Visible Light Materials of Subphthalocyanine and C70 for Efficient Planar-Mixed Organic Photovoltaic Devices, *J. Electrochem. Soc.* 160 (2012) G14–G18.
- [15] W. Tress, K. Leo, M. Riede, Effect of concentration gradients in ZnPc:C60 bulk heterojunction organic solar cells, *Sol. Energy Mater. and Sol. Cells.* 95 (2011) 2981–2986.
- [16] R. Pandey, R.J. Holmes, Graded donor-acceptor heterojunctions for efficient organic photovoltaic cells., *Adv. Mater.* 22 (2010) 5301–5.
- [17] C. Kim, B. Lee, H.J. Yang, H.M. Lee, J.G. Lee, H. Shin, Effects of Surface Treatment on Work Function of ITO (Indium Tin Oxide) Films, *J. Korean Phys. Soc.* 47 (2005) 417–421.
- [18] Q. Wang, G. Williams, H. Aziz, Photo-degradation of the indium tin oxide (ITO)/organic interface in organic optoelectronic devices and a new outlook on the role of ITO surface treatments and interfacial layers in improving device stability, *Org. Electron.* 13 (2012) 2075–2082.
- [19] S. Jang, H. Chae, D. Jung, H. Kim, C.-K. Kim, Simultaneous Oxygen Plasma and Thermal Treatments of an ITO Surface to Improve the Electrical Characteristics of Organic Light-Emitting Diodes, *J. Korean Phys. Soc.* 51 (2007) 956.
- [20] A.P. Yuen, A.-M. Hor, J.S. Preston, R. Klenkler, N.M. Bamsey, R.O. Loutfy, A simple parallel tandem organic solar cell based on metallophthalocyanines, *Appl. Phys. Lett.* 98 (2011) 173301.
- [21] N.M. Bamsey, A.P. Yuen, A.-M. Hor, R. Klenkler, J.S. Preston, R.O. Loutfy, Heteromorphic chloroindium phthalocyanine films for improved photovoltaic performance, *Sol. Energy Mater. and Sol. Cells.* 95 (2011) 2937–2940.
- [22] A.P. Yuen, S.M. Jovanovic, A.-M. Hor, R. A. Klenkler, G. A. Devenyi, R.O. Loutfy, et al., Photovoltaic properties of M-phthalocyanine/fullerene organic solar cells, *Sol. Energy.* 86 (2012) 1683–1688.
- [23] S. Kazaoui, R. Ross, N. Minami, Intermolecular charge-transfer excitation in C60 films: Evidence from luminescence and photoconductivity, *Phys. Rev. B.* 52 (1995) 4–7.

- [24] C.-S. Ho, C.-S. Lee, W.-C. Hsu, C.-Y. Lin, Y.-N. Lai, C.-W. Wang, Efficiency improvements in single-heterojunction organic photovoltaic cells by insertion of wide-bandgap electron-blocking layers, *Solid-State Electron.* 76 (2012) 101–103.
- [25] A.J. Makinen, I.G. Hill, Z.H. Kafafi, Vacuum level alignment in organic guest-host systems, *J. Appl. Phys.* 92 (2002) 1–6.
- [26] D.-W. Chou, C.-J. Huang, T.-C. Wang, W.-R. Chen, T.-H. Meen, Effect of electron transport layer materials on the performance of copper phthalocyanine/fullerene heterojunction with function of organic solar cells, *J. Non-Cryst. Solids.* 356 (2010) 2156–2161.
- [27] R. Schlaf, B. A. Parkinson, P. A. Lee, K.W. Nebesny, N.R. Armstrong, HOMO/LUMO Alignment at PTCDA/ZnPc and PTCDA/ClInPc Heterointerfaces Determined by Combined UPS and XPS Measurements, *J. Phys. Chem. B.* 103 (1999) 2984–2992.
- [28] Z. Wu, H. Yang, Y. Duan, W. Xie, Improved efficiency of organic light-emitting devices employing bathocuproine doped in the electron-transporting layer, *Semicond. Sci. Technol.* 49 (2003).
- [29] K.H. Lee, S.M. Kim, J.Y. Kim, Y.K. Kim, S.S. Yoon, Red Fluorescent Organic Light-Emitting Diodes Using Modified Pyran-containing DCJT B Derivatives, *Bull. Korean Chem. Soc.* 31 (2010) 2884–2888.
- [30] W. Tress, S. Pfuetzner, K. Leo, M. Riede, Open circuit voltage and IV curve shape of ZnPc:C60 solar cells with varied mixing ratio and hole transport layer, *J. Photon. Energy.* 1 (2011) 011114.

Chapter 6

- [1] M. Zhang, H. Ding, Y. Gao, C. Tang, *Appl. Phys. Lett.*, **2010**, 96, 183301.
- [2] M. Zhang, H. Wang, H. Tian, Y. Geng, C. Tang, *Adv. Mater.*, **2011**, 23, 4960.
- [3] S. Suttty, G. Williams, H. Aziz, *Org. Electron.*, **2013**, 14, 2392.
- [4] G. Williams, H. Aziz, *Org. Electron.*, **2013**, 15, 47.
- [5] B. J. Tremolet de Villers, R. C. MacKenzie, J. J. Jasieniak, N. D. Treat, M. L. Chabiny, *Adv. Energy Mater.*, **2013**, 1.
- [6] W. Tress, S. Corvers, K. Leo, M. Riede, *Adv. Energy Mater.*, **2013**, 3, 873.

- [7] Z. Li, F. Gao, N. C. Greenham, C. R. McNeill, *Adv. Funct. Mater.*, **2011**, *21*, 1419.
- [8] P. Chen, J. Huang, Z. Xiong, F. Li, *Org. Electron.*, **2012**, *14*, 621.
- [9] M. Riede, T. Mueller, W. Tress, R. Schueppel, K. Leo, *Nanotechnology*, **2008**, *19*, 424001.
- [10] N. M. Bamsey, A. P. Yuen, A. M. Hor, R. Klenkler, J. S. Preston, R. O. Loutfy, *Sol. Energy Mater. Sol. Cells*, **2011**, *95*, 1970.
- [11] A. P. Yuen, S. M. Jovanovic, A. M. Hor, R. A. Klenkler, G. A. Devenyi, R. O. Loutfy, J. S. Preston, *Solar Energy*, **2012**, *86*, 1683.
- [12] N. M. Bamsey, A. P. Yuen, A. M. Hor, R. Klenkler, J. S. Preston, R. O. Loutfy, *Sol. Energy Mater. Sol. Cells*, **2011**, *95*, 2937.
- [13] C. Tang, *Appl. Phys. Lett.*, **1986**, *48*, 183.
- [14] J. Halls, C. Walsh, N. Greenham, E. Marseglia, R. Friend, S. Moratti, A. Holmes, *Nature*, **1995**, *376*, 498.
- [15] G. Yu, J. Gao, J. Hummelen, F. Wudl, A. Heeger, *Science-AAAS-Weekly Paper Edition*, **1995**, *270*, 1789.
- [16] G. Yu, A. J. Heeger, *J. Appl. Phys.*, **1995**, *78*, 4510.
- [17] R. M. Pinto, *The Journal of Physical Chemistry C*, **2014**.
- [18] R. Lessmann, Z. Hong, S. Scholz, B. Maennig, M. Riede, K. Leo, *Org. Electron.*, **2010**, *11*, 539.
- [19] W. Wang, D. Placencia, N. R. Armstrong, *Org. Electron.*, **2011**, *12*, 383.
- [20] Y. Zang, J. Yu, J. Huang, R. Jiang, G. Huang, *Journal of Physics D: Applied Physics*, **2012**, *45*, 175101.
- [21] B. P. Rand, J. Xue, S. Uchida, S. R. Forrest, *J. Appl. Phys.*, **2005**, *98*, 124902.
- [22] S. Kazaoui, R. Ross, N. Minami, *Physical Review B*, **1995**, *52*, R11665.
- [23] B. Yang, F. Guo, Y. Yuan, Z. Xiao, Y. Lu, Q. Dong, J. Huang, *Adv. Mater.*, **2012**, *25*, 572.

- [24] X. Xiao, K. J. Bergemann, J. D. Zimmerman, K. Lee, S. R. Forrest, *Adv. Energy Mater.*, **2013**.
- [25] Y. Lin, L. Ma, Y. Li, Y. Liu, D. Zhu, X. Zhan, *Adv. Energy Mater.*, **2013**, 4, 1
- [26] I. Hwang, C. R. McNeill, N. C. Greenham, *J. Appl. Phys.*, **2009**, 106, 094506.

Chapter 7

- [1] X. Xiao, K.J. Bergemann, J.D. Zimmerman, K. Lee, S.R. Forrest, Small-Molecule Planar-Mixed Heterojunction Photovoltaic Cells with Fullerene-Based Electron Filtering Buffers, *Adv. Energy Mater.* 4 (2014). doi:10.1002/aenm.201301557.
- [2] S. Suttty, G. Williams, H. Aziz, Understanding charge transport in vacuum deposited Schottky organic solar cells with microsecond transient photocurrent measurements, (2014). doi:10.1117/12.2061067.
- [3] A. Mishra, P. Bäuerle, Small molecule organic semiconductors on the move: promises for future solar energy technology., *Angew. Chem. Int. Ed. Engl.* 51 (2012) 2020–67. doi:10.1002/anie.201102326.
- [4] J. You, L. Dou, Z. Hong, G. Li, Y. Yang, Recent trends in polymer tandem solar cell research, *Prog. Polym. Sci.* (2013). doi:10.1016/j.progpolymsci.2013.04.005.
- [5] M. Riede, C. Uhrich, J. Widmer, R. Timmreck, D. Wynands, G. Schwartz, et al., Efficient Organic Tandem Solar Cells based on Small Molecules, *Adv. Funct. Mater.* 21 (2011) 3019–3028. doi:10.1002/adfm.201002760.
- [6] Y. Sun, G.C. Welch, W.L. Leong, C.J. Takacs, G.C. Bazan, A.J. Heeger, Solution-processed small-molecule solar cells with 6.7% efficiency., *Nat. Mater.* 11 (2012) 44–8. doi:10.1038/nmat3160.
- [7] S. Suttty, G. Williams, H. Aziz, Fullerene-based Schottky-junction organic solar cells: a brief review, *J. Photonics Energy.* 4 (2014) 040999. doi:10.1117/1.JPE.4.040999.
- [8] P. Heremans, D. Cheyns, B.P. Rand, Strategies for increasing the efficiency of heterojunction organic solar cells: material selection and device architecture., *Acc. Chem. Res.* 42 (2009) 1740–7. doi:10.1021/ar9000923.

- [9] T. Sakurai, R. Fukasawa, K. Saito, K. Akimoto, Control of molecular orientation of organic p-i-n structures by using molecular templating effect at heterointerfaces, *Org. Electron.* 8 (2007) 702–708. doi:10.1016/j.orgel.2007.06.004.
- [10] P. Sullivan, T.S. Jones, a. J. Ferguson, S. Heutz, Structural templating as a route to improved photovoltaic performance in copper phthalocyanine / fullerene (C60) heterojunctions, *Appl. Phys. Lett.* 91 (2007) 233114. doi:10.1063/1.2821229.
- [11] B. Verreet, R. Müller, B.P. Rand, K. Vasseur, P. Heremans, Structural templating of chloro-aluminum phthalocyanine layers for planar and bulk heterojunction organic solar cells, *Org. Electron.* 12 (2011) 2131–2139. doi:10.1016/j.orgel.2011.08.031.
- [12] J.C. Bernède, L. Cattin, M. Makha, V. Jeux, P. Leriche, J. Roncali, et al., MoO₃/CuI hybrid buffer layer for the optimization of organic solar cells based on a donor-acceptor triphenylamine, *Sol. Energy Mater. Sol. Cells.* 110 (2013) 107–114. doi:10.1016/j.solmat.2012.12.003.
- [13] W. Zhao, J.P. Mudrick, Y. Zheng, W.T. Hammond, Y. Yang, J. Xue, Enhancing photovoltaic response of organic solar cells using a crystalline molecular template, *Org. Electron.* 13 (2012) 129–135. doi:10.1016/j.orgel.2011.10.016.
- [14] C. Schünemann, D. Wynands, K. Eichhorn, M. Stamm, K. Leo, M. Riede, Evaluation and Control of the Orientation of Small Molecules for Strongly Absorbing Organic Thin Films, *J. Phys. Chem. C.* 117 (2013) 11600–11609.
- [15] B.P. Rand, D. Cheyns, K. Vasseur, N.C. Giebink, S. Mothy, Y. Yi, et al., The Impact of Molecular Orientation on the Photovoltaic Properties of a Phthalocyanine / Fullerene Heterojunction, *Adv. Funct. Mater.* 22 (2012) 2987–2995. doi:10.1002/adfm.201200512.
- [16] J. Lee, D. Park, I. Heo, S. Yim, Effect of cuprous halide interlayers on the device performance of ZnPc/C60 organic solar cells, *Mater. Res. Bull.* 58 (2014) 132–135. doi:10.1016/j.materresbull.2014.03.030.
- [17] T.-M. Kim, H.-S. Shim, M.-S. Choi, H.J. Kim, J.-J. Kim, Multi-layer epitaxial growth of lead-phthalocyanine and C70 using CuBr as a templating layer for the efficiency enhancement of organic photovoltaic cells., *ACS Appl. Mater. Interfaces.* (2014). doi:10.1021/am405946m.
- [18] Y. Yi, V. Coropceanu, J.-L. Brédas, Exciton-dissociation and charge-

recombination processes in pentacene/C60 solar cells: theoretical insight into the impact of interface geometry., *J. Am. Chem. Soc.* 131 (2009) 15777–83. doi:10.1021/ja905975w.

- [19] A. Poschlad, V. Meded, R. Maul, W. Wenzel, Different interface orientations of pentacene and PTCDA induce different degrees of disorder., *Nanoscale Res. Lett.* 7 (2012) 248. doi:10.1186/1556-276X-7-248.
- [20] T. Matsushima, H. Matsuo, T. Yamamoto, A. Nakao, H. Murata, Horizontally oriented molecular thin films for application in organic solar cells, *Sol. Energy Mater. Sol. Cells.* 123 (2014) 81–91. doi:10.1016/j.solmat.2014.01.004.
- [21] U. Hörmann, C. Lorch, A. Hinderhofer, A. Gerlach, M. Gruber, J. Kraus, et al., Voc from a Morphology Point of View: the Influence of Molecular Orientation on the Open Circuit Voltage of Organic Planar Heterojunction Solar Cells, *J. Phys. Chem. C.* 118 (2014) 26462–26470. doi:10.1021/jp506180k.
- [22] G.O. Ngongang Ndjawa, K.R. Graham, R. Li, S.M. Conron, P. Erwin, K.W. Chou, et al., Impact of Molecular Orientation and Spontaneous Interfacial Mixing on the Performance of Organic Solar Cells, *Chem. Mater.* (2015) 150810070747006. doi:10.1021/acs.chemmater.5b01845.
- [23] B.E. Lassiter, R.R. Lunt, C.K. Renshaw, S.R. Forrest, Structural templating of multiple polycrystalline layers in organic photovoltaic cells., *Opt. Express.* 18 (2010) A444–50. <http://www.ncbi.nlm.nih.gov/pubmed/21165074>.
- [24] T. Sakurai, S. Kawai, R. Fukasawa, J. Shibata, K. Akimoto, Influence of 3,4,9,10-Perylene Tetracarboxylic Dianhydride Intermediate Layer on Molecular Orientation of Phthalocyanine, *Jpn. J. Appl. Phys.* 44 (2005) 1982–1986. doi:10.1143/JJAP.44.1982.
- [25] K. V Chauhan, P.J. Sullivan, J.L. Yang, T.S. Jones, Efficient organic photovoltaic cells through structural modification of chloroaluminum phthalocyanine/fullerene heterojunctions, *J. Phys. Chem. C.* 114 (2010) 3304–3308. doi:10.1021/jp910601k.
- [26] H. Jung Kim, H. Shim, J. Whan Kim, H. Hwi Lee, J. Kim, CuI interlayers in lead phthalocyanine thin films enhance near-infrared light absorption, *Appl. Phys. Lett.* 100 (2012) 263303. doi:10.1063/1.4730604.
- [27] C.H. Cheng, J. Wang, G.T. Du, S.H. Shi, Z.J. Du, Z.Q. Fan, et al., Organic solar cells with remarkable enhanced efficiency by using a CuI buffer to control the

molecular orientation and modify the anode, *Appl. Phys. Lett.* 97 (2010) 083305. doi:10.1063/1.3483159.

- [28] K. Vasseur, K. Broch, A.L. Ayzner, B.P. Rand, D. Cheyns, C. Frank, et al., Controlling the texture and crystallinity of evaporated lead phthalocyanine thin films for near-infrared sensitive solar cells., *ACS Appl. Mater. Interfaces.* 5 (2013) 8505–15. doi:10.1021/am401933d.
- [29] T. Kim, H. Shim, M. Choi, H.J. Kim, J. Kim, Multilayer Epitaxial Growth of Lead Phthalocyanine and C 70 Using CuBr as a Templating Layer for Enhancing the Efficiency of Organic Photovoltaic Cells, (2014).
- [30] P. Sullivan, T.S. Jones, a. J. Ferguson, S. Heutz, Structural templating as a route to improved photovoltaic performance in copper phthalocyanine/fullerene (C₆₀) heterojunctions, *Appl. Phys. Lett.* 91 (2007) 233114. doi:10.1063/1.2821229.
- [31] B.P. Rand, J. Xue, S. Uchida, S.R. Forrest, Mixed donor-acceptor molecular heterojunctions for photovoltaic applications. I. Material properties, *J. Appl. Phys.* 98 (2005) 124902. doi:10.1063/1.2142072.

Chapter 8

- [1] M. Jørgensen, K. Norrman, F.C. Krebs, M. Jorgensen, K. Norrman, F.C. Krebs, Stability/degradation of polymer solar cells, *Sol. Energy Mater. Sol. Cells.* 92 (2008) 686–714. doi:10.1016/j.solmat.2008.01.005.
- [2] H. Cao, W. He, Y. Mao, X. Lin, K. Ishikawa, J.H. Dickerson, et al., Recent progress in degradation and stabilization of organic solar cells, *J. Power Sources.* 264 (2014) 168–183. doi:10.1016/j.jpowsour.2014.04.080.
- [3] Q.L. Song, M.L. Wang, E.G. Obbard, X.Y. Sun, X.M. Ding, X.Y. Hou, et al., Degradation of small-molecule organic solar cells, *Appl. Phys. Lett.* 89 (2006) 10–13. doi:10.1063/1.2422911.
- [4] N. Grossiord, J.M. Kroon, R. Andriessen, P.W.M. Blom, Degradation mechanisms in organic photovoltaic devices, *Org. Electron.* 13 (2012) 432–456. doi:10.1016/j.orgel.2011.11.027.
- [5] F.C. Krebs, Degradation and stability of polymer and organic solar cells, *Sol. Energy Mater. Sol. Cells.* 92 (2008) 685. doi:10.1016/j.solmat.2008.01.016.

- [6] F. Jin, B. Chu, W. Li, Z. Su, B. Zhao, X. Yan, et al., Improvement in power conversion efficiency and long-term lifetime of organic photovoltaic cells by using bathophenanthroline/molybdenum oxide as compound cathode buffer layer, *Sol. Energy Mater. Sol. Cells*. 117 (2013) 189–193. doi:10.1016/j.solmat.2013.05.007.
- [7] V. Shrotriya, G. Li, Y. Yao, C.-W. Chu, Y. Yang, Transition metal oxides as the buffer layer for polymer photovoltaic cells, *Appl. Phys. Lett.* 88 (2006) 073508. doi:10.1063/1.2174093.
- [8] D.Y. Kim, J. Subbiah, G. Sarasqueta, F. So, H. Ding, Y. Gao, The effect of molybdenum oxide interlayer on organic photovoltaic cells, *Appl. Phys. Lett.* 95 (2009) 093304. doi:10.1063/1.3220064.
- [9] Q.L. Song, F.Y. Li, H. Yang, H.R. Wu, X.Z. Wang, W. Zhou, et al., Small-molecule organic solar cells with improved stability, *Chem. Phys. Lett.* 416 (2005) 42–46. doi:10.1016/j.cplett.2005.09.052.
- [10] X. Xiao, J.D. Zimmerman, B.E. Lassiter, K.J. Bergemann, S.R. Forrest, A hybrid planar-mixed tetraphenyldibenzoperiflanthene/C70 photovoltaic cell, *Appl. Phys. Lett.* 102 (2013) 073302. doi:10.1063/1.4793195.
- [11] M. Tavakkoli, R. Ajeian, M. Nakhaee Badrabadi, S. Saleh Ardestani, S.M.H. Feiz, K. Elahi Nasab, Progress in stability of organic solar cells exposed to air, *Sol. Energy Mater. Sol. Cells*. 95 (2011) 1964–1969. doi:10.1016/j.solmat.2011.01.029.
- [12] M. Hermenau, M. Riede, K. Leo, S.A. Gevorgyan, F.C. Krebs, K. Norrman, Water and oxygen induced degradation of small molecule organic solar cells, *Sol. Energy Mater. Sol. Cells*. 95 (2011) 1268–1277. doi:10.1016/j.solmat.2011.01.001.
- [13] H.R. Wu, Q.L. Song, M.L. Wang, F.Y. Li, H. Yang, Y. Wu, et al., Stable small-molecule organic solar cells with 1,3,5-tris(2-N-phenylbenzimidazolyl) benzene as an organic buffer, *Thin Solid Films*. 515 (2007) 8050–8053. doi:10.1016/j.tsf.2007.03.187.
- [14] G. Williams, H. Aziz, The effect of charge extraction layers on the photo-stability of vacuum-deposited versus solution-coated organic solar cells, *Org. Electron. Physics, Mater. Appl.* 15 (2014) 47–56. doi:10.1016/j.orgel.2013.10.017.
- [15] Q. Wang, G. Williams, H. Aziz, Photo-degradation of the indium tin oxide

(ITO)/organic interface in organic optoelectronic devices and a new outlook on the role of ITO surface treatments and interfacial layers in improving device stability, *Org. Electron.* 13 (2012) 2075–2082. doi:10.1016/j.orgel.2012.06.017.

- [16] R. Könenkamp, G. Priebe, B. Pietzak, Carrier mobilities and influence of oxygen in C60 films, *Phys. Rev. B.* 60 (1999) 11804–11808. doi:10.1103/PhysRevB.60.11804.
- [17] H. Werner, T. Schedel-Niedrig, M. Wohlers, D. Herein, B. Herzog, R. Schlogl, et al., Reaction of molecular oxygen with C60: spectroscopic studies, *J. Chem. Soc. Faraday Trans.* 90 (1994) 403–409. doi:10.1039/ft9949000403.
- [18] R. Lessmann, Z. Hong, S. Scholz, B. Maennig, M.K. Riede, K. Leo, Aging of flat heterojunction zinc phthalocyanine/fullerene C60 organic solar cells, *Org. Electron. Physics, Mater. Appl.* 11 (2010) 539–543. doi:10.1016/j.orgel.2009.12.010.
- [19] M. Hermenau, S. Scholz, K. Leo, M. Riede, Total charge amount as indicator for the degradation of small molecule organic solar cells, *Sol. Energy Mater. Sol. Cells.* 95 (2011) 1278–1283. doi:10.1016/j.solmat.2010.09.031.
- [20] M. Zhang, H. Wang, H. Tian, Y. Geng, C.W. Tang, Bulk heterojunction photovoltaic cells with low donor concentration., *Adv. Mater.* 23 (2011) 4960–4. doi:10.1002/adma.201102173.
- [21] M. Zhang, H. Ding, Y. Gao, C.W. Tang, Organic Schottky barrier photovoltaic cells based on MoO_x/C₆₀, *Appl. Phys. Lett.* 96 (2010) 183301. doi:10.1063/1.3415497.
- [22] T.-M. Kim, H.-S. Shim, M.-S. Choi, H.J. Kim, J.-J. Kim, Multi-layer epitaxial growth of lead-phthalocyanine and C70 using CuBr as a templating layer for the efficiency enhancement of organic photovoltaic cells., *ACS Appl. Mater. Interfaces.* (2014). doi:10.1021/am405946m.
- [23] H. Jung Kim, H. Shim, J. Whan Kim, H. Hwi Lee, J. Kim, CuI interlayers in lead phthalocyanine thin films enhance near-infrared light absorption, *Appl. Phys. Lett.* 100 (2012) 263303. doi:10.1063/1.4730604.
- [24] B.E. Lassiter, R.R. Lunt, C.K. Renshaw, S.R. Forrest, Structural templating of multiple polycrystalline layers in organic photovoltaic cells., *Opt. Express.* 18 (2010) A444–50. <http://www.ncbi.nlm.nih.gov/pubmed/21165074>.

- [25] B.P. Rand, D. Cheyng, K. Vasseur, N.C. Giebink, S. Mothy, Y. Yi, et al., The Impact of Molecular Orientation on the Photovoltaic Properties of a Phthalocyanine / Fullerene Heterojunction, *Adv. Funct. Mater.* 22 (2012) 2987–2995. doi:10.1002/adfm.201200512.
- [26] T. V. Basova, V.G. Kiselev, V. a. Plyashkevich, P.B. Cheblakov, F. Latteyer, H. Peisert, et al., Orientation and morphology of chloroaluminum phthalocyanine films grown by vapor deposition: Electrical field-induced molecular alignment, *Chem. Phys.* 380 (2011) 40–47. doi:10.1016/j.chemphys.2010.12.004.
- [27] C. Schünemann, D. Wynands, K. Eichhorn, M. Stamm, K. Leo, M. Riede, Evaluation and Control of the Orientation of Small Molecules for Strongly Absorbing Organic Thin Films, *J. Phys. Chem. C* 117 (2013) 11600–11609.
- [28] S. Suttu, G. Williams, H. Aziz, Role of the donor material and the donor–acceptor mixing ratio in increasing the efficiency of Schottky junction organic solar cells, *Org. Electron.* 14 (2013) 2392–2400. doi:10.1016/j.orgel.2013.06.001.
- [29] S. Kazaoui, R. Ross, N. Minami, Intermolecular charge-transfer excitation in C60 films: Evidence from luminescence and photoconductivity, *Phys. Rev. B* 52 (1995) 4–7.
- [30] J.W. Arbogast, A.P. Darmanyan, C.S. Foote, Y. Rubin, F.N. Diederich, M.M. Alvarez, et al., Photophysical Properties of C60, *J. Phys. Chem.* (1991) 11–12. doi:10.1021/j100154a006.
- [31] N. Bajales, S. Schmaus, T. Miyamashi, W. Wulfhekel, J. Wilhelm, M. Walz, et al., C58 on Au(111): a scanning tunneling microscopy study., *J. Chem. Phys.* 138 (2013) 104703. doi:10.1063/1.4793761.
- [32] M. Zhang, H. Ding, C.W. Tang, Y. Gao, Strong interface p-doping and band bending in C60 on MoOx, *Org. Electron.* 12 (2011) 1588–1593. doi:10.1016/j.orgel.2011.06.007.
- [33] L. Ciammaruchi, C. Wang, Y. Gao, C.W. Tang, Delineation of degradation patterns of C60-based organic solar cells under different environments, *J. Appl. Phys.* 117 (2015) 245504. doi:10.1063/1.4923091.
- [34] S.W. Cho, L.F.J. Piper, A. Demasi, A.R.H. Preston, K.E. Smith, K. V Chauhan, et al., Electronic Structure of C 60 / Phthalocyanine / ITO Interfaces Studied using Soft X-ray Spectroscopies, (2010) 1928–1933.

Appendix

Time-zero PV performance of the OSCs shown in Figure 32.

Table A8: Time-zero PV Performance of ZnPc, SubPc and ClInPc PHJ OSCs used in Chapter 8

Device	Jsc	Voc	FF	Efficiency
	[mA/cm ²]	[mV]	[%]	[%]
ZnPc	3.19	438.44	47.64	0.67
SubPc	4.80	1117.80	52.49	2.82
ClInPc	4.14	783.68	55.84	1.81

Time-zero PV performance of OSCs shown in Figure 36

Table A9: Time-zero PV Performance of Control, PTCDA-templated and CuI-templated ZnPc PHJ OSCs shown in Chapter 8

Device	Jsc	Voc	FF	Efficiency
	[mA/cm ²]	[mV]	[%]	[%]
ZnPc Control	3.19	438.44	47.64	0.67
PTCDA/ZnPc	4.10	512.76	52.77	1.11
CuI/ZnPc	3.87	491.46	50.41	0.96

Time-zero PV performance of OSCs shown in Figure 37

Table A10: Time-zero PV Performance of Control, PTCDA-templated and CuI-templated ClInPc PHJ OSCs shown in Chapter 8

Device	Jsc	Voc	FF
	[mA/cm ²]	[mV]	[%]
ClInPc Control	4.14	783.68	55.84
PTCDA/ClInPc	4.72	796.74	54.26
CuI/PTCDA	4.46	599.22	49.25